

**Dispersion-Free DWDM Channel Interleaver with  
Silicon Waveguides**

*A THESIS*

*submitted by*

**GAURANG R. BHATT**

*for the award of the degree*

*of*

**MASTER OF SCIENCE**

(by Research)



**DEPARTMENT OF ELECTRICAL ENGINEERING  
INDIAN INSTITUTE OF TECHNOLOGY MADRAS**

**May 2012**

## **THESIS CERTIFICATE**

This is to certify that the thesis titled “**Dispersion-Free DWDM Channel Interleaver with Silicon Waveguides**”, submitted by **Gaurang R. Bhatt**, to the Indian Institute of Technology, Madras, for the award of the degree of **Master of Science**, is a bonafide record of the research work done by him under my supervision. The contents of this thesis, in full or in parts, have not been submitted to any other Institute or University for the award of any degree or diploma.

**Dr. Bijoy K. Das**  
Research Guide  
Associate Professor  
Dept. of Electrical Engineering  
IIT-Madras, India, 600 036

Place: Chennai, India  
Date: Sun 20<sup>th</sup> May, 2012

Dedicated to my Parents.

## **ACKNOWLEDGEMENTS**

This thesis acknowledgment gives me an opportunity to thank all those who supported me at various stages of my research work providing motivation, knowledge, help and suggestions whenever I was in need. First and foremost, I would like to thank my mentor Dr. Bijoy K. Das, for providing me with the opportunity to work under his guidance. The personal interaction sessions and group meetings that happened over the period of my project work were truly enlightening and encouraging. I would also like to thank my General Test Committee (GTC) members Prof. E. Bhattacharya, Prof. N. Dasgupta and Prof. N. Vasa, for their valuable suggestions that helped me fine tune my research work. I am thankful to Electrical Engineering Department, IIT Madras and all the faculty of Microelectronics & MEMS labs as well as FILL & EXPO Labs for providing me with the required facilities to carry out my experimental work. I am grateful to Dr. Anuj Bhatnagar and Arun Malik at SAMEER, Mumbai for their valuable suggestions and efforts during device fiber pigtailling and packaging.

My special thanks to Mr. Harikrishna, Mr. Jayvel, Mr. Prakash, Mr. Rajendran and Mr. Sreedhar for their timely help on various technicalities pertaining to the fabrication and characterization equipments and setup. I am grateful to all my seniors for teaching me various aspects of fabrication and characterization of integrated optical devices. My special thanks to all the members of Integrated Optoelectronics, EXPO & FILL and, Microelectronics & MEMS Laboratories for their help and valuable suggestions during different stages of my research work. I thank my co-authors of various publications/proceedings, U. Karthik, Rajat and Vivek for some of the simulation results and subsequent discussions that made the submissions possible.

I am indebted to my amiable UG friends and, friends at IIT-Madras, for their love and support, which has constantly inspired and encouraged me at various stages of my life. Last but not the least, I am grateful to my parents and family for their continuing support that helped me to accomplish this piece of work.

## ABSTRACT

**KEYWORDS:** SOI, Waveguides, Integrated Optics, Silicon Photonics, Interleaver, Metal Clad Waveguides, Polarizer, Wavelength Division Multiplexing, Dispersion-free.

The growing need of higher data rates over fiber-optic communication link has attracted much interest towards the dense wavelength division multiplex (DWDM) systems. To meet these requirements, the ITU channel spacing has been reduced repeatedly and defined in the orders of 200-, 100-, 50-, 25- GHz and so on. As the channel spacing reduces, there is intense requirement for channel interleaver devices to improve the performances at transmitter / receiver ends. Recent evolution in silicon photonics research has also been directed towards the realization of large bandwidth and high speed optical interconnects as well as other functional optoelectronic devices including laser sources, modulators and detectors in Silicon-On-Insulator (SOI) platform. Therefore, demonstration of an integrated optical interleaver device in SOI platform was proposed for the current thesis work. The devices were fabricated with optimized design parameters, and characterized in terms of insertion loss, wavelength / polarization dependencies and inter-channel extinction over  $\lambda = 1520$  to 1600 nm. Some of the  $2 \times 2$  prototype devices are fiber pigtailed and packaged successfully at SAMEER, Mumbai. Our packaged devices have shown overall promising characteristics: a typical inter-channel extinction of  $> 15$  dB and 3-dB channel pass band of  $\sim 40$  GHz have been recorded. The packaged integrated optical DWDM channel interleaver fabricated with silicon waveguides in SOI platform is being reported for the first time to our knowledge.

# TABLE OF CONTENTS

<b>ACKNOWLEDGEMENTS</b>	<b>ii</b>
<b>ABSTRACT</b>	<b>iii</b>
<b>LIST OF TABLES</b>	<b>vi</b>
<b>LIST OF FIGURES</b>	<b>ix</b>
<b>ABBREVIATIONS</b>	<b>x</b>
<b>NOTATION</b>	<b>xii</b>
<b>1 Introduction</b>	<b>1</b>
1.1 Motivation . . . . .	1
1.2 Research Objective . . . . .	9
1.3 Thesis Organization . . . . .	9
<b>2 Design and Simulations</b>	<b>10</b>
2.1 Background Theory . . . . .	10
2.2 Single-mode Waveguides . . . . .	12
2.3 Directional Coupler . . . . .	20
2.4 Interleaver Design . . . . .	25
2.5 Conclusions . . . . .	28
<b>3 Fabrication and Characterization</b>	<b>29</b>
3.1 Mask Design and Fabrication . . . . .	29
3.2 Device Fabrication . . . . .	31
3.3 Device Characterizations . . . . .	40
3.4 Conclusions . . . . .	52
<b>4 Device Packaging and Testing</b>	<b>53</b>
4.1 Fiber Pigtailling . . . . .	53

4.2	Test Results and Discussions . . . . .	55
4.3	Conclusions . . . . .	59
<b>5</b>	<b>Conclusions</b>	<b>60</b>
5.1	Summary . . . . .	60
5.2	Outlook . . . . .	61
<b>A</b>	<b>Appendix</b>	<b>65</b>
A.1	Asymmetric MZI Based Interleaver . . . . .	65
A.2	Recipes for etching . . . . .	68

## LIST OF TABLES

2.1	Various waveguide geometries in SOI . . . . .	13
2.2	Calculated waveguide birefringence, mode-size and dispersion slopes for various waveguide structures . . . . .	14
2.3	Fiber-Waveguide mode overlap ( $\Gamma$ ) and affordable waveguide bending radius ( $R$ ) calculated from Fig. 2.5 for TE polarization . . . . .	16
2.4	Final design parameters of DWDM channel interleaver . . . . .	25
3.1	List of fabricated metal-clad waveguide samples . . . . .	37
3.2	List of fabricated interleaver samples . . . . .	39
3.3	Degradation of polarization extinction in LCRW based meander-bend, directional coupler and interleaver (Input: TE polarization) . . . . .	49
3.4	Degradation of polarization extinction in LCRW based meander-bend, directional coupler and interleaver (Input: TM polarization) . . . . .	50
4.1	Characteristics of prototype DWDM channel interleaver . . . . .	58



## LIST OF FIGURES

1.1 Schematic of a typical fiber optic link . . . . .	2
1.2 Schematic of a typical optical transmitter . . . . .	3
1.3 Schematic of a typical AWG . . . . .	4
1.4 Various waveguide devices in SOI . . . . .	5
2.1 Asymmetric MZI based channel interleaver . . . . .	11
2.2 Typical SOI rib waveguide structure . . . . .	13
2.3 Group index dispersion in SOI waveguides . . . . .	14
2.4 Mode-field distribution and bend-induced losses in S-bend waveguide structure . . . . .	15
2.5 Horizontal mode-spread as a function of rib waveguide (LCRW) width	16
2.6 Guided fundamental mode of a SOI based large cross-section rib waveguide and a single-mode fiber . . . . .	17
2.7 Scheme showing polarization cross-talk in bend waveguides . . . . .	18
2.8 Schematic of a metal-clad SOI rib waveguide structure. . . . .	18
2.9 Attenuation of TE and TM polarized light in metal coated SOI rib waveguide . . . . .	19
2.10 Scheme of coupled waveguides and their simulated mode-field distributions at input and output . . . . .	20
2.11 Power splitting ratio of directional coupler as a function of wavelength for various waveguide structures . . . . .	21
2.12 3-dB coupling length of directional coupler as a function of waveguide spacing and etch depth . . . . .	22
2.13 Polarization dependent power splitting ratio across optical C and L band for LCRW based directional coupler . . . . .	22
2.14 Schematic of an practical directional coupler . . . . .	23
2.15 Calculated coupling coefficient ( $\kappa$ ) as a function of spacing in bend waveguide . . . . .	24
2.16 Wavelength dependent transmission characteristics of interleaver based on various waveguide structures . . . . .	26
2.17 Wavelength dependent transmission characteristics of interleaver for TE and TM polarization . . . . .	27

2.18	Temperature effects on interleaver response . . . . .	28
3.1	Schematic top view layout used for fabricaton of interleaver mask .	30
3.2	Scheme of interleaver with integrated metal-clad waveguide polarizer	30
3.3	Fabrication process steps . . . . .	31
3.4	Comparison of waveguides fabricated with PPR and metal mask . .	35
3.5	Typical SEM images of different sections of a fabricated interleaver	36
3.6	Typical microscope image of metal coated SOI rib waveguides . . .	36
3.7	SEM images of Au and Al coated SOI rib waveguides . . . . .	38
3.8	Polished end-facet of fabricated interleaver . . . . .	40
3.9	Schematic of an end-fire coupling setup . . . . .	41
3.10	Transmitted TE and TM mode profiles for single-mode large cross-section rib waveguides . . . . .	42
3.11	Screen-shot of virtual interface developed on LABVIEW for waveguide loss measurement . . . . .	43
3.12	Measured fabry-perot resonance for large corss-section SOI rib waveguides . . . . .	44
3.13	Transmitted intensity profiles for LCRW based directional coupler .	45
3.14	Wavelength dependent power splitting ratio for LCRW based directional coupler . . . . .	45
3.15	Transmitted intensity profiles for interleaver at two successive ITU channel wavelengths . . . . .	46
3.16	Measured wavelength dependent transmission characteristics (C band) at output ports of LCRW based channel interleaver . . . . .	47
3.17	Measured wavelength dependent transmission characteristics for TE and TM polarization, at output ports of interleaver . . . . .	48
3.18	Measured wavelength dependent transmission characteristics for TE and TM polarization, at output ports of interleaver. . . . .	48
3.19	Transmitted TE and TM mode profiles for metal-clad waveguides .	50
3.20	Measured polarization extinction as a function of metal-clad waveguide length . . . . .	51
4.1	Schematic cross-section view of fiber v-grove assembly and device end-facet . . . . .	54
4.2	Photograph of a fiber pigtailed SOI interleaver chip . . . . .	54
4.3	Photograph of a packaged prototype DWDM channel interleaver . .	55

4.4	Experimental setup for characterization of packaged DWDM channel interleaver . . . . .	56
4.5	Wavelength dependent transmission characteristics ( $\lambda \sim 1550$ nm) of interleaver before and after pigtailling with SMF fibers . . . . .	56
4.6	Wavelength dependent transmission characteristics ( $\lambda \sim 1550$ nm) of interleaver before and after pigtailling with PM fibers . . . . .	57
4.7	Wavelength dependent transmission characteristics ( $\lambda = 1520$ nm to 1600 nm) at Port 3 of interleaver pigtailed with PM fibers . . . . .	58
5.1	Channel interleaver with integrated ring resonator for achieving flat-band response . . . . .	61
5.2	Proposed twin ITU channel source in SOI . . . . .	62
5.3	Interleaving of broad-band input source and proposed design modifications for reduced inter-channel cross-talk . . . . .	63
5.4	Proposed TM-pass waveguide polarizer . . . . .	64

# ABBREVIATIONS

## Acronyms

<b>AWG</b>	Arrayed Waveguide Grating
<b>Band C</b>	Conventional wavelength band ( $\lambda \sim 1527$ to $1567$ nm)
<b>Band L</b>	Long wavelength band ( $\lambda \sim 1567$ to $1607$ nm)
<b>BOX</b>	Buried Oxide
<b>BPM</b>	Beam Propagation Method
<b>CMOS</b>	Complementary Metal Oxide Semiconductor
<b>DFB</b>	Distributed Feedback
<b>DI</b>	De-ionized (water)
<b>DWDM</b>	Dense Wavelength Division Multiplexing
<b>FEM</b>	Finite Element Method
<b>FSR</b>	Free Spectral Range
<b>ICP</b>	Inductively Coupled Plasma
<b>ITU</b>	International Telecommunication Union
<b>LCRW</b>	Large Cross-section Rib Waveguide
<b>MZI</b>	Mach Zehnder Interferometer
<b>PhWW</b>	Photonic Wire Waveguide
<b>PhWRW</b>	Photonic Wire Rib Waveguide
<b>PM</b>	Polarization Maintaining
<b>PPR</b>	Positive Photo Resist
<b>RCRW</b>	Reduced Cross-section Rib Waveguide
<b>RIE</b>	Reactive Ion Etching
<b>SEM</b>	Scanning Electron Microscope
<b>SMF</b>	Single Mode Fiber
<b>SOI</b>	Silicon-On-Insulator
<b>TE</b>	Transverse Electric (polarization)
<b>TM</b>	Transverse Magnetic (polarization)
<b>UV</b>	Ultra-Violet

### Chemical Names

<b>Al</b>	Aluminum
<b>Ar</b>	Argon
<b>Au</b>	Aurum (Gold)
<b>CHF<sub>3</sub></b>	Tri-fluoro Methane
<b>Cr</b>	Chromium
<b>HF</b>	Hydro Fluoric Acid
<b>HNO<sub>3</sub></b>	Nitric Acid
<b>H<sub>2</sub>O</b>	Water
<b>H<sub>2</sub>O<sub>2</sub></b>	Hydrogen Peroxide
<b>KOH</b>	Potassium Hydroxide
<b>NaOH</b>	Sodium Hydroxide
<b>SF<sub>6</sub></b>	Sulfur Hexafluoride
<b>Si</b>	Silicon
<b>SiO<sub>2</sub></b>	Silicon dioxide
<b>TCE</b>	Tri-chloro Ethylene

### Units

<b>dB</b>	Decibel
<b>dBm</b>	Decibel milli-Watts
<b>mW</b>	milli Watts
<b>Gbps</b>	Giga-bits per second
<b>μm</b>	Micrometer
<b>ps</b>	Pico Second
<b>sccm</b>	standard cubic centimeter per minute
<b>mTorr</b>	milli-Torr (of pressure)
<b>mbar</b>	milli-Bar (of pressure)
<b>ml</b>	milli-liter (of fluid)

## NOTATION

$\mathbf{n}$	Refractive index
$\mathbf{n}_{eff}$	Effective refractive index
$\mathbf{n}_g$	Group refractive index
$\epsilon$	Permittivity
$\lambda$	Wavelength
$\beta$	Propagation constant
$\phi$	Phase of the EM wave
$\mathbf{R}$	Waveguide bending radius
$\mathbf{L}$	Length (refers to device length, component length)
$\mathbf{L}_c$	Coupling length in directional coupler
$\kappa$	Coupling coefficient or strength of coupling
$\Gamma$	Overlap integral coefficient
$\alpha$	Loss per unit length
$\delta_{dB}$	Polarization extinction
$\delta_{ch-ex}$	Channel extinction
$\Delta\lambda$	Channel spacing
$\omega_x$	Electric field distribution in horizontal direction (along x-axis)
$\omega_y$	Electric field distribution in vertical direction (along y-axis)

# CHAPTER 1

## Introduction

In this introductory chapter, we first present the basic components of a typical fiber-optic link and discuss about the necessity of photonic integrated circuits (PICs) at the transmitter and receiver ends. This is then followed by a brief review of recent advancements in silicon photonics research and SOI based PICs. Afterwards, original objective of this research work and thesis organization as per accomplishments are presented.

### 1.1 Motivation

Over the past decade, there have been tremendous advances in information and telecommunication industry. The conventional copper wires/interconnects used for transferring data over long-haul/on-chip links are incapable of meeting the growing need for higher transmission capacity. In case of long-haul communication, glass fiber links were laid across the globe in order to carry modulated light signals with low loss and higher bandwidth. In course of time, these links have become essential backbone of global data communication networks. Block diagram of a typical fiber optic communication network is shown in Fig. 1.1. It consists of various subsystems like sources / detectors, modulators / demodulators, multiplexers / de-multiplexer, de-interleaver / interleaver and fiber optic cable / link operating at wavelengths  $\lambda \sim 1.3 - 1.6 \mu\text{m}$ . For any given fiber optic link, higher data transmission capacity can be achieved by: either having higher-modulation rate of a single carrier or by increasing the number of modulated carriers (frequencies), each modulated at relatively lower rate [1]. The former involves designing of high speed electronics and complex synchronization circuitry. Whereas, the other technique, often called the Wavelength Division Multiplexing (WDM), has attracted much interest as an efficient means to increase the bandwidth of an optical network [2]. This has been made possible by the revolutionary discovery of arrayed

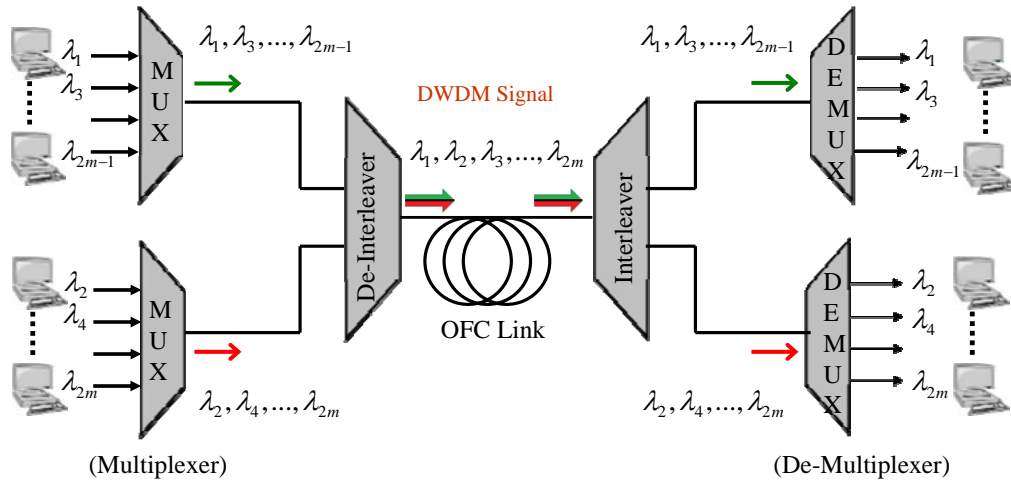


Figure 1.1: Schematic representation of a typical fiber optic link.

waveguide gratings (AWGs) [3]. The idea here is to multiplex several modulated narrow line-width optical carriers, closely spaced in frequency/wavelength domain, before sending them over a single optical fiber link.

Efforts are being made to develop cost-effective, high-speed transmitter/receiver chips, by integrating narrow line-width laser sources, modulators, wavelength multiplexers / de-multiplexers, detectors, etc. Wide variety of materials are utilized for realizing these components operating in optical communication bands (S, C, & L). Compound semiconductor based laser- and photo-diodes are often used for realising WDM sources [4, 5] and detectors [6], respectively. Narrow linewidth ITU specified DWDM channel wavelengths are defined by inscribing grating structure in gain medium (DFB laser) or replacing one of the endfacet mirrors by distributed Bragg reflector (DBR laser) [7, 8]. The quantum efficiency of laser diodes is enhanced by epitaxially grown single/double heterostructure or quantum well configurations [9]. Photo-detectors have various structural configurations like p-n, p-i-n and, metal-semiconductor-metal diodes [10]. The required higher sensitivity, faster response time and lower noise figure are obtained by suitable bandgap engineering, tactful design and associated superior circuit configurations.

A typical single channel transmitter unit is shown schematically in Fig. 1.2. In order to modulate the optical carriers, external high-speed modulators based on electro-optic lithium niobate [11] and various III-V compound semiconductors [12] have been



demonstrated and widely implemented. An electro-optic intensity modulator consists of a Mach-Zehnder Interferometer (MZI) structure formed by using single-mode waveguides and Y-junctions. Here, the incoming optical carrier is equally split in power at the input Y-branch and in absence of external field, they interfere constructively at the output Y-junction. Application of bias voltage across one arm of MZI causes localized change in refractive index of the material. If the application of applied bias voltage ( $V_\pi$ ) is enough to introduce an excess phase of  $\pi$ , then the signals will interfere destructively, resulting in absence of light at the output waveguide. Thus, application of data-bit stream in the form of voltage change can result in intensity modulated optical output. The electro-optic modulators based on lithium niobate are popular over semiconductor modulators due to their faster electro-optic response, low  $V_\pi$  and, stable temperature performances [11].

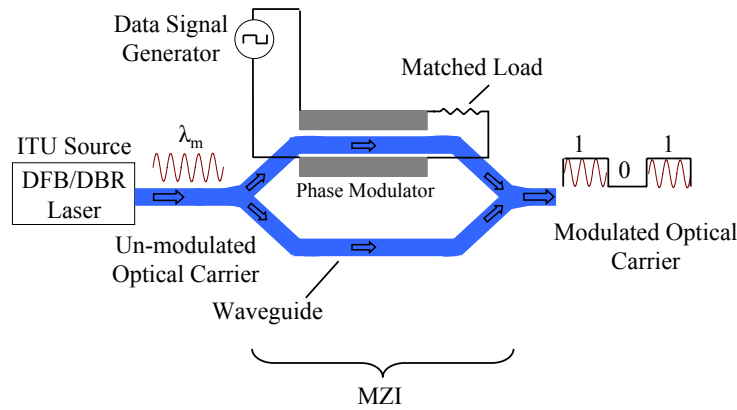


Figure 1.2: Schematic representation of a typical optical transmitter using travelling wave phase modulator.  $\lambda_m$  is any ITU channel wavelength.

The modulated optical carriers (ITU specified wavelengths) from several transmitter units are multiplexed using AWG, similar to the one shown in Fig. 1.3. The same AWG can be used at the receiver-end to de-multiplex the optical carriers. Here, the number of arrayed waveguides ( $N$ ) decides the channel packing density ( $m = \frac{FSR}{\Delta\lambda}$ ): FSR - free spectral range of AWG,  $\Delta\lambda$  - wavelength spacing between any two adjacent channels. The design of AWGs become more critical as the channel spacing ( $\Delta\lambda$ ) reduces [13]. In addition to this, DWDM channel receivers with better wavelength selectivity and low cross talk are costly. Therefore, channel interleaving devices with relatively simpler design can help to realize DWDM systems with channel spacings as low as 12.5 GHz

( $\Delta\lambda = 0.1$  nm). Interleavers can be broadly classified into three categories - AWG router, Michelson interferometer based interleavers and lattice filter [14]-[17]. The most widely used and simplest of all interleavers is based on asymmetric MZI which belongs to the lattice filter category. Such interleavers have been implemented over wide range of material platform. Asymmetric MZI based fiber interleavers [18, 19] were replaced by integrated optical DWDM channel interleavers developed over silica-on-silicon platform which became commercially popular due to their ease of fabrication, low insertion losses, low fiber-waveguide coupling loss and commercial feasibility [17]. Apart from

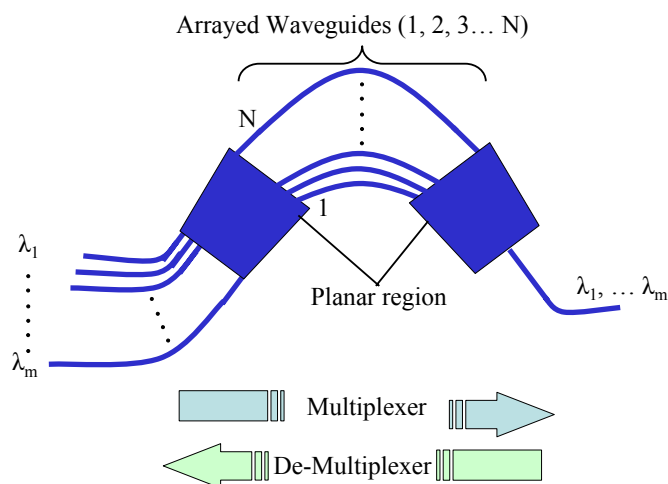


Figure 1.3: Schematic representation of a typical  $1 \times m$  Arrayed Waveguide Gratings.

AWGs [20] and interleavers [21, 22], other passive optical-networking components like power splitters [23] were also successfully demonstrated in silica-on-silicon platform. However, inspite of many advantages, silica based devices had a significantly larger device footprint and were mainly passive in operation. This is a severe limitation while designing reconfigurable optical networks.

There has been a continuing demand for finding a suitable material platform that can provide monolithic/hybrid integration of aforementioned functional photonic devices with commercial viability. Recently, silicon-on-insulator (SOI) has attracted much interest for realizing integrated optical and opto-electronic circuits [24]. In the next section we will look into the advantages that SOI platform provides and recent advances in silicon photonics research.

## Silicon Photonics

Conventional copper interconnects used for on-chip communications pose a major bottleneck for high bandwidth applications. As the electronic device dimensions are shrinking, it has been predicted that the interconnect delays will dominate the overall system delays [25]. In order to overcome these challenges, optical interconnects with a typical cross-section dimension of  $\sim 250 \text{ nm} \times 250 \text{ nm}$  (single-mode waveguide @  $\lambda \sim 1550 \text{ nm}$ ) had been proposed and successfully demonstrated along with various other integrated photonic components like sources / detectors, modulators, multiplexers / de-multiplexers, de-interleavers / interleavers, etc., in SOI platform [26].

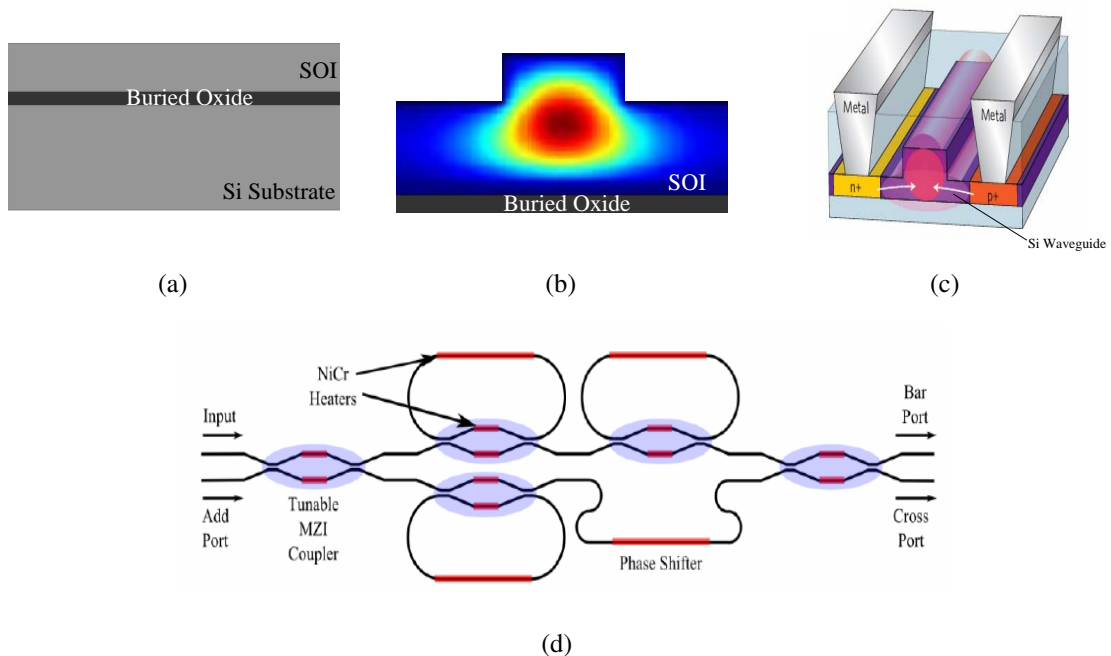


Figure 1.4: (a) Schematic cross section of a SOI wafer. (b) Typical cross-section view of a single-mode silicon rib waveguide with its simulated fundamental guided mode. (c) An integrated waveguide phase shifter with simple p-i-n configuration [27]. (d) Fully reconfigurable SOI based integrated optical add-drop multiplexer. [28].

Primarily, SOI based waveguide structures are preferred as the device layer (Si) is transparent over the optical communication band ( $1.3 \mu\text{m} - 1.6 \mu\text{m}$ ). The Si waveguides fabricated in SOI platform have a bottom cladding of  $\text{SiO}_2$  and top cladding of air/ $\text{SiO}_2$ , resulting into single-mode tighter light confinement (due to high core-cladding refractive index contrast). Typical cross-section view of a SOI wafer and a single-mode silicon rib waveguide is shown in Fig. 1.4. The refractive index of silicon waveguide

structure can be modulated by suitable thermo-/electro-optic tuning. Fig. 1.4(c) shows a cross-section of electro-optically tunable silicon waveguide structure with p-i-n configuration. Reconfigurable photonic circuits based on SOI can be realized using this refractive index modulation achieved as a result of thermo-optic/free carrier plasma dispersion (see Fig. 1.4(d)) [28]. Thus, SOI offers bright prospects for integrated optoelectronic devices [29]. The CMOS technology widely used for fabricating functional electronic devices can also be used for making commercially viable silicon based photonic devices. Recent advances in SOI based photonic/opto-electronic devices will be briefly reviewed in the following paragraphs.

**Sources/Detectors:** Conventionally, direct bandgap compound III-V semiconductors are used for realizing laser sources due to their higher quantum efficiency and flexibility in bandgap engineering. Silicon is an indirect band-gap semiconductor and hence not suitable for realizing conventional diode based laser sources. However, it has been found that the Raman scattering coefficient in case of silicon is much higher than that of silica or other widely used photonic material. All silicon Raman lasers with reduced cross section rib waveguide structures have been successfully demonstrated by *Boyras et al. and Rong et al.* [30, 31]. Recently, hybrid DFB silicon lasers (with III-V semiconductor lasing medium) have also been reported [32]-[34]. In this case, grating inscribed silicon waveguide is bonded with an AlGaInAs active layer, resulting into laser emission at  $\lambda = 1600$  nm [32]. Laser sources with desired emission wavelength in optical C and L band can be achieved by suitable design of Bragg grating and optimum material composition of active layer [33]. Evanescently coupled hybrid mode-locked lasers (repetition rate  $\sim 40$  GHz) with silicon waveguides have also been reported in SOI platform [34].

Besides various laser sources, silicon based optical amplifiers with hybrid configurations have shown a 13 dB gain at bit-rates upto 40 GHz [35]. Very recently, Al<sub>2</sub>O<sub>3</sub>:Er<sup>3+</sup> (Erbium doped Alumina) active waveguide amplifiers monolithically integrated with passive SOI waveguides have been demonstrated with a signal amplification of upto 7 dB at  $\lambda = 1533$  nm by *Agazzi et al.* [36]. Here, an adiabatically tapered SOI waveguide is used to efficiently couple light to the fundamental mode of monolithically integrated laser-active Al<sub>2</sub>O<sub>3</sub> waveguide and vice-versa [36]. It is claimed that the entire

processing is compatible with CMOS technology.

Silicon based detectors have also been demonstrated and widely used in visible wavelength range as well as  $\sim 800$  nm communication band. The conventional silicon photo-detectors are not suitable for other communication bands ( $\lambda \sim 1310$  nm, 1550 nm) as the bandgap of silicon  $E_g = 1.1$  eV ( $\lambda_g = 1127.13$  nm). However, various Si-Ge alloys are found to be suitable candidate for detecting longer wavelengths (S, C & L bands) [37]. Moreover, Si/Ge hetero-junction photo-detectors operating at longer wavelength bands have also been reported in SOI platform. Here, a heterojunction is created by deposition of Ge over double-SOI (DSOI) [38, 39]. Such structures have shown a quantum efficiency of  $> 60$  %. Hybrid photodetectors (III-V photodetectors coupled with silicon waveguides) have been reported by *Park et al.* at intel research labs [40]. Very recently, integrated AlGaInAs-silicon evanescent race track photodetector have also been demonstrated by the same group [41].

**Modulators:** Integrated optical high speed silicon phase-modulators have been demonstrated by exploiting plasma dispersion of injected free carriers into the guiding medium [42]. Typically, two types of waveguide phase shifters have been reported - MOS-capacitor type and p-i-n type (see Fig. 1.4(c) and 1.4(d)) [43]. Using MOS-capacitor type phase-shifter in MZI configuration, modulation speeds of  $> 1$  Gbps have been reported by *Liu et al.* [44]. Later, MZI modulators with p-i-n type phase shifters have been reported with a higher modulation rates of  $> 40$  Gbps [27, 45]. Modulators with micro-ring configuration have also been demonstrated with a modulation speeds of  $\sim 12$  Gbps [46]. Such modulators are limited by the resonant wavelengths of the cavity. There are also efforts to demonstrate modulators with low  $V_\pi$  ( $\sim 1$  V) by integrating photonic crystal waveguide phase-shifters in MZI configuration [47].

**Multiplexers/De-multiplexers/Filters:** As mentioned earlier, the transmission capacity of the optical communication link can be significantly increased through wavelength division multiplexing. Multiplexing of several wavelength channels can be simultaneously done using AWGs as explained earlier (see Fig. 1.3). The AWGs in SOI platform have shown impressive response for dense channel multiplexing and demultiplexing with reasonably high inter-channel extinction  $> 20$  dB in optical communication bands (C, L) [48, 49]. These structures were fabricated using sub-micron

photonic wire waveguides (PhWW).

The WDM channels packed over a single fiber optic link can be selectively dropped using wavelength selective filters. Such wavelength filters using Bragg grating structures incorporated with silicon waveguide have been demonstrated in SOI platform. These filters can be used for channel adding and dropping. Here, the Bragg gratings are suitably designed to have high reflectivity at a particular channel wavelength while rest of the wavelengths are transmitted. The reflected channel can then be dropped out using a circulator at the input side [50]. Multilayer thin film stacking can also help to realize add-drop filters [51]. Recently, wavelength add/drop multiplexers/de-multiplexers with micro-ring configuration in SOI substrate have also been reported [52].

**Interleavers:** Reconfigurable interleavers using silicon waveguides integrated with thermo-/electro-optic phase-shifters have shown an inter-channel extinction  $>15$  dB for 100 GHz DWDM grid at  $\lambda \sim 1550$  [53]-[28]. The interleaver switch fabricated using large-cross section rib waveguide structures with thermo-optic tuning offers a 4 nm band selection around  $\lambda \sim 1550 \text{ nm} \pm 8.5 \text{ nm}$  [53]. A similar approach for active tuning (thermo-/electro-optic) of interleavers has been reported by *Luo et al.* [28]. These interleavers have shown an interchannel extinction of  $\sim 20$  dB in optical C band. However, these devices are fabricated with sub-wavelength grating and/or photonic wire waveguide (PhW) structures - requiring sophisticated nano-fabrication techniques. The PhW based devices offer smaller footprints but performances are limited by some practical issues like higher fiber-device-fiber insertion loss, waveguide birefringence, dispersion etc. Insertion losses can be improved by tactful designs of tapered waveguide couplers at the input/output ends [55, 56]. Recently, waveguides with relatively low structural birefringence have also been successfully demonstrated using reduced cross section rib waveguide structures [57]. However, dispersion still remains a challenging issue for realising DWDM components (AWGs, interleavers, etc.) with a uniform response across the optical communication bands (C, L). Hence, there is an utmost need for a thorough investigation to resolve this issue and, the present work was directed for the same with a proposal to demonstrate a dispersion-free channel interleaver in SOI platform.

## 1.2 Research Objective

The progress in silicon photonics and preliminary research success at Integrated Optoelectronics / Microelectronics & MEMS Labs, IIT Madras, served as one of the primary motivation to study SOI based interleaver device. Single-mode straight and bend waveguides on SOI had been successfully demonstrated in our lab at IIT Madras [58, 59]. Later,  $2 \times 2$  directional couplers with uniform power splitting were also designed and fabricated [60, 61]. Utilizing these basic building blocks and present lab facilities, demonstration of integrated optical dispersion-free DWDM channel interleaver with silicon waveguides in SOI platform was proposed as a part of this thesis work. The key points of the final research module can be listed as below.

- Optimizing various design parameters for realizing dispersion-free DWDM channel interleaver.
- Fabrication and characterization of SOI interleaver chip.
- Fiber pigtailling, packaging and testing of SOI interleaver chip (prototype device) for DWDM applications

## 1.3 Thesis Organization

The thesis work has been split into five chapters. At first, the working principle of interleaver, its theoretical analysis, various design parameters and related simulation results are discussed in Chapter 2. This is followed by device fabrication and characterizations in Chapter 3. Later, device pigtailling, packaing and final testing results are discussed in Chapter 4. Finally, the whole thesis work is summarized in Chapter 5 and future scope of this work is discussed.

# CHAPTER 2

## Design and Simulations

In this chapter we will discuss about the design of an integrated optical interleaver to be fabricated in SOI platform. Background theory has been discussed in Section 2.1. Design of fundamental building blocks like single-mode waveguides and directional couplers have been discussed in Sections 2.2 and 2.3, respectively. Finally, overall design of a DWDM channel interleaver has been presented in Section 2.4.

### 2.1 Background Theory

As discussed in the previous chapter, asymmetric Mach-Zehnder Interferometer (MZI) is the simplest form of interleaver structure. A schematic view of such an interleaver has been shown in Fig. 2.1. The asymmetric MZI is formed by cascading two identical directional couplers. It has two input ports as well as two output ports and can be operated as a bidirectional device. Each of the incoming DWDM channel launched at one of the two input ports is equally split in power and independently guided into two arms of the MZI. Depending on the phase relationship, they interfere at the second directional coupler and accordingly the signal powers are distributed between Port 3 and Port 4, respectively.

The working principle of aforementioned device can be understood using transfer matrix method [62]. As shown in Fig. 2.1, we have annotated the electric field amplitudes associated with the guided modes at different points in the device:  $E_{1i}$  ( $E_{2j}$ ) are the electric fields at different locations in upper (lower) arm of the interleaver. The transfer matrices corresponding to the first directional coupler, the unbalanced arms and the second directional coupler can be written as:

$$\begin{bmatrix} E_{12} \\ E_{22} \end{bmatrix} = \begin{bmatrix} \cos(\kappa_1 L_{c1}) & -j \sin(\kappa_1 L_{c1}) \\ j \sin(\kappa_1 L_{c1}) & \cos(\kappa_1 L_{c1}) \end{bmatrix} \cdot \begin{bmatrix} E_{11} \\ E_{21} \end{bmatrix} \quad (2.1)$$



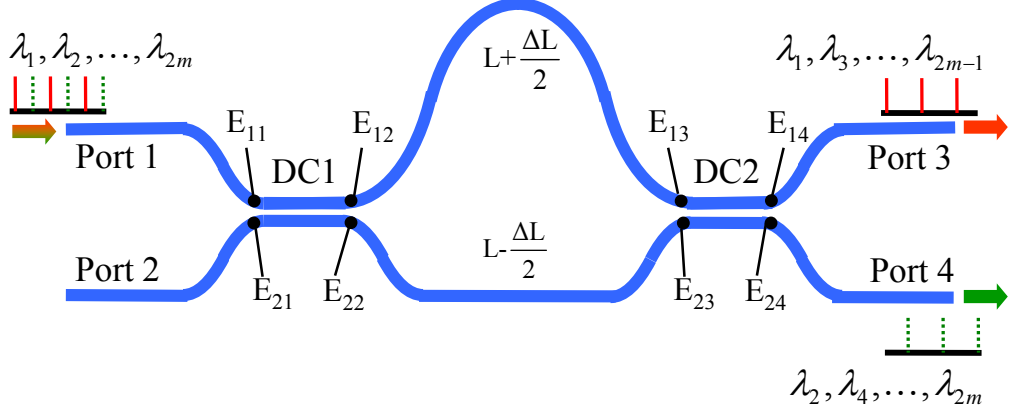


Figure 2.1: Schematic top view of an unbalanced MZI based channel interleaver. DC1 and DC2 are two identical directional couplers. Various other symbols are used for mathematical modeling (see text).

$$\begin{bmatrix} E_{13} \\ E_{23} \end{bmatrix} = e^{-j\beta L} \begin{bmatrix} \exp(-j\phi) & 0 \\ 0 & \exp(j\phi) \end{bmatrix} \cdot \begin{bmatrix} E_{12} \\ E_{22} \end{bmatrix} \quad (2.2)$$

$$\begin{bmatrix} E_{14} \\ E_{24} \end{bmatrix} = \begin{bmatrix} \cos(\kappa_2 L_{c2}) & -j \sin(\kappa_2 L_{c2}) \\ j \sin(\kappa_2 L_{c2}) & \cos(\kappa_2 L_{c2}) \end{bmatrix} \cdot \begin{bmatrix} E_{13} \\ E_{23} \end{bmatrix} \quad (2.3)$$

In the above set of equations  $L_{c1}$  ( $L_{c2}$ ) and  $\kappa_1$  ( $\kappa_2$ ) are the coupling length and the coupling coefficient of the first (second) directional coupler, respectively. The length of two arms between directional couplers are  $L + \frac{\Delta L}{2}$  and  $L - \frac{\Delta L}{2}$ , respectively. It is also assumed that both the waveguides are single-mode guiding and identical, having propagation constants of  $\beta = \frac{2\pi n_{eff}}{\lambda}$ , where  $n_{eff}$  as the effective index of the guided mode at  $\lambda$ . Thus, the acquired phase difference due to the unbalanced arms of MZI is  $2\phi = \beta\Delta L$ . For  $E_{21} = 0$  and  $\kappa_1 L_{c1} = \kappa_2 L_{c2} = \frac{\pi}{4}$  (required for 3 dB power splitting), it can be shown that the powers in Port 3 and Port 4 are proportional to  $\cos^2 \phi$  and  $\sin^2 \phi$ , respectively (see Appendix A.1). Since  $\phi$  is function of  $\lambda$ , the response of the device as a function of wavelength is periodic in either ports. It can be proved by couple mode theory that the phase introduced by a directional coupler to the signal in the coupled waveguide is exactly  $\frac{\pi}{2}$ . Taking this fact into account, an incoming DWDM channel  $\lambda_i$  would appear in Port 3 and neighboring channel  $\lambda_{i+1}$  in Port 4, if  $\beta_i \Delta L = (2m + 1)\pi$  and  $\beta_{i+1} \Delta L = 2m\pi$  are satisfied ( $m$  is an integer). Therefore,  $\Delta L$  serves as the main determining factor for designing interleaver with desired channel

spacing  $\Delta\lambda = |\lambda_{i+1} - \lambda_i|$ . The path length difference  $\Delta L$  between the two arms of the MZI can then be expressed as (see Appendix A.1):

$$\Delta L = \frac{\lambda_i \lambda_{i+1}}{2n_g \Delta\lambda} \quad (2.4)$$

where, the group index  $n_g$  is defined by:

$$n_g = n_{eff} - \lambda \frac{dn_{eff}}{d\lambda} \quad (2.5)$$

It is evident from Eq. 2.4 that for designing interleaver to separate DWDM channels uniformly with desired channel spacing  $\Delta\lambda$ , the required  $\Delta L$  depends on the group refractive index ( $n_g$ ) of the guided mode. Therefore, in order to obtain better device characteristics, dispersion-free waveguide structure with single-mode guiding, accurate design of directional couplers with wavelength independent 3-dB power splitting and low-loss s-bend waveguides are desired. Each of these will be discussed separately in following sections.

## 2.2 Single-mode Waveguides

Typical cross-section of a silicon waveguide in SOI platform has been shown in Fig. 2.2. Four different single-mode waveguides namely photonic wire waveguide (PhWW), photonic wire rib waveguide (PhWRW), reduced cross-section rib waveguide (RCRW) and large cross-section rib waveguide (LCRW) were studied. The cross sectional geometries of these waveguide structures are obtained by scaling the waveguide width  $W$ , height  $H$  and slab height  $h$  (see Table 2.1). The dimensions were carefully chosen from the published literatures demonstrating various functional silicon photonic devices [57]-[58], [63]-[64]. Wavelength dependent group index variation for guided fundamental modes have been presented in Fig. 2.3. Clearly, the photonic wire waveguide structures are highly dispersive, while RCRW and LCRW are less dispersive. The group index dispersion  $\left(\frac{dn_g}{d\lambda}\right)$  at  $\lambda = 1550$  nm for TE polarizations are estimated to be  $-10^{-5}$  /nm and  $-3.5 \times 10^{-6}$  /nm for RCRW and LCRW, respectively (see Table

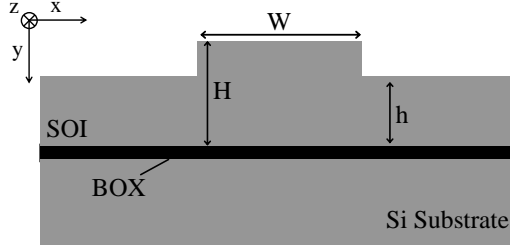


Figure 2.2: Schematic cross-sectional view of a typical silicon waveguide structure. The controlling parameters for single-mode guiding are waveguide width  $W$ , height  $H$  and slab height  $h$ . The bottom and top claddings are considered to be buried oxide ( $\text{SiO}_2$ ) and air, respectively.

Table 2.1: Classification of SOI waveguides based on cross-sectional dimension.

Waveguide	Parameters [ $\mu\text{m}$ ]	Reference
PhWW	$W = 0.50, H = 0.22, h = 0.00$	[63, 65]
PhWRW	$W = 0.50, H = 0.22, h = 0.05$	[66, 67]
RCRW	$W = 1.30, H = 2.00, h = 0.80$	[57, 68]
LCRW	$W = 5.00, H = 5.00, h = 3.20$	[58, 64]

2.2). These calculations were carried out considering material dispersion characteristics of silicon using Sellmeier's coefficients [69]. The group index variation for bulk silicon is  $-3 \times 10^{-6} / \text{nm}$ , clearly suggesting that the waveguide dispersion is negligible for LCRW structures and total dispersion is dominated by material properties of silicon. It is worth to mention here that the group index dispersions for TM polarization also show a similar trend for all four waveguide geometries. Moreover, the waveguide birefringence of SOI based structures can result in different values of  $\Delta L$  for TE and TM polarizations, and consequently affect the device response. Calculated waveguide birefringence ( $n_{eff}^{\text{TE}} - n_{eff}^{\text{TM}}$ ) and guided fundamental mode sizes for TE polarization are given in Table 2.2. Clearly, the sub-micron structures are strongly polarization dependent while the RCRW and LCRW structures are relatively less polarization sensitive. Besides, the guided fundamental mode size of LCRW structures (for both polarizations) is found to be comparable to that of standard single-mode fibers (mode-field diameter  $\sim 10.4 \mu\text{m}$ ). Hence, LCRW structures have been chosen for realizing DWDM device that require uniform response across entire optical communication band.

The waveguide dimensions for LCRW structures ( $W = 5 \mu\text{m}$ ,  $H = 5 \mu\text{m}$  and  $h = 3 - 4 \mu\text{m}$ ) have been chosen according to Soref's single-mode condition [64] and

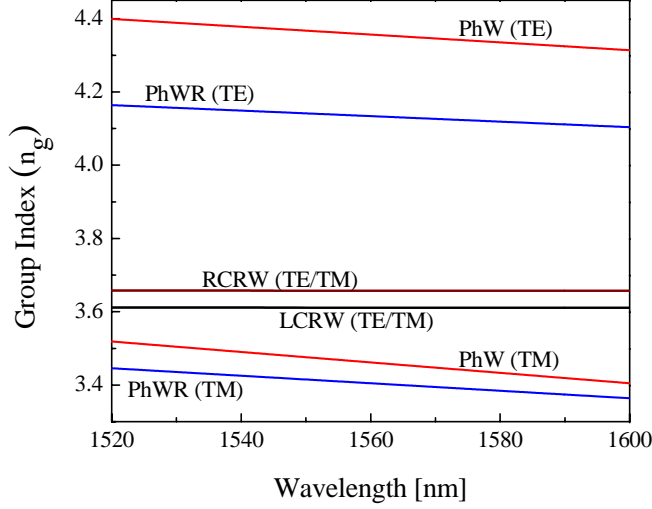


Figure 2.3: Group index as a function of wavelength for various single-mode waveguide structures in SOI platform.

Table 2.2: Group index dispersion slopes, waveguide birefringence and, mode-size for various waveguide structures at  $\lambda = 1550$  nm.

Waveguide	$\left(\frac{dn_g}{d\lambda}\right)$ [nm <sup>-1</sup> ], (TE)	$n_{eff}^{TE} - n_{eff}^{TM}$	Mode-size [ $\mu\text{m} \times \mu\text{m}$ ], (TE)
PhWW	$-9.48 \times 10^{-4}$	0.7	$0.30 \times 0.22$
PhWRW	$-6.38 \times 10^{-4}$	0.8	$0.32 \times 0.22$
RCRW	$-2.27 \times 10^{-5}$	$-6 \times 10^{-6}$	$1.3 \times 1.5$
LCRW	$-3.48 \times 10^{-6}$	$-2 \times 10^{-4}$	$6.2 \times 4.2$

prior experimental investigations in our labs [58]. The Soref's condition is assumed to be valid for both TE and TM polarization around  $\lambda = 1550$  nm:

$$\frac{W}{H} \leq 0.3 + \frac{r}{\sqrt{1-r^2}}; \quad r = \frac{h}{H} \geq 0.5; \quad W, H > \lambda \quad (2.6)$$

It is also necessary that the chosen waveguide dimensions ensure low bend-induced losses and fiber-to-waveguide coupling losses. The losses in bend waveguides can broadly be classified into two categories - scattering loss and bend-induced radiation losses [58]. The scattering losses are due to interaction of guided mode with the waveguide side-wall roughness. The radiation losses are due to extended evanescent tail (weaker mode confinement) at the outer edge of bend (Fig. 2.4(a)). Moreover, radiation losses also occur due to localized mode-mismatch at the waveguide transitions (straight-bend, bend-bend, straight-bend) [58]. The bend-induced losses as a function

of bend radius for three different values of  $r = h/H$  (0.75, 0.65 and, 0.55) are shown in Fig. 2.4(b). Clearly, the radiation loss in bend waveguides increases with, decrease in bending radius ( $R$ ) and, increase in waveguide parameter  $r$ . These bend-induced ra-

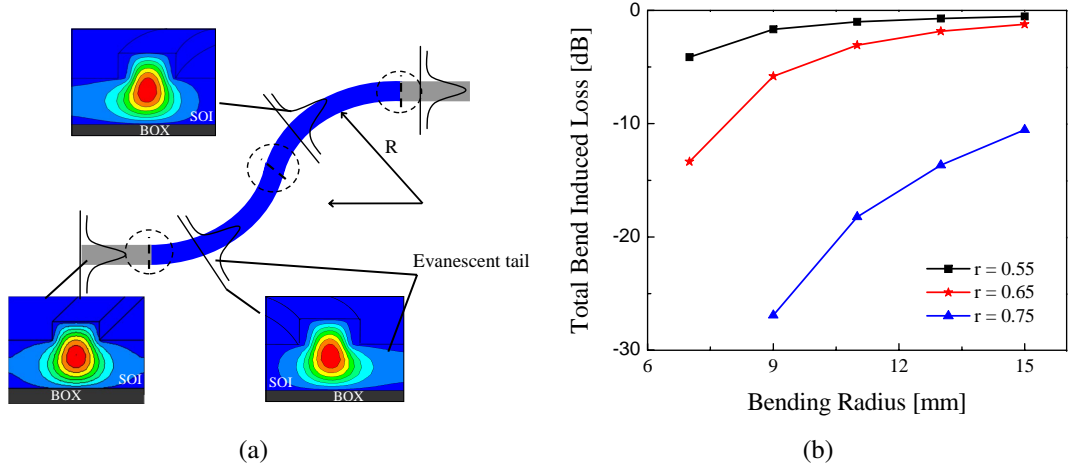


Figure 2.4: (a) Schematic of a s-bend waveguide structure and its mode-field distribution at different points. (b) Bend induced loss as a function of bending radius using  $r$  as a parameter. Waveguide width  $W = 5 \mu\text{m}$  and height  $H = 5 \mu\text{m}$  are considered for the calculations.

radiation losses in s-bend waveguides are mainly dictated by spreading of guided mode in horizontal direction - wider the spread (see Fig. 2.6(a)), higher the loss. The calculated  $\frac{1}{e}$  full width ( $\omega_x$ ) at the widest mode spread of guided mode as a function of  $W$  (up to single-mode cut-off width) for three different values of  $r$  and given  $H = 5 \mu\text{m}$  (commercially available), are shown in Fig. 2.5. It has been observed that  $\frac{1}{e}$  full width in vertical direction remains nearly unchanged ( $\omega_y \sim 3.9 \mu\text{m}$ ) as a function of  $W$  (and  $r$ ) since  $H$  is fixed at  $5 \mu\text{m}$ . For a given values of  $r$  and  $H$ , the tightest lateral mode confinement (or minimum horizontal mode-spread  $\omega_x^{min}$ ) occurs at an optimum waveguide width ( $W^{opt}$ ). Again,  $\omega_x^{min}$  reduces as the  $r$  value reduces. The minimum horizontal mode-spread ( $\omega_x^{min}$ ), corresponding optimum waveguide width ( $W^{opt}$ ), fiber-to-waveguide mode overlap ( $\Gamma$ ) and minimum affordable waveguide bending radius derived from Fig. 2.5 have been presented in Table 2.3. It is evident that the minimum affordable bending radius decreases as the  $r$  value decreases. This can certainly ensure smaller device footprints. However, it has been experimentally observed that for  $r < 0.6$  the waveguide propagation losses increases drastically ( $> 2.5 \text{ dB/cm}$ ) [58]. Again, for  $r > 0.7$ , the minimum affordable bending radius is relatively high because

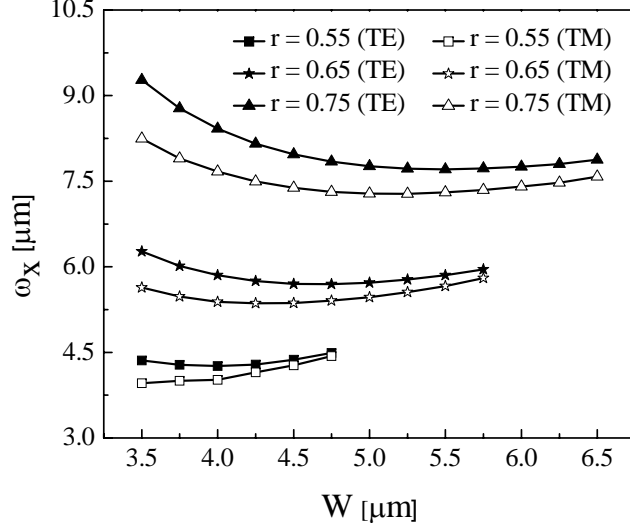


Figure 2.5: Maximum horizontal mode-spread  $\omega_x$  ( $\frac{1}{e}$  full width), as a function of waveguide width (upto single-mode cut-off) for three different values of  $r = \frac{h}{H}$ , at  $\lambda = 1550$  nm. The calculations are carried out for  $H = 5$   $\mu\text{m}$ .

Table 2.3: Fiber-Waveguide mode overlap ( $\Gamma$ ) and affordable waveguide bending radius ( $R$ ) calculated from Fig. 2.5 for TE polarization

$r$	$\omega_x^{min}$ [ $\mu\text{m}$ ]	$W^{opt}$ [ $\mu\text{m}$ ]	$\Gamma$ [%]	$R$ [ $\mu\text{m}$ ]
0.75	7.7	5.5	74	>28000
0.65	5.8	5.0	72	>15000
0.55	4.2	4.0	60	>11000

of the larger horizontal mode-spread. Therefore,  $r \sim 0.65$  has been chosen to obtain acceptable waveguide loss ( $< 1$  dB/cm), affordable bend induced loss ( $\sim 1$  dB) and reasonable fiber-to-waveguide coupling efficiency (72 %). The fiber-to-waveguide coupling efficiency is estimated by calculating overlap integral ( $\Gamma$ ) between single-mode fiber and waveguide mode-field distributions at  $\lambda = 1550$  nm (see Fig. 2.6(a) & 2.6(b)). The mode overlap ( $\Gamma$ ) is calculated according to Eq. 2.7 [42]

$$\Gamma = \frac{\int_{-\infty}^{\infty} \int_{-\infty}^{\infty} E_f(x, y) \cdot E_w(x, y) dx dy}{\left( \int_{-\infty}^{\infty} \int_{-\infty}^{\infty} (E_f(x, y))^2 dx dy \cdot \int_{-\infty}^{\infty} \int_{-\infty}^{\infty} (E_w(x, y))^2 dx dy \right)^{\frac{1}{2}}} \quad (2.7)$$

where,  $E_w(x, y)$  is the mode-field distributions in a z-propagating waveguide, while  $E_f(x, y)$  is the gaussian mode-field distribution in a z-propagating single-mode fiber.

For our chosen values of waveguide parameters ( $W = 5$   $\mu\text{m}$ ,  $H = 5$   $\mu\text{m}$  and,  $h = 3.2$   $\mu\text{m}$ ), the computed group refractive indices and mode field distributions for

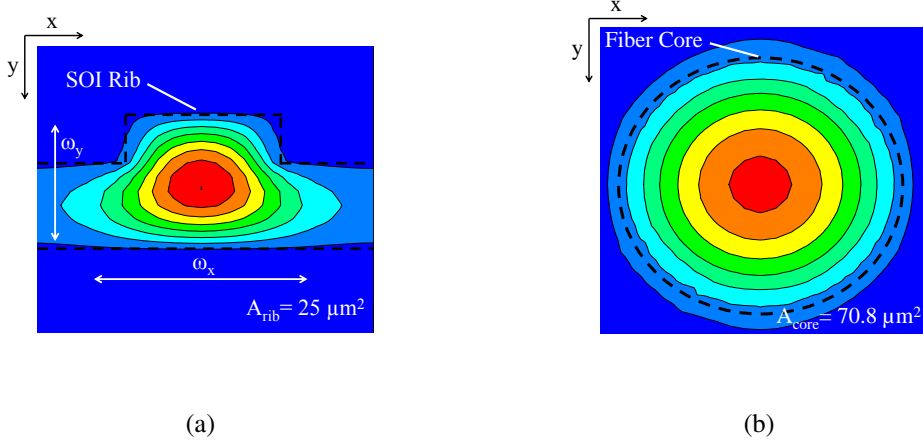


Figure 2.6: (a) Typical mode-field distribution ( $E_w(x, y)$ ) in LCRW structure (TE polarization). (b) Mode-field distribution ( $E_f(x, y)$ ) in a single-mode fiber ( $LP_{00}$  mode).

TE (TM) polarization are  $3.61120$  ( $3.61103$ ) and  $6.2 \mu\text{m} \times 4.2 \mu\text{m}$  ( $5.6 \mu\text{m} \times 3.8 \mu\text{m}$ ), respectively. These values are nearly wavelength independent in the desired communication window of  $\lambda = 1520 - 1600 \text{ nm}$ . The slight polarization dependency is due to the asymmetric geometry of the rib waveguide structure, which can affect the overall performance of device.

It is evident from Table 2.2 that, most of the waveguide structures are polarization sensitive. Hence, it becomes necessary to ensure that the device is operated in either of the two polarizations. Again, it has been theoretically studied and investigated that bend waveguides tend to induce some polarization rotations (see Fig. 2.7) [70, 71]. The resulting degradation in polarization extinction can also affect the optimum performance of the device. Therefore, it is necessary to have an integrated on-chip polarizer.

It is known that metal cladding over a dielectric waveguide structure attenuates guided light having dominant electric field component normal to the cladding [72]-[74]. Schematic of a metal-coated rib waveguide structure is shown in Fig 2.8. Here, the buried oxide layer acts as the lower cladding while upper cladding is air - except top of the rib, which is metal coated. We have assumed that the single-mode guiding condition mentioned in Eq. 2.6 is also valid in this case. It is worth mentioning here that, guided TE polarized light for such rib waveguide contains dominant field components  $E_x$ ,  $H_y$  and  $H_z$  whereas, TM polarized light has components  $H_x$ ,  $E_y$  and  $E_z$ . The attenuation mechanism of TM-polarized light in a metal clad waveguide structure can

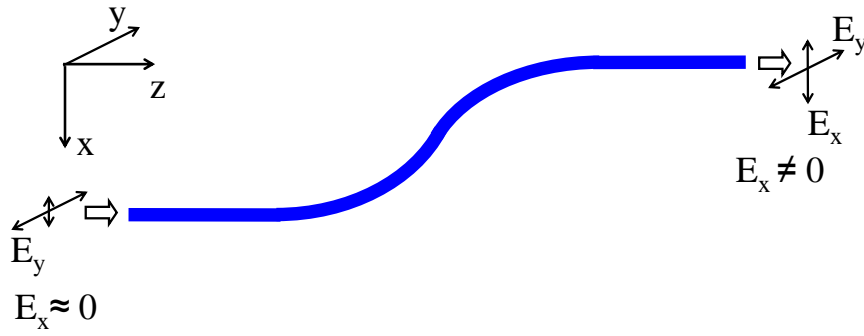


Figure 2.7: Schematic representation of degradation in polarization extinction in a s-bend waveguide structure.  $E_x$  and  $E_y$  are the two orthogonal electric field components.

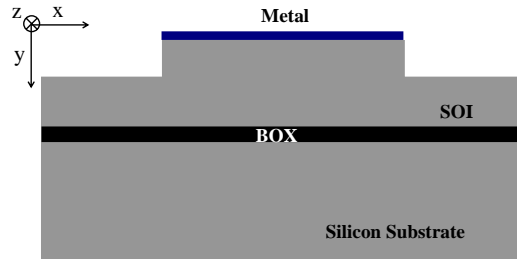


Figure 2.8: Schematic of a metal-clad SOI rib waveguide structure.

then be explained from the principle of excitation of surface plasmon polariton at the metal-dielectric interface. These surface plasmon polaritons are excited because of the coupling between electromagnetic wave and the surface current (at optical frequencies). The overlap between evanescent field of the guided mode and plasma cloud of the metal gives rise to surface current. This surface current can arise for both the polarizations. However, the specific boundary conditions for TM polarization satisfy to excite SPP, whereas the TE polarization does not have a feasible solution for the same [75]. If the thickness of metal cladding is higher than the skin depth, the energy of SPP undergoes ohmic losses resulting into an ultimate attenuation of guided light as it propagates. The quantitative loss due to metal cladding can be approximately estimated using effective index method [42, 76]. Metals at optical frequencies are known to possess complex refractive index. The imaginary part of refractive index (known as extinction co-efficient) for these metals is directly responsible for absorption of the guided light. Effective in-



dex solution for such a metal-clad dielectric waveguide has eigen mode solutions with complex propagation constants, which are responsible for its overall attenuation.

The above mentioned attenuation can be estimated more accurately by BPM simulation. We have used RSoft BPM solver to study absorption characteristics of various metal claddings (Al/Cr/Au) for the structure shown in Fig. 2.8. The refractive indices considered for Al, Cr and Au at  $\lambda = 1550$  nm are  $1.55 - 15.31j$ ,  $4.27 - 4.93j$ , and  $0.55 - 11.5j$ , respectively [77]. The simulation results show that TM-polarized light extinguishes as length of metal claddings increases, whereas the TE polarized light remains almost un-attenuated (see Fig. 2.9). As expected, Al cladding provides better extinction because of the large imaginary part of its refractive index.

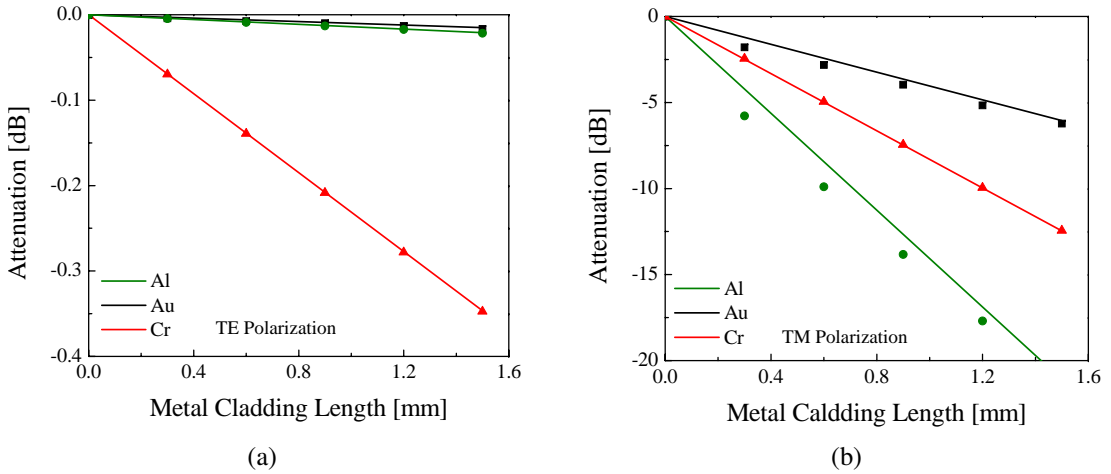


Figure 2.9: (a) Simulated attenuation of TE polarization as a function of metal cladding length. (b) Simulated attenuation of TM polarization as a function of metal cladding length. The solid lines are the exponential fits of the computed results correspond to Au, Cr and Al.

Based on BPM simulation results an empirical equation is formulated for finding the attenuation ( $\alpha$ ) of TM-polarized light as a function of length ( $l$ ):

$$P_{TM} = P_O \cdot \exp(-\alpha \cdot l) \quad (2.8)$$

Here,  $P_O$  is the launched TM power while,  $P_{TM}$  is the transmitted TM polarized light after traveling through a metal clad waveguide of length  $l$ . The values of  $\alpha$  obtained for the empirical fits are  $\alpha_{Al} = 3.5 \text{ mm}^{-1}$  ( $\sim 15 \text{ dB/mm}$ ),  $\alpha_{Cr} = 1.8 \text{ mm}^{-1}$  ( $\sim 7.8 \text{ dB/mm}$ ) and  $\alpha_{Au} = 0.77 \text{ mm}^{-1}$  ( $\sim 3.34 \text{ dB/mm}$ ), respectively. It is worth

mentioning here that the attenuation profile of launched TE-polarized light also follows a similar formula for power attenuation; however, the attenuation coefficient is negligibly small (nearly 10 times smaller than that of TM-polarized light). The extinction ratio of TM-polarized light is estimated by:

$$\delta_{ex}[dB] = 10 \cdot \log_{10} \left( \frac{P_{TM}}{P_{TE}} \right) \quad (2.9)$$

Typically, an extinction of TM polarized light due to Al cladding is estimated to be  $\sim 15$  dB/mm.

## 2.3 Directional Coupler

As mentioned in Section 2.1, the proposed interleaver structure has two identical directional couplers (3-dB power splitters). Basically, a directional coupler consists of two single-mode waveguides in close proximity of each other (see Fig. 2.10). When

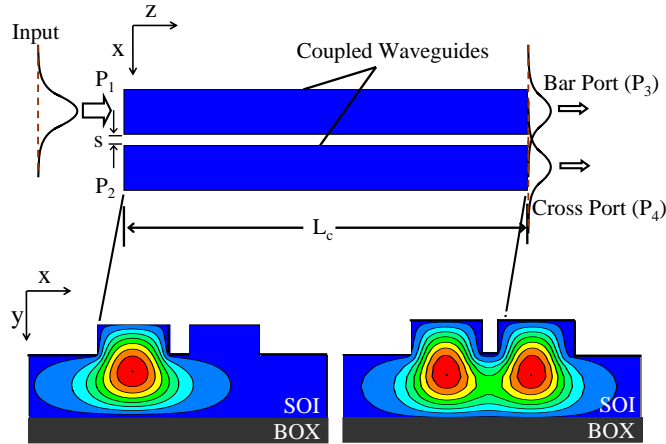


Figure 2.10: Schematic top view of coupled waveguides in a directional coupler (3-dB power splitter) with input and output field distributions.  $L_c$  - 3-dB coupling length and  $s$  - waveguide spacing.

the waveguide separation is small, evanescent tails of the guided mode of one waveguide overlap with the guided mode of second waveguide causing coupling of power in the later. The depth of penetration of evanescent tail depends on the effective index of the material between the two closely placed waveguides. Four different directional

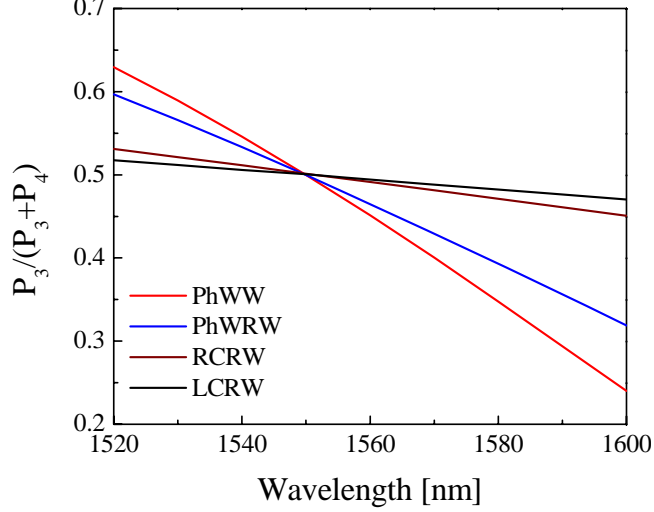


Figure 2.11: Splitting ratio as a function of wavelength for various waveguide structures. The coupling length are chosen for 3 – dB splitting of TE polarized light at  $\lambda = 1550$  nm.

couplers were designed using four waveguide geometries (PhWW, PhWRW, RCRW, LCRW). The spacings between two coupled waveguides for PhWW, PhWRW, RCRW and, LCRW based directional couplers are suitably chosen as  $0.3 \mu\text{m}$ ,  $0.3 \mu\text{m}$ ,  $1 \mu\text{m}$  and,  $2.5 \mu\text{m}$ , respectively. The corresponding 3-dB coupling lengths at 1550 nm for TE polarization are estimated to be  $101 \mu\text{m}$ ,  $27 \mu\text{m}$ ,  $269 \mu\text{m}$  and,  $1610 \mu\text{m}$ . It is found that the splitting ratio for dispersive waveguide structures (PhWW and PhWRW) vary considerably over the communication band, while the variation for RCRW and LCRW structures is  $3 \pm 0.35$  dB and  $3 \pm 0.25$  dB (least amongst all), respectively (see Fig. 2.11).

Waveguide spacing of  $\sim 2.5 \mu\text{m}$  and coupling lengths of  $\sim 1610 \mu\text{m}$  were optimized for the chosen single-mode LCRW based directional couplers. Wider waveguide spacing is not chosen as it considerably increases the coupling length and also to the overall device dimension (see Fig. 2.12(a)). In addition to this, minimum realizable feature dimension in our labs is  $\sim 2 \mu\text{m}$  and hence the chosen waveguide spacing is kept  $\sim 2.5 \mu\text{m}$ . The lithographic errors in fabrication can affect the 3-dB coupling length, which can be adjusted by controlling the etching depth. Fig. 2.12(b) shows the 3-dB coupling length as a function of etch depth upto single-mode cut-off. As the etch depth increases, the mode gets strongly confined in the rib, resulting in weaker evanescent tail interaction and longer coupling length. Moreover, the power splitting ratio of di-

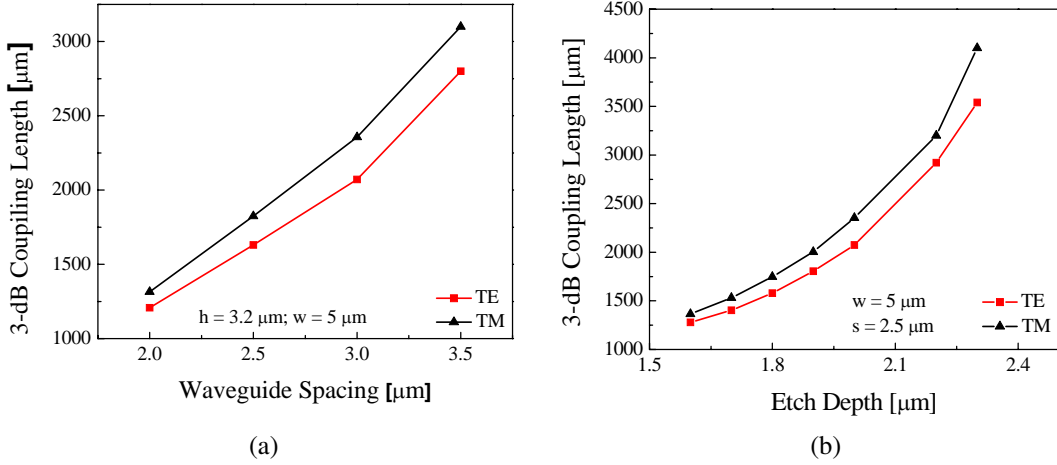


Figure 2.12: (a) 3-dB coupling length as a function of waveguide spacing. (b) 3-dB coupling length as a function of waveguide etch depth ( $H-h$ ). Simulations are carried out for  $H = 5 \mu\text{m}$ .

rectional coupler is found to be polarization dependent across the entire optical C and L band (Fig. 2.13). This is because, the mode-size of TE polarization is slightly larger than that of TM polarization. Thus, the interaction of evanescent tail for TE polarization is relatively stronger, resulting in lower coupling length. The coupled waveguides are

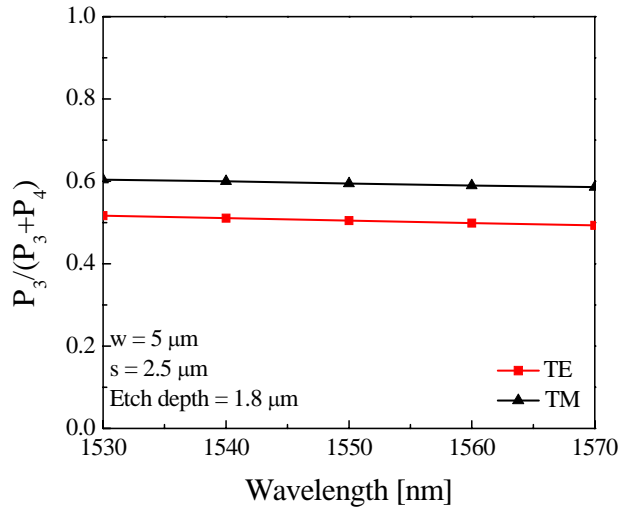


Figure 2.13: Polarization dependency of splitting ratio as a function of wavelength for directional coupler with LCRW structures. The coupling length is chosen for 3 – dB splitting of TE polarized light at  $\lambda = 1550 \text{ nm}$ .

terminated with S-bend waveguides as shown in Fig. 2.14. It must be noted that the bend waveguides also contribute in coupling as they emerge from the parallel coupled region. Accordingly, care has to be taken to reduce the central coupling length in order

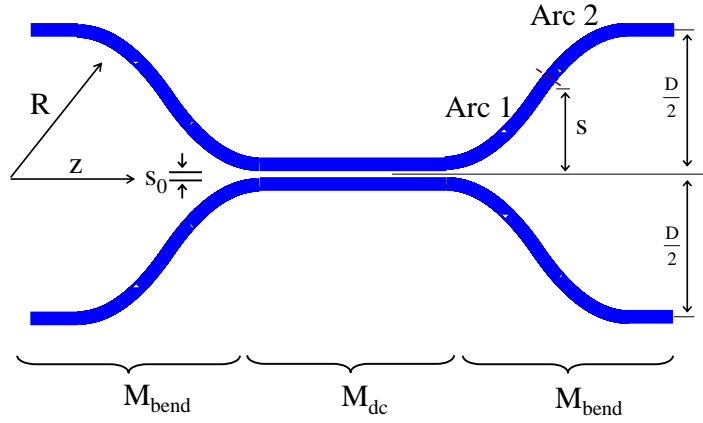


Figure 2.14: Schematic of an practical directional coupler.  $s$  is the waveguide spacing at coupler,  $s_{bend}$  is waveguide spacing at the junction of two identical arcs,  $R$  is the bending radius and  $z$  is the arc length,  $D$  is the output waveguide spacing.

to achieve precise 3-dB power splitting. This can be corrected by modifying the transfer matrices given in Eqs. 2.1 & 2.3. Each of the directional couplers can then be dissolved into three sections the bend regions at the input and the output side ( $M_{bend}$ ), and the central coupling region ( $M_{dc}$ ) (see Fig. 2.14). Transfer matrix for the central coupler section remains the same as in Eq. 2.1 and 2.3 while the  $M_{bend}$  can be given as below:

$$M_{bend} = \begin{bmatrix} \cos(\delta) & -j \cdot \sin(\delta) \\ -j \cdot \sin(\delta) & \cos(\delta) \end{bmatrix} \quad (2.10)$$

Here, the coupling coefficient ( $\delta$ ), is a function of propagation length inside the bend and can be given as below:

$$\delta = \int_0^{z_c} \kappa(z) dz \quad (2.11)$$

The interaction of guided mode in the emanating waveguide gradually becomes weak as the waveguide spacings increases and vice-versa. From Fig. 2.14 the geometrical function for emanating waveguides can be written as below.

$$s(R, z) = \frac{s_0}{2} + \left( R - \sqrt{R^2 - z^2} \right) \quad (2.12)$$

where,  $s_0$  is the waveguide spacing at the coupler end,  $R$  is the bending radius and  $z$  is the length. Typically, an S-bend structure is formed using two identical arcs with angles

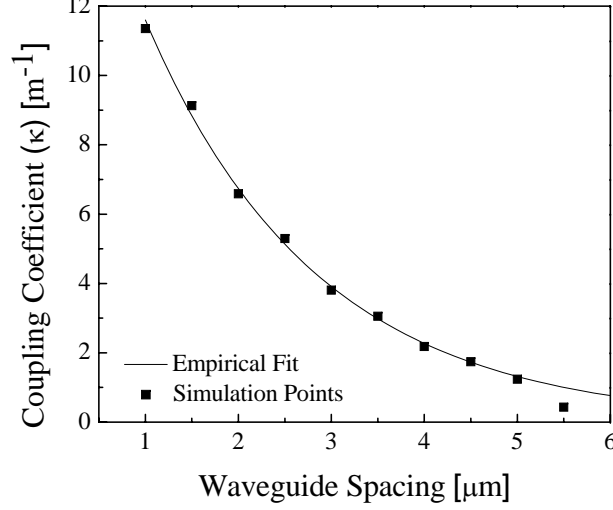


Figure 2.15: Coupling coefficient ( $\kappa$ ) as a function of waveguide spacings.

(i.e.  $\theta_{arc1} = 0$  to  $\theta_f$  and  $\theta_{arc2} = \theta_f$  to  $0$ ). The values of coupling coefficient  $\kappa$ , then as a function of waveguide spacing is shown in Fig. 2.15. The  $\kappa$  is calculated using the solution obtained from coupled mode theory given by [78]:

$$\kappa = \frac{\frac{\omega \epsilon_0}{4} \int_{-\infty}^{\infty} \int_{-\infty}^{\infty} E_1(x, y) \Delta n^2 E_2^*(x, y) dx dy}{\frac{\beta}{2 \cdot \omega \mu_0} \int_{-\infty}^{\infty} \int_{-\infty}^{\infty} E_1(x, y) E_2^*(x, y) dx dy} \quad (2.13)$$

where,  $\Delta n^2 = (n_{core})^2 - (n_{clad})^2$  in core area and,  $\Delta n^2 = 0$  elsewhere.

Here,  $E_1(x, y)$  and  $E_2(x, y)$  are the mode field distributions inside the two coupled waveguides, while  $\omega$  and  $\beta$  are the frequency and propagation constant of the propagating optical mode. The fundamental mode field distribution inside a bend waveguide is computed using RSoft-FEM tool. The empirical solution for the computed  $\kappa$  value is shown in Eq. 2.14.

$$\kappa(s) = A \cdot \exp(-B \cdot s) \quad (2.14)$$

where,  $A = 19.98 \text{ m}^{-1}$  and  $B = 0.5437 \text{ } \mu\text{m}^{-1}$ . Then,  $\kappa$  as a function of length  $z$  for a given value of  $R$  can be obtained using Eq. 2.12 and 2.14 as below:

$$\kappa(z) = A \cdot \exp \left[ -B \cdot \left\{ \frac{s_0}{2} + \left( R - \sqrt{R^2 - z^2} \right) \right\} \right] \quad (2.15)$$

BPM and matlab simulations reveal that the coupling length for directional coupler with emanating s-bend waveguides of geometrical dimensions  $W = 2.5 \text{ } \mu\text{m}$ ,  $H = 5 \text{ } \mu\text{m}$ ,

$h = 3.2 \mu\text{m}$  and  $R = 15 \text{ mm}$  reduces by  $\sim 200 \mu\text{m}$ .

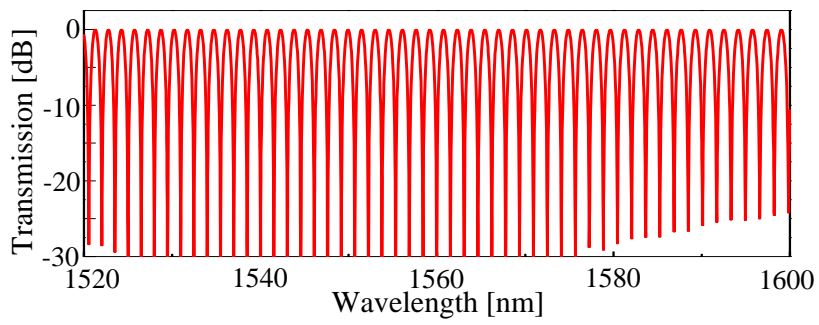
## 2.4 Interleaver Design

The final design of interleaver is made considering the above discussed and optimized waveguide parameters. The final design parameters are tabulated in Table 2.4. The design details are mentioned for interleaving channels in 100 GHz DWDM grid. While considering the design of  $\Delta L$  using Eq. 2.4,  $\lambda_1$  and  $\lambda_2$  are chosen as the two successive channels 1550.9 nm and 1551.7 nm, respectively. The  $\Delta L$  estimated using effective index for TE polarizations is mentioned. The output waveguides are kept  $250 \mu\text{m}$  apart in order to allow efficient fiber pigtailling. Due to the slight polarization dependency of

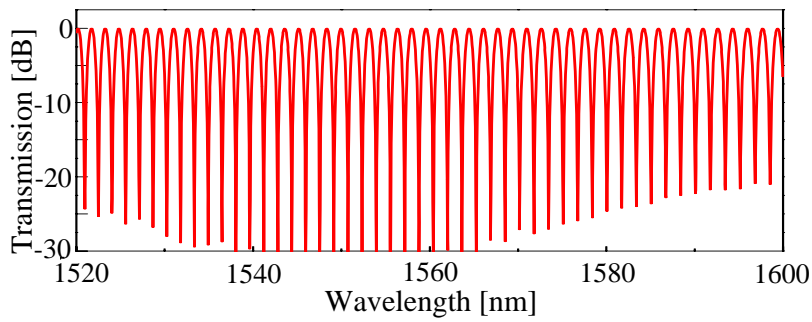
Table 2.4: Final design specifications for 100 GHz DWDM channel interleaver (channel spacing  $\Delta\lambda = 0.8 \text{ nm}$  ).

$W = 5 \mu\text{m}$	Waveguide Spacing = $2.5 \mu\text{m}$
$h = 3.2 \mu\text{m}$	Coupling Length = $1400 \mu\text{m}$
Bending Radius (R) = $15000 \mu\text{m}$	$\Delta L = 415.38 \mu\text{m}$
Device Length = $\sim 2.9 \text{ cm}$	Operation Band = C and L

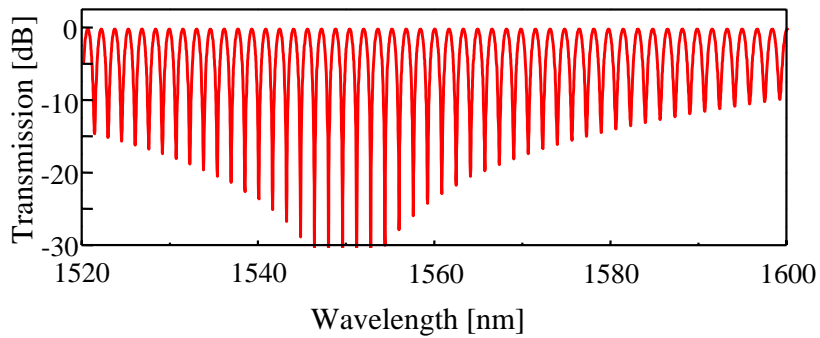
the single-mode LCRW structures, length of directional coupler ( $L_{3db}$ ) and asymmetric arm of MZI ( $\Delta L$ ) for TM polarization were found to be  $1700 \mu\text{m}$  and  $415.38 \mu\text{m}$ , respectively. The Fig. 2.16(a) shows simulated transmission characteristics of LCRW based interleaver obtained using transmission matrix theory (see Section 2.1) and incorporating the variation in effective index and coupling coefficient  $\kappa$ . As a comparison, Fig. 2.16 also shows the calculated transmission characteristics in TE polarization for PhWW, PhWRW and, RCRW based interleaver over the entire optical C+L band. The degradation of inter-channel extinction at the band-edges ( $\lambda \sim 1520 \text{ nm}$  and  $\lambda \sim 1600 \text{ nm}$ ) is clearly evident in case of PhWW, PhWRW and RCRW based interleavers and thus making LCRW based interleaver an obvious choice for realizing dispersion-free device. The degradation of channel extinction in case of PhWW, PhWRW and RCRW based interleaver is due to non-uniform power splitting ratio of directional coupler across the operational band. Moreover, channel chirping is also observed in characteristic response of dispersive interleaver structures. Thus, reducing the operational band of the device with channel extinction  $> 25 \text{ dB}$  and  $\Delta\lambda = 0.8 \text{ nm}$ . In



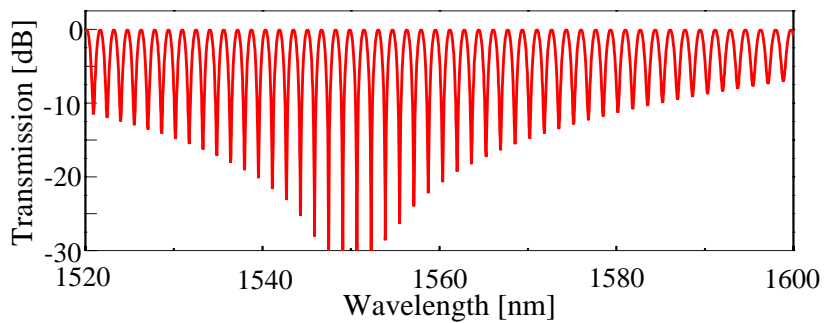
(a)



(b)



(c)



(d)

Figure 2.16: Wavelength dependent transmission characteristics at Port 3 (bar port) of interleaver with various waveguide cross sections. (a) Interleaver with LCRW structure, (b) interleaver with RCRW structure, (c) interleaver with PhWRW structure and, (d) interleaver with PhWW structure. The characteristics shown here are for TE polarization.



case of dispersion-free LCRW structures, the group index variation due to waveguide inhomogeneities (if any) is found to be negligibly small:  $\frac{dn_g}{dh}\Big|_{W=5\ \mu\text{m}} = 10^{-4} / \mu\text{m}$  and  $\frac{dn_g}{dW}\Big|_{h=3.2\ \mu\text{m}} = 4.8 \times 10^{-5} / \mu\text{m}$ . Thus, the performance of LCRW based interleavers is less susceptible to fabrication errors.

The interleaver characteristics for single-mode LCRW based interleaver though dispersion-free are slightly polarization dependent as expected from the prior analysis. Wavelength dependent transmission characteristics of LCRW based interleaver around  $\lambda = 1550\ \text{nm}$  is shown in Fig. 2.17 for TE and TM polarization. The shift in resonance peaks at the two output ports for TE and TM polarization is due to waveguide birefringence ( $n_{eff}^{TE} - n_{eff}^{TM} = -2 \times 10^{-4}$ ). It can be shown from Eq. 2.4 that, this small waveguide birefringence has negligible influence on  $\Delta\lambda = |\lambda_{i+1} - \lambda_i|$ , however, it can affect the position of resonance peaks ( $\delta\lambda = \lambda_r^{TE} - \lambda_r^{TM} \sim 100\ \text{pm}$ ). But, interleaver designed to operate in TE polarization (at  $T = 27\ ^\circ\text{C}$ ) can be reconfigured to operate in TM polarization if the device operating temperature is tuned by  $\pm 2\ ^\circ\text{C}$ . The temperature tuning characteristics of interleaver response has been shown in Fig. 2.18, assuming temperature coefficient of refractive index change  $\frac{dn}{dT} = -1.86 \times 10^{-4} / \text{K}$  [42]. It has been theoretically estimated that the shift in resonance peaks as function of temperature is  $\sim 0.1\ \text{nm}/^\circ\text{C}$ . Polarization independent interleaver is very important in fiber optic communication systems. Designing such an interleaver requires design of polarization independent single-mode waveguides and directional couplers.

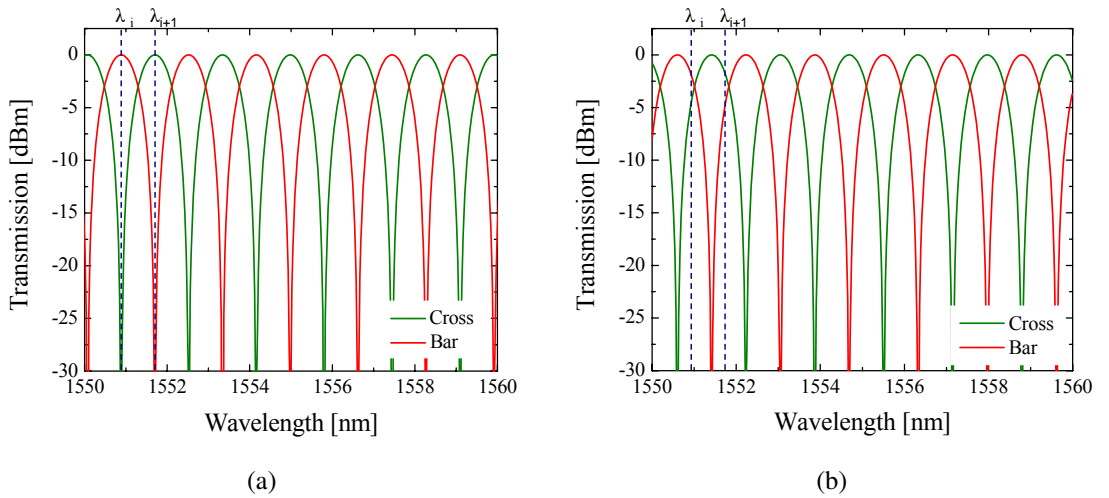


Figure 2.17: Simulated transmission characteristics for two orthogonal polarizations, (a) TE polarization, and (b) TM polarization. The vertical markers denote two successive ITU channels at  $\lambda_i = 1550.9\ \text{nm}$  and  $\lambda_{i+1} = 1551.7\ \text{nm}$ .

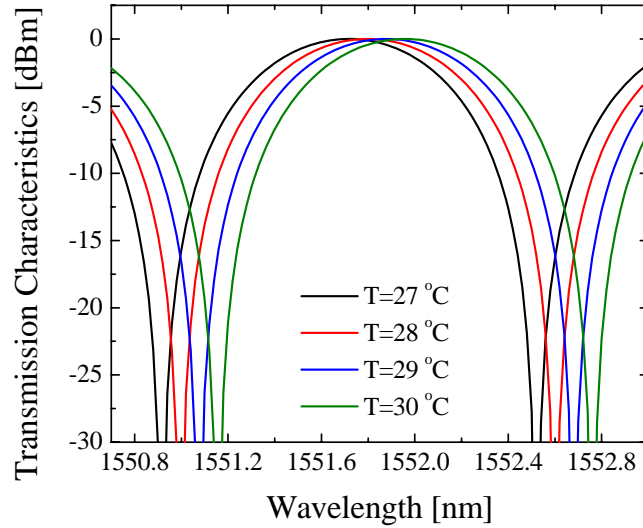


Figure 2.18: Shift in resonance peak of a particular channel at bar port (Port 3) of interleaver due to temperature variation.

## 2.5 Conclusions

Asymmetric MZI based channel interleaver was thoroughly studied using various single-mode waveguide structures. Interleaver based on single-mode LCRW structures ( $W = 5 \mu\text{m}$ ,  $h = 3.2 \mu\text{m}$  and  $H = 5 \mu\text{m}$ ) in SOI were found to be nearly dispersion-free in the desired optical communication band (C, L). However, LCRW based devices (directional coupler and interleavers) studied here were slightly polarization dependent. The degradation in device response due to polarization dependency can be solved by integrating an on-chip polarizer. Metal-clad waveguides were studied to improve polarization extinction in device operation. It is estimated that a metal clad waveguide of length  $\sim 1 \text{ mm}$  can improve polarization extinction by  $> 15 \text{ dB}$ . However, this is not a viable solution for fiber optic communication systems.

## CHAPTER 3

### Fabrication and Characterization

DWDM channel interleavers based on LCRW structures have been fabricated using the design parameters discussed in Chapter 2 and, subsequently they are characterized. Suitable masks were designed and fabricated for defining the device structures; details of which have been discussed in Section 3.1. The device fabrication and characterizations have been presented in Section 3.2 and 3.3, respectively. In order to improve the polarization extinction in device performance, metal-clad waveguide polarizers have been investigated and the results are presented in Section 3.3.

#### 3.1 Mask Design and Fabrication

The fabrication of proposed interleaver in SOI platform is a single mask process, but a second mask is required to integrate waveguide polarizers. The mask layouts were designed using commercial R-soft CAD tool. Basically, the mask layout consists of stripes corresponding to six waveguides as shown schematically in Fig. 3.1. Here, Wg2 and Wg3 together form an interleaver, while the other reference structures are namely, meander-bend waveguide (Wg1), directional coupler (Wg4-Wg5) and straight waveguide (Wg6). These reference structures have been included to study various parameters like waveguide loss (straight waveguide), bend-induced losses and polarization rotations (meander bend waveguide), power splitting ratio and excess loss (directional coupler). There are five such sets (S1, S2, S3, S4, and S5) in entire mask layout. These sets have interleaver structures with same value of  $\Delta L$ , but they differ by the length of directional coupler ( $L_c = 1000 \mu\text{m}$ ,  $1200 \mu\text{m}$ ,  $1400 \mu\text{m}$ , and  $1600 \mu\text{m}$ ). Overall dimension of the mask layout is  $1.3 \text{ cm}$  (width)  $\times$   $3.5 \text{ cm}$  (length). The second mask contains several rectangular structures of varying lengths ( $200 \mu\text{m}$ ,  $400 \mu\text{m}$ ,  $600 \mu\text{m}$ ,  $800 \mu\text{m}$ ,  $1000 \mu\text{m}$ , and  $1200 \mu\text{m}$ ) suitably aligned with the first mask to fabricate waveguide polarizers (see Fig. 3.2). The photolithography using second mask is to be carried out

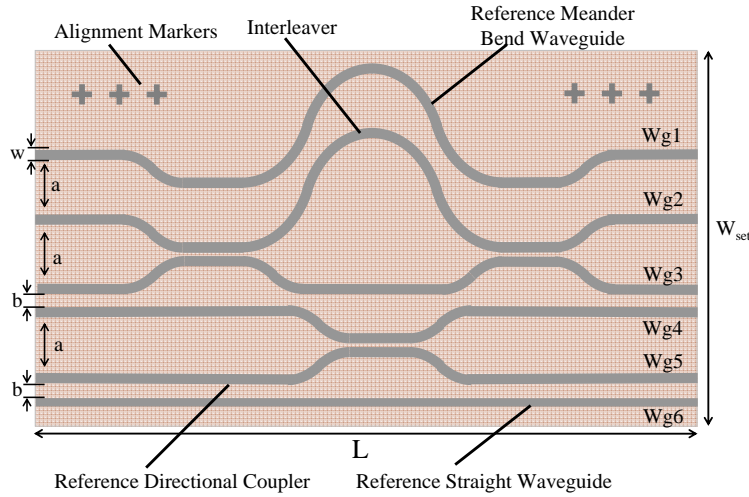


Figure 3.1: Schematic top view of one of the five sets in the interleaver mask.  $a = 250 \mu\text{m}$ ,  $b = 50 \mu\text{m}$  and  $W = 5 \mu\text{m}$ ,  $W_{set} = 2600 \mu\text{m}$  and  $L = 3.5 \text{ cm}$ .

on the waveguide samples after reactive ion etching (RIE) process and before removal of metal thin-film. A schematic top-view of the two masks aligned together is shown in Fig. 3.2.

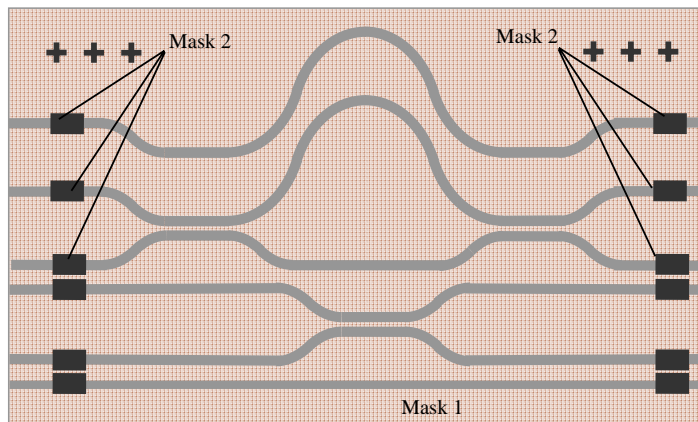


Figure 3.2: Schematic top-view of two masks aligned together.

The mask layout is transferred over a commercially acquired Cr coated ( $\sim 50 \text{ nm}$ ) mask plate ( $4'' \times 4''$  glass plate) having a thin layer ( $\sim 540 \text{ nm}$ ) of photoresist (AZP-1350). Pattern is directly written over the photoresist using UV laser writer (DWL - 66, Heidelberg Instruments GmbH, He-Cd laser source  $\lambda = 442 \text{ nm}$ ). The exposed PPR is then developed using a 0.1 molar NaOH developer solution (7 pelets NaOH in 250 ml water). The photoresist pattern is later transferred to the Cr film using Ammonium Ceric

Nitrate and Acetic Acid based etchant solution (see Appendix A.2). The undeveloped photoresist is finally removed by acetone cleaning.

## 3.2 Device Fabrication

The devices are fabricated on optical grade SOI wafers (Ultrasil Inc., USA). Detailed specifications of these wafers are listed below:

- Handle wafer thickness:  $500 \mu\text{m} \pm 25 \mu\text{m}$
- Device layer thickness:  $5 \mu\text{m} \pm 0.25 \mu\text{m}$
- Buried oxide thickness:  $1 \mu\text{m}$
- Device Layer Resistivity:  $> 5000 \Omega/\text{cm}$
- Crystal orientation:  $\langle 100 \rangle$
- Wafer diameter:  $\sim 100 \text{ mm}$

Sequential device fabrication steps are: (i) wafer cleaning, (ii) metal thin-film deposition, (iii) photolithography for waveguide definition (using mask 1), (iv) reactive ion etching and, (v) photolithography for polarizer definition (using mask 2), (vi) end-facet preparation. These fabrication process steps are schematically shown in Fig. 3.3. Each of these process steps have been discussed separately below. Towards the end of this section, a detailed summary of fabricated interleaver samples is mentioned.

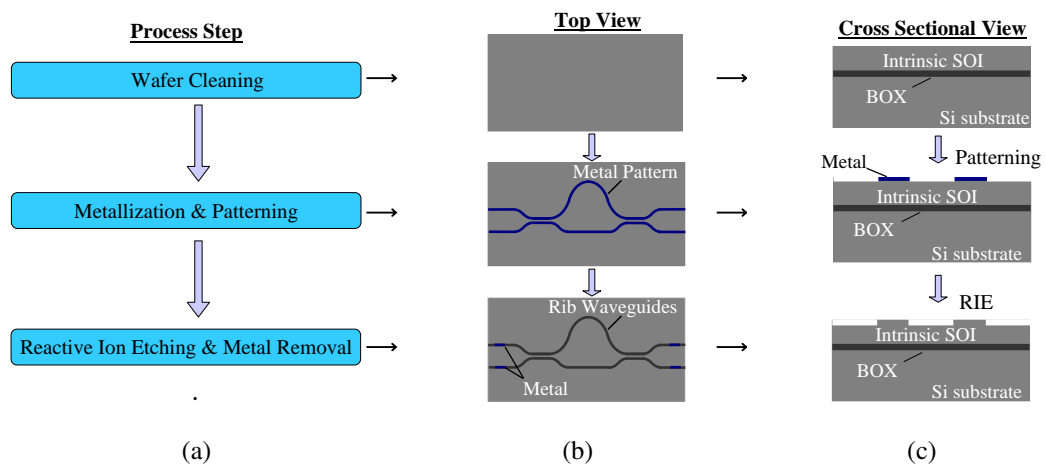
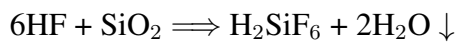
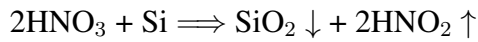


Figure 3.3: (a) Fabrication process steps. (b) Top view of of the sample SOI wafer. (c) Cross section view of the sample SOI wafer.

### (i) Wafer Cleaning

The SOI wafer with above mentioned specifications are diced/cleaved into smaller rectangular pieces ( $\sim 1.3 \text{ cm} \times 3.4 \text{ cm}$ ) to nearly accommodate the mask layout discussed in previous section as well as to fit to the dimension of sample-holder in our characterization setup. At first, samples are rigorously treated for removing any kind of organic/inorganic impurities. The organic impurities have been removed using trichloroethylene (TCE) and acetone cleaning procedures, respectively. Wafer samples are immersed in TCE and the solvent is boiled ( $\sim 55 \text{ }^\circ\text{C}$ ) in a beaker for 2-5 min. Afterwards, the samples are cleaned by immersing them in acetone with ultrasonic agitation, followed by thorough rinsing with DI water. Later, the inorganic impurities are cleaned using conc. Nitric Acid ( $\text{HNO}_3$ ). In this case, samples are immersed in  $\text{HNO}_3$  and boiled at  $\sim 55 \text{ }^\circ\text{C}$  for 5 min. Cleaning with  $\text{HNO}_3$  not only removes (dissolves) inorganic impurities but also causes growth of thin oxide layer ( $< 5 \text{ nm}$ ) on top of silicon wafer. The growth of oxide-film can be verified by hydrophilic nature of wafer surface. This oxide is removed by immersing the wafer in dil. HF solution (1 parts of HF in 10 parts of water) for  $\sim 30 \text{ s}$ . Since the growth of oxide consumes silicon from the wafer, removal of oxide exposes a fresh wafer surface suited for fabrication of devices. The chemical reactions for oxide growth and its removal are given by:



### (ii) Metal Film Deposition

Device fabrication requires metal mask for selective etching of silicon to realize rib waveguide structures. Moreover, it is also required to study the absorption characteristics of various metals for realizing efficient metal-clad TE-pass waveguide polarizer. The cleaned samples are coated with thin metal-films (Al/Au/Cr) using thin-film deposition techniques. Uniform Al coating is achieved through thermal deposition technique (System: Hydro Pneo Vac, HPVT 305G), while Au and Cr are deposited using DC sputtering technique (System: Hind-Hivac DC Sputtering). Thermal evaporation of Al is preferred due to its low atomic weight and low evaporation temperature.

In both the techniques, the chambers are evacuated to a pressure of  $< 5 \times 10^{-6}$  mbar. Low chamber pressures are particularly necessary to achieve uniform thickness of deposited metal. In case of thermal deposition, electronic-grade Al wire/piece is placed in a tungsten filament. On applying current across the filament causes its resistive heating, leading to evaporation of metal (Al) which gets deposited on the exposed wafer surface. Typically, for an Al of  $\sim 0.4$  gm, a deposition thickness of  $\sim 100$  nm is obtained on applying a DC voltage of  $\sim 80$  V. In case of DC sputtering technique, the evacuated chamber is filled up with inert gas, before applying DC bias to the metal source acting as cathode. The energized gas ions transfer their momentum on impact with Cr/Au target leading to ballistic fly-out of target metal particles, which later settles on the exposed surface of sample. In order to achieve efficient momentum transfer, sputtering gas with its atomic weight close to that of the depositing metal is often preferred. In our case, Ar was used as the sputtering gas. A constant flow of Ar through the chamber was maintained and the chamber pressure was allowed to drop from initial value of  $< 5 \times 10^{-6}$  mbar to  $\sim 5 \times 10^{-3}$  mbar. The DC bias voltage of 330 V and current of 0.25 A were maintained throughout the sputtering process and deposition rate of  $\sim 2$  nm/min was achieved.

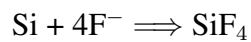
### **(iii) Photolithography for Waveguide Definition**

The mask pattern has been photolithographically transferred on the metal-coated samples. In our case, for single mask processes we have often used Cr metal coated samples. This is mainly because, it has been observed that NaOH/KOH based developer solutions used at our labs have relatively lower affinity to attack Chromium. At first, a thin layer ( $\sim 1.2$   $\mu\text{m}$ ) of positive photoresist (S1813-G) over sample surface is obtained using spin coating technique (spining speed: 6000 rpm and, angular acceleration: 600 rpm/s). The positive photoresist (PPR) coated samples are then pre-baked at 80 °C for 25 min in an oven. This is done in order to harden the PPR layer as well as to evaporate humidity content and organic solvents. The device mask is then aligned over the sample and exposed to 365 nm UV radiation for  $\sim 8$  s using a 306 W UV lamp (Mask Aligner: BA6/MA6 Suss MicroTech). The exposure to UV radiation tends to break the inter-molecular bonds of the photoresist making it soft, which can later be

removed using a NaOH/KOH based developer solution (in our case 0.1 molar NaOH). Typically, the optimized developing time is  $\sim 10-12$  s at  $25^\circ\text{C}$  temperature and, 50 % humidity for a sample exposed with UV intensity of  $5\text{ mW}/\text{cm}^2$ . The developed samples are later post-baked at  $120^\circ\text{C}$  for  $\sim 35$  min. Baking for longer time can induce cracks in the hardened PPR which can not effectively work as mask for metal patterning resulting in discontinuous waveguides. The corresponding pattern on the deposited metal film is realized by putting the sample in a suitable metal etchant (see Appendix A.2). The typical etch rate of the etchant is  $\sim 40\text{ nm}/\text{min}$ . The PPR is then removed from top of the metal patterned sample.

#### (iv) Reactive Ion Etching

The rib structures are realized by etching un-masked silicon using OXFORD Plasma 80 Plus RIE system. As it can be seen in Fig. 3.3, the patterned metal-film acts as mask for realizing rib structure. Here, it is necessary to have anisotropic etching of silicon with better selectivity over the metal mask. The etching chemistry optimized earlier is used for the present work [58, 59]. In this process, the sample is initially loaded into the chamber which is evacuated to obtain a base pressure of  $3 \times 10^{-7}$  mTorr. Then a mixture of  $\text{SF}_6$  and Ar is passed, each at a flow rate of 20 sccm to achieve a constant chamber pressure of 200 mTorr. The oscillating electric field (RF freq: 13.56 MHz, RF power: 150 W) applied across the two electrodes inside the chamber, ionizes the gas (Ar) by stripping the electron and thereby creating plasma which eventually disintegrates  $\text{SF}_6$  that etches silicon and releases  $\text{SiF}_4$ . The chemical reaction representing the same are shown below [79]:



Initially, for the mentioned recipe various chamber pressure were tried in order to find the etch rate. It was found that higher chamber pressure ( $\geq 250$  mT) is responsible for more of chemical etching due to presence of higher amount of reacting species and thus showing higher etch rate. While in case of lower chamber pressure, etching mostly happens due to physical removal of silicon by energized positive ions and the



etching rate was found to be relatively lower. The etch-rate for a chamber pressure of 100 mTorr was estimated to be  $\sim 0.16 \mu\text{m}/\text{min}$  while for a chamber pressure of 250 mTorr it is  $\sim 0.38 \mu\text{m}/\text{min}$ . However, etching at higher chamber pressure is less preferred as the etching is isotropic in nature resulting in under-cut and all around feature shrinking ( $\leq 1 \mu\text{m}$  on each edge). Furthermore, physical etching at lower pressure tends to increase the surface roughness of the sample and hence an intermediate value of chamber pressure (200 mTorr) was selected as a compromise. Samples etched with the mentioned recipe ( $\text{SF}_6$ : Ar:: 20:20 sccm, 200 mTorr, RF Power: 150 W) showed a surface roughness of  $\sim 40 \text{ nm}$  when measured using surface profiler (WYKO, Veeco Metrology Corporation).

As mentioned earlier, the RIE is carried out using patterned metal thin-film acting as a mask over the sample surface, which is removed from top of the rib structure after completion of etching process. The PPR mask is less preferred during RIE process as uneven edges are often observed (see Fig. 3.4(a)). These uneven edges could be because of the lower selectivity of the etchant species over the PPR mask ( $\sim 10 : 1$ ) as compared to the metal mask ( $> 30 : 1$ ). Microscopic images of waveguides fabricated with PPR and metal mask are shown in Fig. 3.4 for comparison. Similar non-uniform waveguide edges are also observed while using KOH based developer solution. Typical

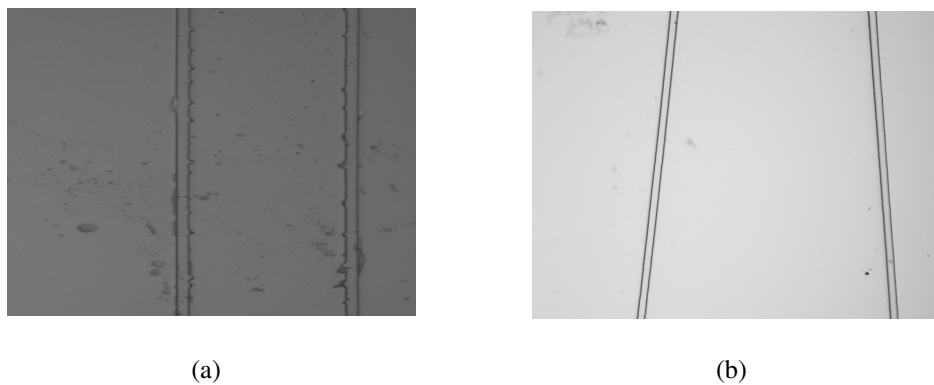


Figure 3.4: Waveguide fabricated using (a) PPR mask and, (b) Metal mask.

SEM images of different sections of interleaver fabricated using metal mask along with optimized process parameters discussed earlier are shown in Fig. 3.5.

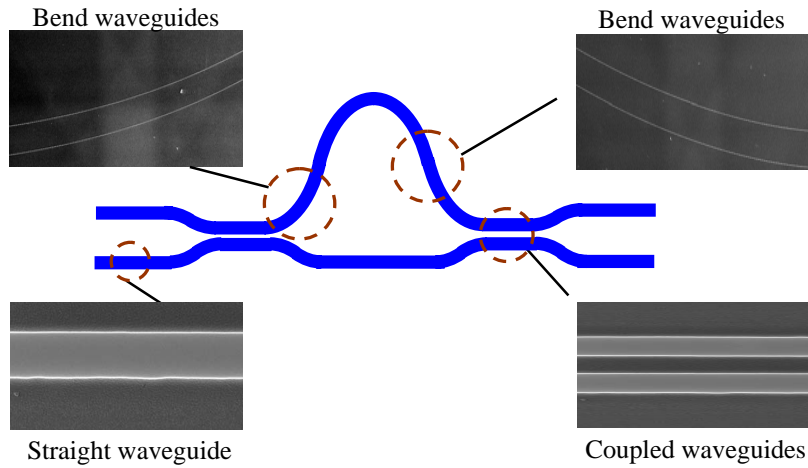


Figure 3.5: Typical SEM images of different sections of a fabricated interleaver.

**(v) Photolithography for Polarizer Definition**

For realizing an on-chip TE-pass waveguide polarizer, metal masks used for waveguide definitions are selectively retained by another photolithographic definition (also see Fig. 3.2). The microscopic image of a TE-pass waveguide polarizer is shown in Fig. 3.6. The patterned metal is then etched using suitable metal etchant (Appendix A.2). Three different metal-coated waveguide polarizers have been investigated using three different metals namely Al, Cr and Au. Samples are fabricated with Al, Cr and Au as the top cladding with thickness  $\sim 100$  nm,  $\sim 100$  nm, and  $\sim 40$  nm, respectively. The thinner gold cladding was chosen due to Au-Si adhesion issues. Initially, metal-coated

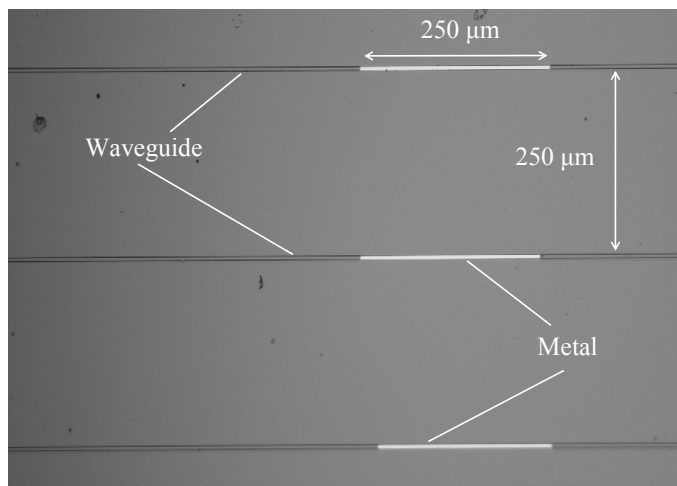


Figure 3.6: Typical microscopic image of a metal coated silicon rib waveguides.

Table 3.1: List of fabricated samples with integrated waveguide polarizer.  $S_i$ :  $n$  - where  $i=1,2,3,4,5,6$  are the set number and,  $n$  is the number of uniform waveguides in the corresponding set (see text for set description). Also mentioned are the cladding metal on each sample. Waveguides on all the samples have an etch depth of  $\sim 1.2 \mu\text{m}$ .

Sample Number	Device Sets: Uniform Waveguides	Cladding Metal	Remarks
GS3	S2: 1, S3: 3, S4: 4, S5: 3	Cr	Device length was $\sim 1.2$ cm. Other waveguides of sets S1, S2, S3 and, S5 were damaged due to cuts in top metal-film before RIE. Good Cr-coated polarizer sample.
GS10	S3: 1, S4: 4, S5: 4, S6: 3	Cr	Device length was $\sim 1.2$ cm. Other waveguides of sets S2, S3 and, S6 were damaged due to cuts in top metal-film before RIE. Good Cr-coated polarizer sample.
GS1	S1: 3, S2: 5, S3: 5, S4: 6	Al	Devices are fabricated using old waveguide mask with 7 waveguides per set. Sample length was $\sim 1.5$ cm. Other waveguides of sets S1, S2, S3 and, S4 were damaged due to cuts in top metal-film before RIE. Good al-coated polarizer sample.
GS5	S1: 3, S2: 4, S3: 4, S4: 4, S5: 4	Al	Device length was $\sim 0.8$ cm. Other waveguides of sets S1 were damaged during handing mainly due to their proximity to sample edge. Good Al-coated polarizer sample.
GS8	S1: 4, S2: 4, S3: 4, S4: 4, S5: 4, S6: 4	Au	Device length was $\sim 1.2$ cm. Good Au-coated polarizer sample.
GS9	S1: 4, S2: 4, S3: 4, S4: 4, S5: 4, S6: 4	Au	Device length was $\sim 1.2$ cm. Good Au-coated polarizer sample.

straight waveguides are fabricated and characterised for polarization dependent losses before integrating with the interleaver. Table 3.1 shows a list of metal-coated waveguide samples which have been investigated. These samples contained five sets of four identical straight waveguides with  $W = 5 \mu\text{m}$ . These five sets S1, S2, S3, S4, S5, and S6 had metal-cladding of lengths  $200 \mu\text{m}$ ,  $400 \mu\text{m}$ ,  $600 \mu\text{m}$ ,  $800 \mu\text{m}$ ,  $1000 \mu\text{m}$ , and  $1200 \mu\text{m}$ , respectively (also see Section 3.1). The metal-clad waveguides were initially studied for an etch-depth of  $\sim 1.2 \mu\text{m}$ . Magnified microscopic images of metal coated

rib waveguides are shown in Fig. 3.7. The poor quality of metal-film in Fig. 3.7(b), can be due to strong affinity of developer solution (NaOH) to Aluminium.

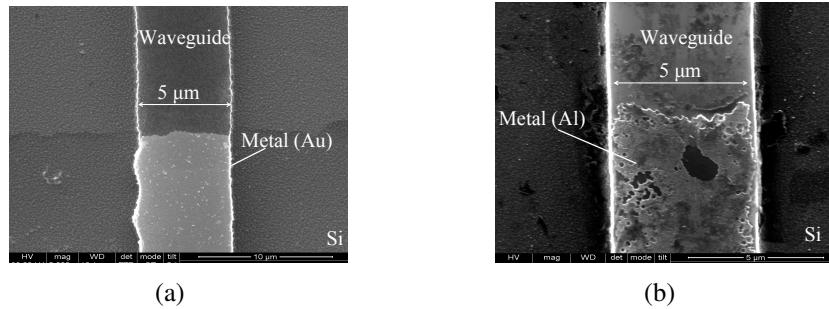


Figure 3.7: (a) SEM image of silicon rib waveguides coated with e-beam deposited Au. (b) SEM image of silicon rib waveguides coated with thermally deposited Al.

#### (vi) End-facet Preparation

The end facet of the fabricated samples have to polished so as to allow effective coupling of light into the waveguides. The samples are mechanically polished using ULTRAPOL, Ultra-Tec Inc., USA. The end facet of the sample were initially polished using abrasive (diamond coated) films with particle size  $30 \mu\text{m}$ . Subsequently, the abrasive films with smaller particle size were used and finally the end facet roughness of  $\sim 0.5 \mu\text{m}$  was achieved. The Fig. 3.8 shows the polished end-facets of two adjacent rib waveguides of interleaver with a separation of  $250 \mu\text{m}$ .

#### Summary of Fabricated Devices

A list of fabricated samples is shown in Table 3.2. The measured etch-depth after RIE on each of these samples is separately mentioned in column 2. The etching time (or etch-depth) during RIE was slightly adjusted after thorough microscopic examination of waveguide spacings in the coupler region (also see Section 2.3). Devices which were observed to be marginally over-developed, the etching depth was accordingly reduced and vice-versa. As mentioned earlier in Section 3.1, each of the mask layout contained five sets of six waveguides each. A list of uniform waveguides in each set of fabricated samples is also given Table 3.2. Sample GI7 and GI15 (also see Table 3.2) were initially

Table 3.2: List of fabricated interleaver samples. Each if samples are designated a particular number. The etch-depth and working waveguides in each set ( $S_i[n]$ ) are shown. Also see Fig. 3.1 for reference.

Sample Number	Etch Depth [ $\mu\text{m}$ ]	Device Sets: Uniform Waveguides	Remarks
GI1	$\sim 1.65$	-	All the devices showed pillar like structures parallel to the waveguides after RIE. None of the devices on the sample showed output response during optical characterization.
GI2	$\sim 1.65$	-	Sample was damaged during polishing.
GI12	$\sim 1.7$	S2: Wg1-Wg4 S3: Wg1-Wg6 S4: Wg4-Wg6 S5: Wg1	Reference directional coupler in S2 showed a near 3-dB power splitting. Interleaver in set S2 showed good characteristics and was pigtailed using single-mode fibers.
GI13	$\sim 1.7$	S2: Wg1-Wg6 S3: Wg1-Wg6 S4: Wg1-Wg3 S4: Wg5-Wg6	Reference directional coupler in set S2 showed a near 3-dB power splitting.
GI7	$\sim 1.75$	S2: Wg1-Wg6 S3: Wg1-Wg6 S4: Wg1-Wg5 S5: Wg1-Wg6	Reference directional coupler in set set S4 showed nearly 3-dB power splitting. Devices in set S4 were later integrated with waveguide polarizer (Al, length $\sim 1$ mm).
GI14	$\sim 1.75$	S3: Wg1-Wg6 S5: Wg1-Wg5	Reference directional couplers in set S3 showed nearly 3-dB power splitting. Interleaver in set S3 showed good characteristics and was pigtailed using polarization maintaining fibers.
GI15	$\sim 1.75$	S3: Wg2-Wg6 S4: Wg1-Wg6 S5: Wg1-Wg4	Sample surface showed a roughness of $> 60$ nm. Relatively poor power levels were measured at the output during the characterizations. Devices in set S4 were later integrated with waveguide polarizer (Al, length $\sim 1$ mm).
GI10	$\sim 1.8$	S3: Wg2-Wg5	A milky white patch covering S4 and S5 was seen over the sample surface after RIE. Surface study of sample revealed high roughness ( $> 100$ nm). Precise reason for the problem could not be found. The set S3 during optical characterization showed poor power levels.

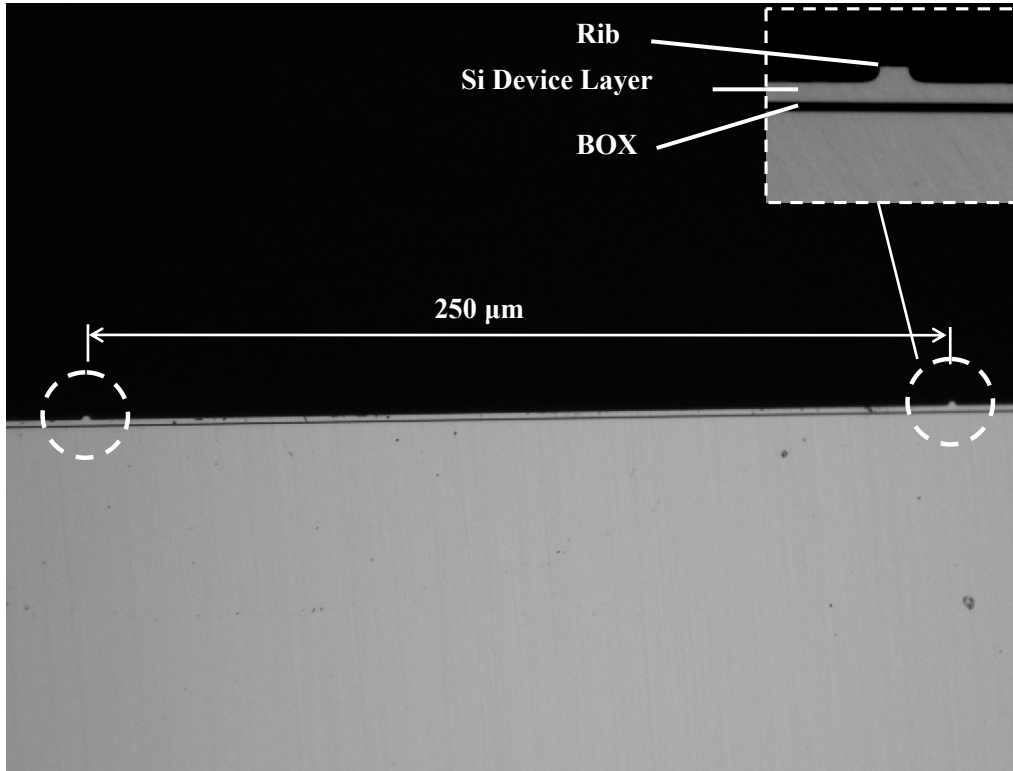


Figure 3.8: Polished end-facet of SOI based interleaver showing two ribs 250  $\mu\text{m}$  apart. Inset: Cross section close-up of a rib structure in SOI.

fabricated with Cr mask and after thorough optical characterization, integration of Al-clad waveguides was carried out. The devices were re-coated with Al and then patterned using second mask. Some of the devices samples were damaged due to various issues in fabrication process like over-developing, discontinuous waveguides after RIE due to cuts in top metal thin-film, edge damage and sample breaking during dicing/polishing, high surface roughness after RIE due to previous process residue, etc.

### 3.3 Device Characterizations

The fabricated samples were characterized in terms of insertion loss, wavelength and polarization dependencies, inter-channel and polarization extinctions. A block diagram of the experimental setup has been shown in Fig. 3.9. An external cavity tunable semiconductor laser source ( $1520 \text{ nm} < \lambda < 1600 \text{ nm}$ ) with a line width of  $\sim 0.8 \text{ pm}$  and minimum tuning step of  $1 \text{ pm}$  is used to characterize the fabricated devices. The light output from the source is taken through a polarization controller using a single mode

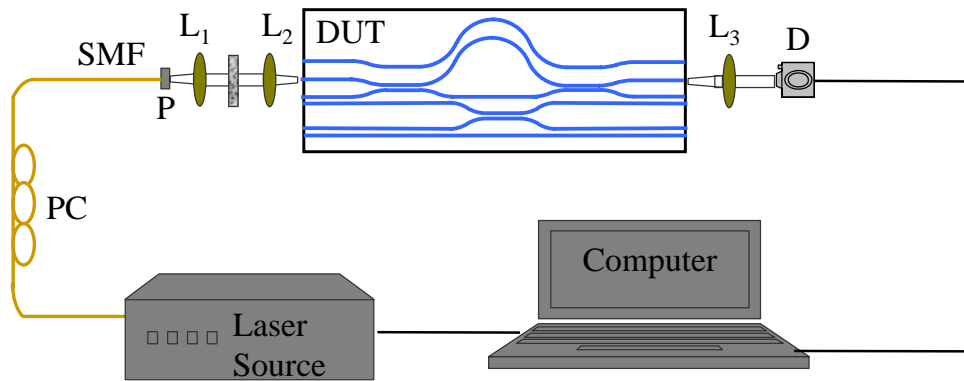


Figure 3.9: Schematic of the experimental setup used for characterization of integrated optical interleaver. PC-Polarization Controller, SMF-single mode fiber, L-Lens, P-Polarizer, DUT-Device Under Test, D-Detector (IR Camera/PIN detector).

fiber. The polarization controller induces stress on the single mode fiber due to which the power can be varied among the two orthogonal polarizations. The light beam is then collimated using a lens setup and allowed to pass through a Glan-Thompson polarizer. This basically contains two calcite prism stacked together along their long faces. The optical axes of calcite crystals are parallel and aligned perpendicular to the plane of reflection. Due to birefringence the incoming light beam splits into two rays (ordinary & extraordinary), both experiencing different refractive indices. Since the ordinary and extraordinary refractive indices are different, the EM wave along extraordinary axis will be deviated away from the principle axis (according to Snell's law) when it exits from the crystal. This will result in two separate images, of ordinary and extraordinary wave. The polarization controller can now be tuned such that power in the ordinary wave can be maximized and thus allowing only one orthogonal polarization to pass through. The waveguides are tested for polarization dependencies by maximizing power in one of the two polarization (TE or TM) using polarization controller and an external polarizer. The polarized light beam is then focused on the polished end facet of the rib waveguide. The transmitted light from the device is collected using another lens and focused on the detector/IR camera for measuring the power/intensity profiles. Alternately, we can also use another Glan-Thompson polarizer (analyzer) on the output side to measure the polarization extinctions in the transmitted light. The data-logging from detector/IR camera and wavelength tuning at the laser source are synchronized using a virtual in-

terface in LABVIEW on host computer. At first, characterization results of straight and bend waveguides and directional couplers will be presented. Later, characterization results of fabricated interleaver devices are shown.

### Single-mode Waveguides

The single-mode straight waveguides fabricated along side interleaver were studied for waveguide loss and polarization dependency. These waveguides were 3 cm long with  $W = 5 \mu\text{m}$  and  $h = 3.2 \mu\text{m}$ . The captured intensity profiles for TE and TM polarization captured using a near field IR camera (specification) are shown in Fig. 3.10. The measured  $(1/e^2)$  mode size for TE (TM) polarization is found to be  $\sim 4.6 \mu\text{m} \times 6.3 \mu\text{m}$  ( $\sim 4.2 \mu\text{m} \times 5.2 \mu\text{m}$ ), closely matching with the theoretical values of  $\sim 4.2 \mu\text{m} \times 6.2 \mu\text{m}$  ( $\sim 3.8 \mu\text{m} \times 5.6 \mu\text{m}$ ), respectively. The variation in the experimentally measured mode dimension for TE and TM polarization is due to slight waveguide birefringence. While estimating the measured mode-size, the measured intensity profiles were compared to a known intensity distribution of a single-mode fiber. Thus, measurement errors were avoided.

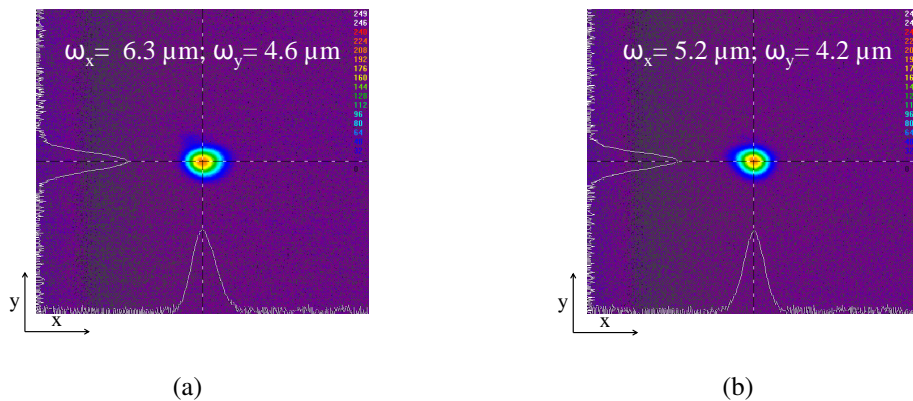


Figure 3.10: Captured intensity profiles for TE (a), and TM (b) polarizations, respectively.  $\omega_x$  is the mode spread in horizontal direction and  $\omega_y$  is the mode spread in vertical direction. Results correspond to sample S4 of GI14.

The waveguide loss measurement was carried out using low-finesse loss measurement technique [80]. Waveguide structure can be compared to that of a cavity where the optical signal propagating along the waveguide experiences multiple reflections at the two end-facets depending on the refractive index of waveguide core and external



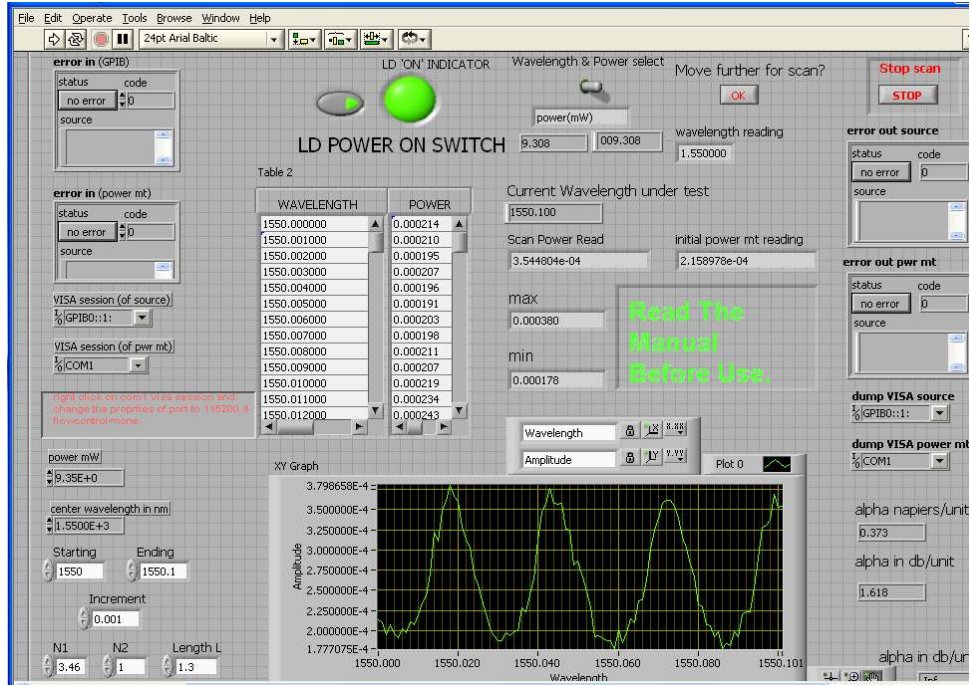


Figure 3.11: Screen-shot of virtual interface developed on LABVIEW for waveguide loss measurement.

medium [8]. This leads to interference of light at the waveguide output facet and a sinusoidally varying response is observed as a function of wavelength. The FSR of the cavity is given by  $\Delta\nu = \frac{c}{2n_{eff}L}$ , where  $L$  is the length of cavity (or waveguide in our case) and  $n_{eff}$  is the effective refractive index. Fig. 3.11 shows the screen-shot of a LABVIEW based virtual interface developed for loss measurement, while Fig. 3.12 shows a Fabry-Perot resonance recorded at the output side of a waveguide when scanned over a small wavelength range near  $\lambda = 1550$  nm. The slight distortion in the characteristics shown in Fig. 3.12 is due to error in experimental measurement as the wavelength tuning steps are limited here to  $\sim 1$  pm. The experimental results are recorded from a reference straight waveguide (S3-GI14) of length  $\sim 3.1$  cm. The experimental FSR  $\sim 9$  pm closely matches our theoretical calculations ( $\sim 11$  pm). As a comparison, a Fabry-Perot resonance of another sample  $\sim 1.5$  cm long is shown with an estimated of FSR  $\sim 25$  pm (theoretical FSR: 27 pm). The loss from the above plot can then be derived using Eq. 3.1 [8, 42].

$$\alpha = \frac{1}{L} \ln \left( \frac{1 + \sqrt{\zeta}}{R \sqrt{\zeta} + 1} \right) \quad (3.1)$$

where,  $\alpha$  is the loss,  $\zeta = \frac{I_{max}}{I_{min}}$ ,  $L$  is the sample length and  $R$  is reflectivity at the

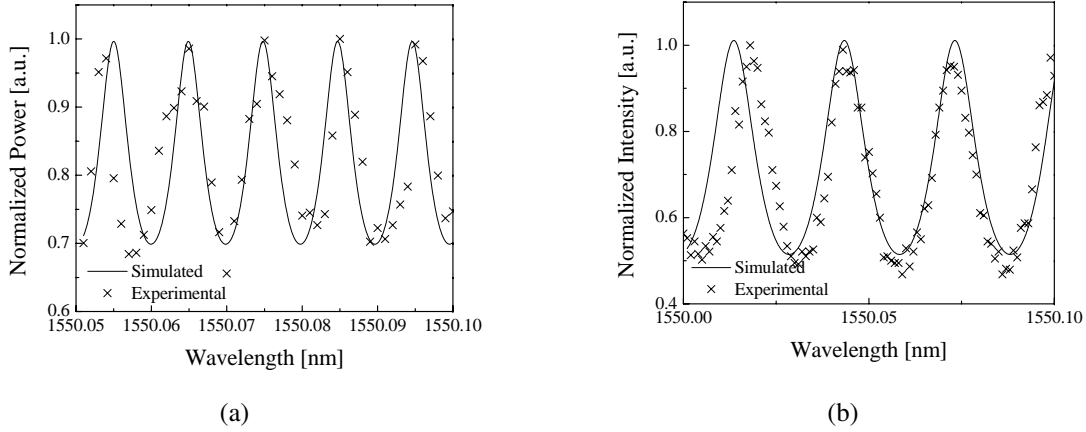


Figure 3.12: Fabry-perot resonance recorded from a straight waveguide of length (a)  $\sim 3.1$  cm and, (b)  $\sim 1.5$  cm. Laser tuning step 1 pm. Solid line is an empirical fit while the scatter points are the actual data points. Results recorded from GI14 and GS1, respectively.

end-facet. The values of  $I_{max}$  and  $I_{min}$ , the maximum and minimum values of the intensities respectively, can be obtained from the Fig. 3.12 and reflectivity is given by  $R = \left( \frac{n_{eff}-1}{n_{eff}+1} \right)^2$ . Where  $n_{eff}$  is the effective index of the guided mode. The best of the measured waveguide loss for TE (TM) polarization using the above equation is 1.2 dB/cm (0.8 dB/cm). This waveguide loss accounts for material absorption characteristics and scattering loss due waveguide side-wall roughness. The waveguide losses are higher in case of TE polarized light as the dominant electric field component normal to the rib side wall experiences higher scattering. It is worth to mention here that these losses were found to be uniform across the entire optical communication band (C, L).

The 3 cm-long meander bends replicating the top arm of the interleaver were also characterized for its wavelength and polarization dependent performance. These meander bend structures showed an overall wavelength independent insertion loss of  $\sim 9$  dB. These structures contain four s-bend structures of 15 mm bending radius (see Fig. 2.7). Deducting the measured waveguide loss for such a  $\sim 3$  cm long straight waveguide, a total bend induced loss of  $\sim 6$  dB (for 4 s-bends) is estimated.

### Directional Couplers

The  $2 \times 2$  reference directional couplers adjacent to the interleaver were characterized for insertion loss, polarization dependency and wavelength dependency. Intensity profiles

captured at two output ports indicates uniform power splitting of directional couplers (see Fig. 3.13). The splitting of the directional coupler was then recorded over the entire  $\lambda = 1520 \text{ nm}$  to  $1600 \text{ nm}$  band using a LABVIEW based virtual interface, similar to the one shown in Fig. 3.11. As expected from our theoretical predictions, directional couplers showed a polarization dependent but uniform power splitting across the entire C+L band (see Fig. 3.14) [81]. This polarization dependency is due to the polarization

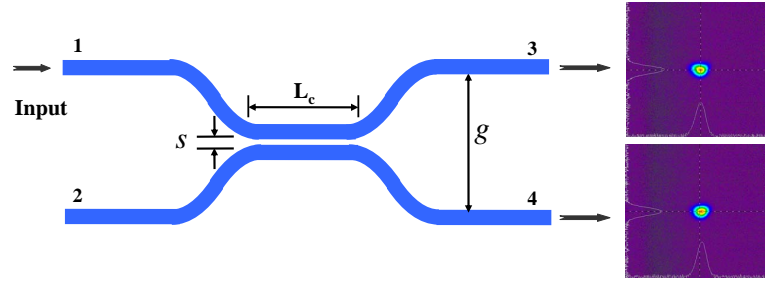


Figure 3.13: Captured intensity profiles at the two output ports of directional coupler showing uniform power splitting at bar (Port 3) and cross (Port 4) port. The profiles are recorded at  $\lambda = 1550 \text{ nm}$  for TE polarization from directional coupler in set S4 of GI7.

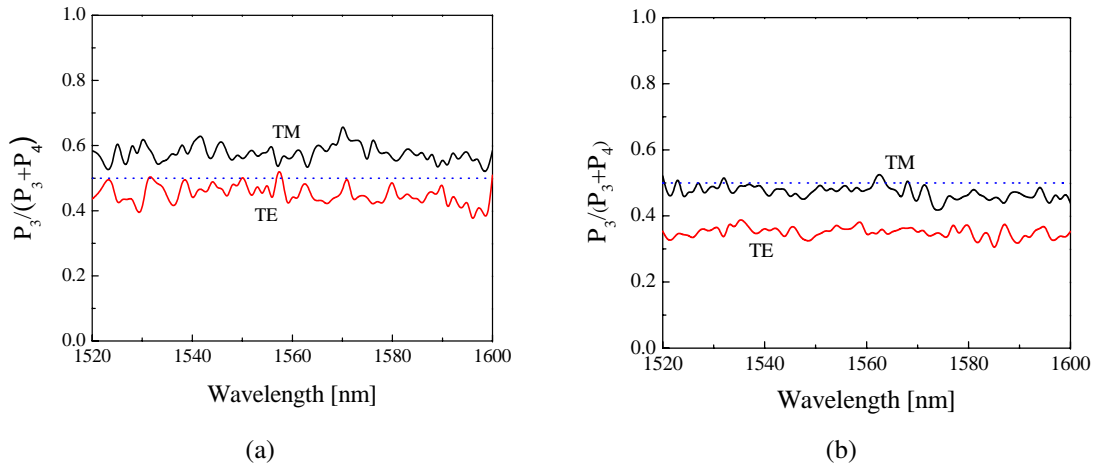


Figure 3.14: Wavelength dependent power splitting ratio of directional coupler with (a)  $L_c = 1400 \mu\text{m}$  and  $r = 0.64$  and (b)  $L_c = 1200 \mu\text{m}$  and  $r = 0.66$ . Note the difference in splitting ratio for two polarizations. These results are recorded from directional coupler in set S4 of GI7 and set S2 of GI12, respectively.

dependent mode-size and effective refractive indices of the guided fundamental modes. The overall on-chip insertion loss of the directional couplers was estimated to be  $\sim 6 \text{ dB}$  for the two polarizations. This includes waveguide losses, total bending losses and, insertion loss of coupler.

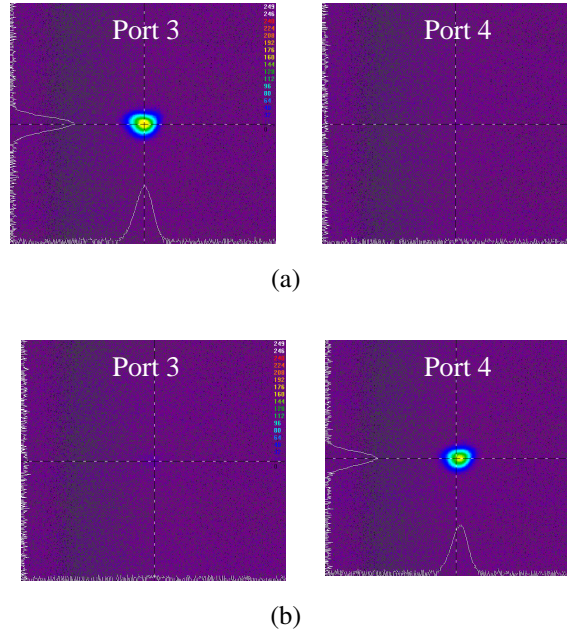


Figure 3.15: Transmitted intensity profiles measured at bar and cross ports for two consecutive ITU channels: (a)  $\lambda = 1550.9$  nm and (b)  $\lambda = 1551.7$  nm for TE polarization, respectively.

### Interleaver

The transmitted mode profiles at the two out ports were captured using IR-camera in the near field. Fig. 3.15 shows the transmitted profiles for TE polarizations for two consecutive ITU channels with 100 GHz channel spacing [82]. It is clearly evident that when one of the channel retains power in a particular port, the same channel in other port is completely diminished. The interleavers were characterized for wavelength dependency across the entire optical C+L band. Fig. 3.16 shows the device response over entire optical C band recorded using a virtual interface on LABVIEW. Uniformity of the response in terms of inter-channel extinction and insertion loss at the channel peak is clearly evident. It is worth to mention here that the two directional couplers in this particular structure response shown here were having a coupling length of  $1400 \mu\text{m}$ .

The poor inter-channel extinction in Fig. 3.16 is due to resolution error caused by high wavelength tuning step. For better visualization wavelength characteristics taken over a smaller range ( $\lambda = 1550$  to  $1555$  nm) with a fine tuning step ( $\sim 30$  pm) for both the polarization are shown in Fig. 3.17 [81]. The little variation in the inter-channel extinction at two ports is due to slight non-uniformity in power splitting of the directional coupler. Here, the inter-channel extinction is obtained best in case of TE

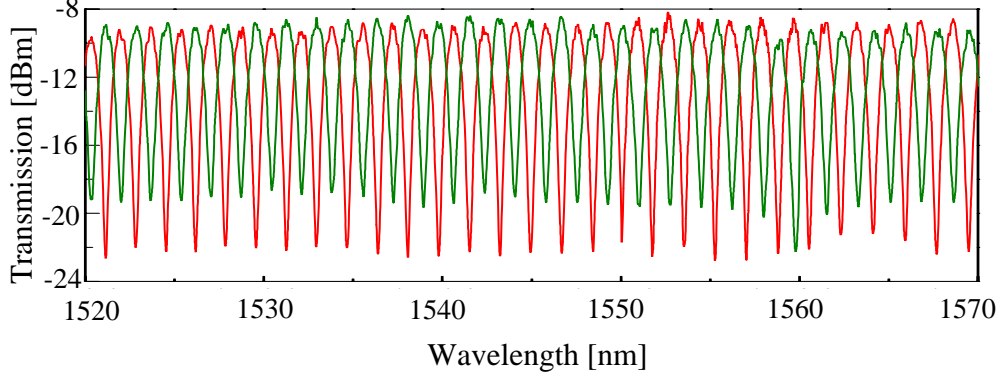


Figure 3.16: Experimentally measured transmission characteristics for TE polarization over entire optical C band. The experimentally measured value of channel spacing  $\Delta\lambda = 0.84$  nm and inter-channel extinction  $\delta_{ex\_ch} \sim 10$  dB. Lines in red correspond to response at Port 3 (Bar) and, lines in green correspond to response at Port 4 (cross). Laser wavelength tuning steps=50 pm. Results correspond to sample S4 of G17.

polarization due to nearly 3-dB power splitting of its directional coupler (also see Fig. 3.14(a)). Fig. 3.18 shows a response of another interleaver device having directional couplers with non-uniform power splitting (also see Fig. 3.14(b)). Moreover, shift in channel resonance peaks ( $\sim 0.25$  nm) for TE and TM polarization was also observed. As discussed in theoretical analysis, this shift is due to slight waveguide birefringence (see Section 2.4). It is worth to mention here that, this variation in effective indices for two polarizations did not affect the interleaved channel spacings at the output. The resonance peaks for consecutive channels at the output were separated by  $\sim 105$  GHz in contrast to the designed value of 100 GHz. This variation is due design error in  $\Delta L$  ( $\sim 0.1\%$ ) because of the angular rounding introduced by the mask designing CAD tool. Some of the best interleaver showed an inter-channel extinction of  $> 12$  dB and  $> 13$  dB at bar and -cross ports, respectively. The low inter-channel extinction from the predicted theoretical value can be attributed to the polarization dependencies of the LCRW structures. As mentioned previously, our characterization setup involves use of external Glan-Thompson polarizer ( $\delta_{ex-pol} \sim 15$  dB) for ensuring that the launched light signal is of a particular polarization. This low polarization extinction during device characterization can be one of the reason for low inter-channel extinction measured from interleaver.

The interleavers were also characterized for insertion loss. The overall on-chip in-

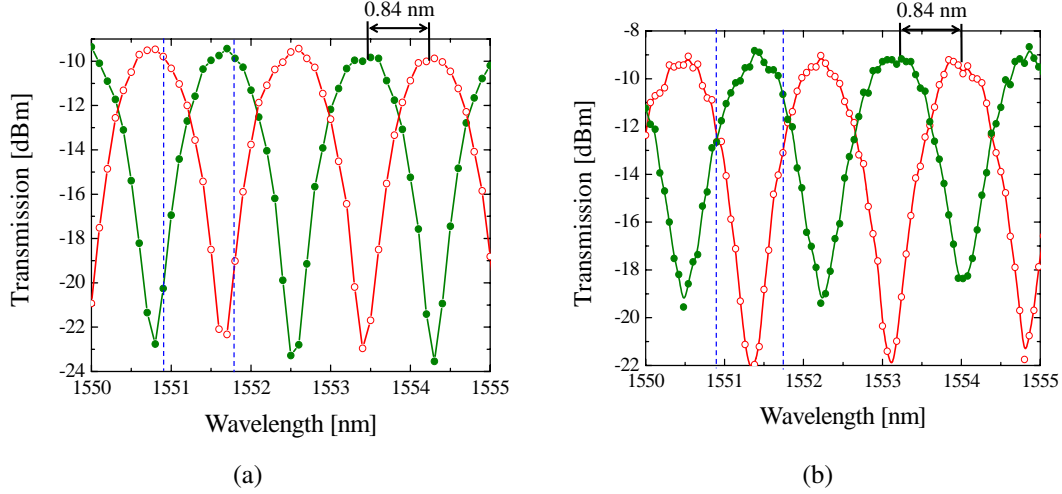


Figure 3.17: Experimentally measured transmission characteristics for TE (a) and, TM (b) polarizations, respectively. Lines in red correspond to response at Port 3 (Bar) and, lines in green correspond to response at Port 4 (cross). Note the shift in resonance peaks. Results correspond to interleaver in set S4 of GI7.

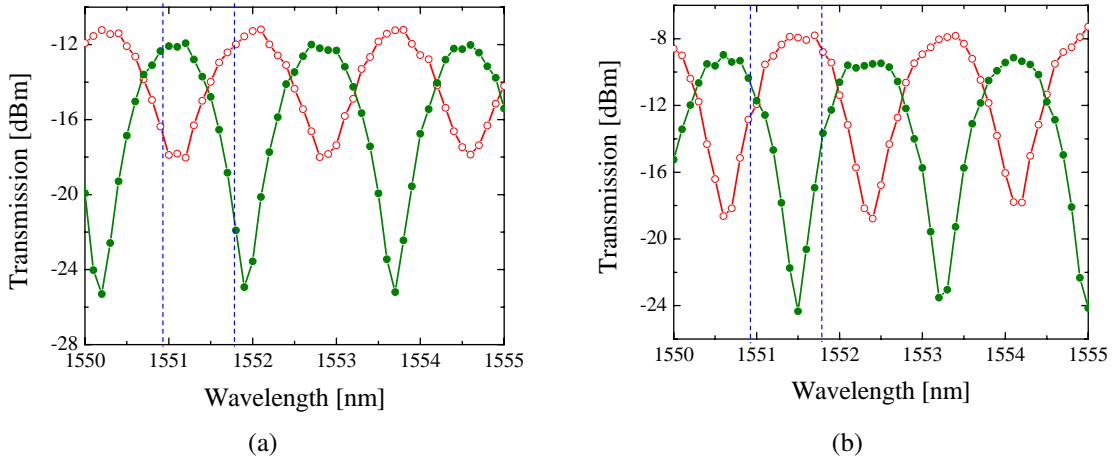




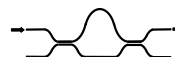
Figure 3.18: Experimentally measured transmission characteristics for TE (a) and, TM (b) polarizations, respectively. The reference directional couplers show non-uniform power splitting ( $L_c = 1200 \mu\text{m}$  and  $r = 0.66$ ). Lines in red correspond to response at Port 3 (Bar) and, lines in green correspond to response at Port 4 (cross). Note the shift in resonance peaks. Results shown here are from interleaver in set S3 of GI12.

sersion loss of  $\sim 11$  dB was measured at the channel pass band. This high insertion loss accounts for waveguide losses ( $\sim 1$  dB/cm), bend induced losses ( $\sim 6$  dB) and insertion loss of two directional couplers ( $\sim 2$  dB). These high losses are directly or indirectly related to the waveguide sidewall roughness and can be significantly reduced ( $< 0.5$  dB/cm) by use of ICP-RIE technique during the fabrication of SOI based waveguide device.

## Polarization Issues and Metal Clad Waveguides

As shown in the above characterization results, LCRW based structures are found to be slightly polarization dependent. The structural birefringence results in interleaver response with shifted resonance peaks for two different polarizations. The directional couplers showed different power splitting due to polarization dependent mode-field distribution. Thus, it is necessary to operate LCRW based devices in either of the two polarization at a time. However, it has also been found that there is significant amount of polarization cross-talk in LCRW based bend waveguides. This has been discussed and shown schematically in Fig 2.7. Each of the above discussed structures were characterized for polarization cross-talk/rotation by measuring input and output polarization extinctions. Table 3.3 and 3.4 shows the measured polarization extinction values at output, for an input signals of TE and TM polarization, respectively [83]. Here, the polar-


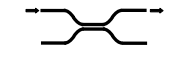
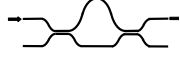
Table 3.3: Measured polarization extinction ( $\delta_{ex}$ ) for LCRW based meander-bend, directional coupler and interleaver. Input signal if of TE polarization. This particular data is recorded from sample GI7.

Device	Layout	Operating Wavelength	TE-to-TM	
			Input $\delta_{ex}$	Output $\delta_{ex}$
Meander Bend		1550 nm	-18 dB	-15.8 dB
Directional Coupler		1550 nm	-18 dB	-16.4 dB
Interleaver		1549.2 nm	-18 dB	-15 dB

ization extinction  $\delta_{ex}$  is given according to Eq. 2.9. The tabulated results were recoded from sample GI7. Similar response was recoded from waveguide devices on samples GI17 and, GI18. Degradation in polarization extinction observed above can be partly due to polarization dependent losses ( $\Delta\alpha = \alpha_{TM} - \alpha_{TE} \sim 0.2$  dB/cm) [84], polarization dependent power splitting ( $\sim 0.7$  dB), and polarization rotation. The polarization rotation was estimated to be higher from TE-to-TM than TM-to-TE. This could be due to the particular orientation of electric field components for TE and TM polarizations (see Fig. 2.7). The dominant electric field component in case of TE polarization is



Table 3.4: Measured polarization extinction ( $\delta_{ex}$ ) for LCRW based meander-bend, directional coupler and interleaver. Input signal is of TM polarization. This particular data is recorded from sample GI7.

Device	Layout	Operating Wavelength	TM-to-TE	
			Input $\delta_{ex}$	Output $\delta_{ex}$
Meander Bend		1550 nm	18 dB	16.7 dB
Directional Coupler		1550 nm	18 dB	16.3 dB
Interleaver		1549.2 nm	18 dB	17.1 dB

$E_x$  which prominently observes the refractive index asymmetry due to curvature of rib (also in x-z-plane). However, this interaction is weak for TM mode consisting of dominant  $E_y$  component. The polarization rotation is expected to be more dominantly in case of bends with shorter bending radius [85] as well for nano-dimension PhW waveguides [71]. This can considerably degrade the device performance. In order to solve these issue, integrated TE-pass polarizers with metal clad waveguides are fabricated and improvement in polarization extinction is subsequently measured.

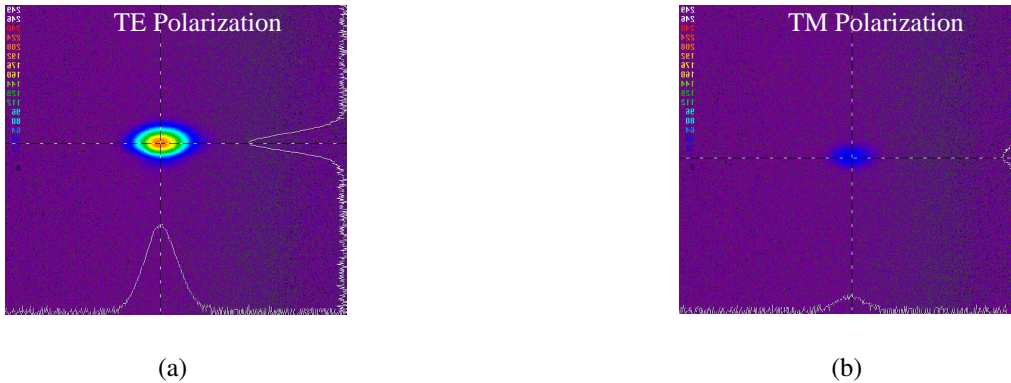


Figure 3.19: Transmitted intensity profiles from metal clad rib waveguides for (a) TE polarization and, (b) TM polarization. Metal: Al,  $l \sim 1$  mm,  $t_{Al} \sim 100$  nm. The results are recorded from sample GS5.

Input light is launched into these sample by aligning the Glan-Thompson polarizer on the input side at  $45^\circ$ . At the output side another polarizer is used to measure the transmitted TE and TM polarized light intensity. Fig. 3.19 shows the captured intensity



profiles for guided TE and TM polarized light from an aluminium coated rib waveguide of length  $\sim 1$  mm [83]. As expected, the TM polarized light is almost attenuated

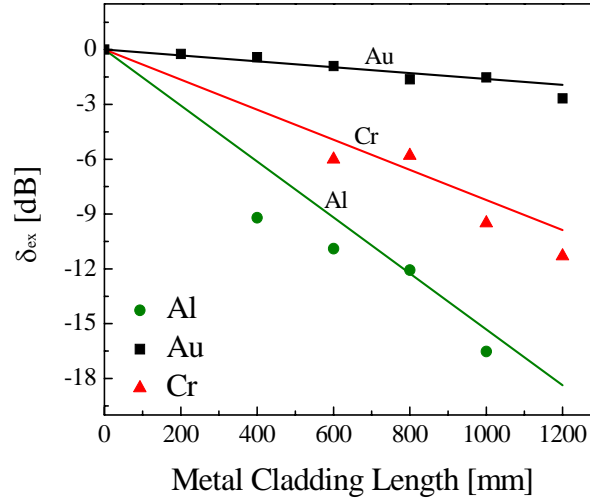


Figure 3.20: Measured polarization extinction as a function of metal cladding length shown by scatter points for two different metals Al and Au. Here, the Al and Cr cladding thickness is  $\sim 100$  nm, while Au cladding thickness is 40 nm. Solid lines denote the empirical solution from the BPM simulations. Results for different metal shown here are average values from samples mentioned in Table 3.1.

while the TE polarized light remains nearly unaffected. The polarization extinction ( $\delta_{ex}$ ) as a function of metal clad waveguide length is shown in Fig. 3.20 [83]. Solid lines are the empirical fit obtained using BPM simulation data while the scatter points are experimentally measured values. Typically, polarization extinction of  $> 20$  dB (industry benchmark) can be obtained by having Al metal cladding of length  $> 2$  mm. It is worth to mention here that Cr metal clad waveguide showed considerably high TE loss. This can be due to  $\text{Re}(n_{Cr}) > \text{Re}(n_{Si})$ . The above mentioned TE-pass polarizer was successfully integrated with interleaver and tested for its optimum performance. It was found that the interleaver samples with etch-depth  $\sim 1.75 \mu\text{m}$  showed a similar polarization extinction characteristics as those with initial straight waveguide samples with etch depth  $\sim 1.2 \mu\text{m}$ . However, it is observed that integrated such a polarizer increased the insertion loss by  $\sim 2$  dB.

## 3.4 Conclusions

A dispersion-free DWDM channel interleaver has been successfully fabricated in SOI platform with large cross-section single-mode rib waveguide structures. The characterized device samples showed an interchannel extinction of  $> 12$  dB at bar and cross ports with an interleaved channel spacing of 210 GHz. This variation is due to the design error in  $\Delta L$  ( $\sim 0.1\%$ ) because of the angular rounding introduced by the mask designing CAD tool. The device samples are found to be polarization sensitive. Moreover, the reference meander bend waveguides showed a polarization rotation causing the polarization extinction to degrade by  $\sim 3$  dB. As a solution to this problem, an integrated optical TE-pass polarizer has been fabricated with metal-clad waveguides (Al, length:  $\sim 1$  mm, thickness:  $\sim 100$  nm) and a polarization extinction of  $> 15$  dB is recorded. However, it has been found that integrating such polarizer can further increase the insertion loss of the device (by  $\sim 2$  dB).

# CHAPTER 4

## Device Packaging and Testing

In the previous chapter, fabrication and characterization results of DWDM channel interleaver were presented. Some fabricated devices were fiber pigtailed, packaged and tested for their performance. The details of fiber pigtailling and packaging procedure have been discussed in Section 4.1. Afterwards, the test results of a packaged prototype device have been presented in Section 4.2. Finally, a brief conclusion is made at the end of the chapter.

### 4.1 Fiber Pigtailling

The fiber pigtailling and packaging of some of the SOI interleaver chips have been carried out with the help of Dr. Anuj Bhatnagar and his team at SAMEER, Mumbai. As noticed in the previous chapter, the fabricated devices are slightly polarization sensitive and thus it is necessary to operate in one of the two polarizations (TE or TM). Therefore, the devices were pigtailed using commercially acquired PM fiber v-groove assemblies. A typical cross section of one such fiber v-groove assembly is shown in Fig. 4.1(a). Each of these fibers have a diameter of  $\sim 125 \mu\text{m}$  and are placed in a silicon v-groove assembly with a center-to-center separation of  $\sim 250 \mu\text{m}$ . The assembly is tightly held by gluing it with a pyrex lid from top. The end-facet of fiber-v-groove assembly are polished for efficient butt-coupling of light to the polished waveguide end-facets. Since, the v-groove thickness is  $\sim 1 \text{ mm}$ , it is recommended to have an equivalent handle wafer thickness of integrated optical chip, in order to achieve better mechanical support during adhesion. As mentioned earlier, the interleavers are fabricated in commercially acquired optical grade SOI wafers having a handle wafer thickness of  $\sim 500 \mu\text{m}$  (see Fig. 4.1(b)). Hence, these wafers are at first glued to another dummy substrate (silicon wafer thickness  $\sim 500 \mu\text{m}$ ) using an epoxy adhesive (Araldite). Typically, such epoxy adhesive have a tendency to harden as soon as their polymer-resin and hardner are mixed together. In order to achieve a thin layer of this epoxy for sticking wafers, initially a small

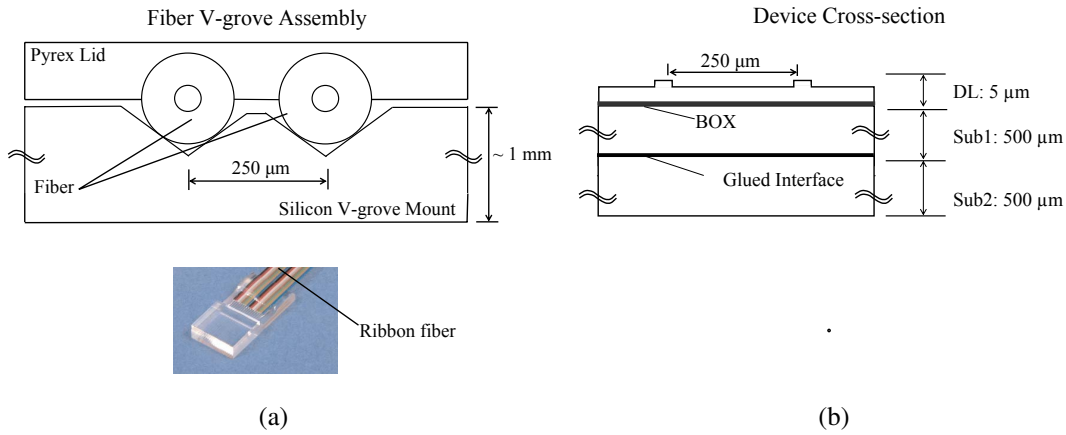


Figure 4.1: (a) Schematic cross-sectional view of fibers assembled in v-grooves (showing two adjacent fibers separated by a distance of  $250 \mu\text{m}$ .) Inset: photograph of a ribbon fiber - array of single-mode fibers assembled in v-grooves (ref: OZ Optics Limited). (b) Schematic cross-section of fabricated chip showing a pair of input/output waveguides of interleaver. DL-Device Layer, Sub1: Substrate1, Sub2: Substrate2.

quantity ( $\sim 1 \text{ ml}$ ) of hardner is dissolved in acetone. Later, equal (or lesser) quantity of polymer-resin is mixed with the prepared solution and immediately applied using a paint-brush on top of the dummy substrate. The fabricated device sample are then carefully placed over this dummy substrate and left to dry for 12-14 h. For proper sticking, approx  $\sim 400 - 500 \text{ gms}$  of metal weight was placed on top of the glued wafers. Care was taken to avoid the scratching of top device surface while putting under a metal weight. It is worth to mention here that, such a bonding is permanent bonding and can not be removed. The end facets of the glued wafers were again polished to  $< 0.5 \mu\text{m}$  roughness as mentioned in Section 3.2. The fiber v-grove assemblies are then critically

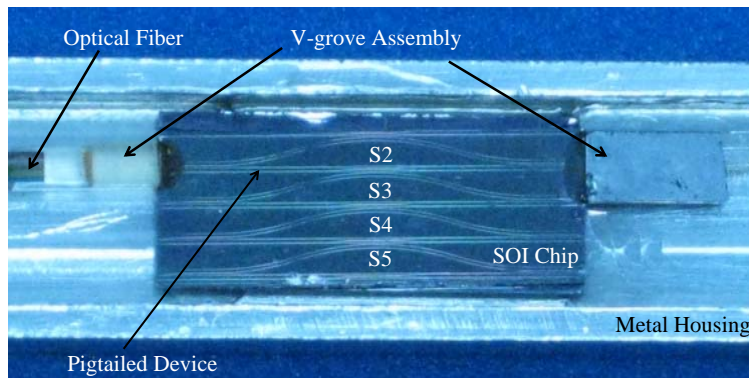


Figure 4.2: Photograph of a fiber pigtailed integrated SOI interleaver chip (sample GI12). The pigtailed interleaver is in set S2.



Figure 4.3: Photograph of a packaged prototype DWDM channel interleaver. Packaged device: GI12.

aligned to the waveguide end facets and glued using index matching epoxy adhesive (NOA-61, Norland Products, USA). In order to achieve permanent adhesion between the fiber and waveguide end-facet, the index matching epoxy glue was cured under UV radiation for  $\sim 8$  min. The pigtailed sample is later housed in a metal casing (see Fig. 4.2). Photographic image of a prototype DWDM-channel interleaver has been shown in Fig. 4.3.

## 4.2 Test Results and Discussions

The packaged interleaver structures have been tested for their performance. A schematic of experimental setup used for testing of prototype device is shown in Fig. 4.4. The wavelength-dependent output response of the device is measured using a detector and the data is logged in a computer. The Fig. 4.5(a) and 4.5(b) show wavelength dependent transmission characteristics ( $\lambda \sim 1550$  to  $1555$  nm) for an interleaver (in set S2 of GI12) before and after pigtailed with standard single-mode fibers (SMF-28), respectively. The degradation in interchannel extinction is because, both the polarizations are excited in the device as the input fiber (SMF-28) is not polarization maintaining. Therefore, it is necessary to ensure high polarization extinction during device operation.

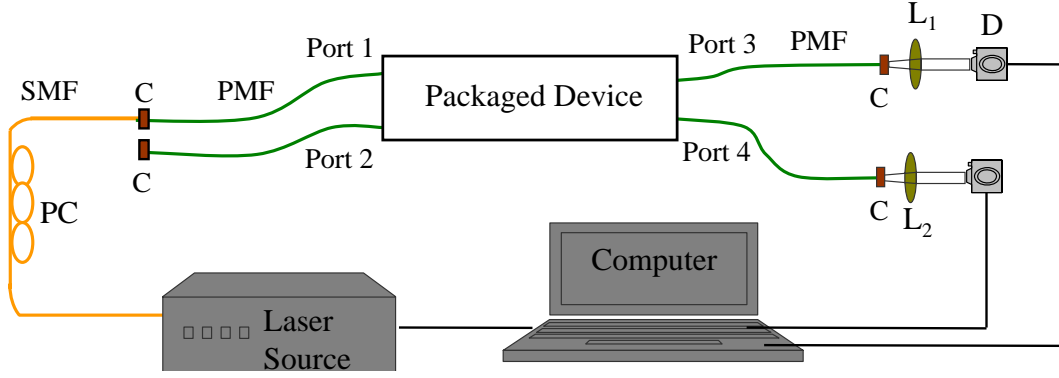


Figure 4.4: Experimental setup for characterization of packaged DWDM channel interleaver. PC- Polarization Controller, SMF- Single Mode Fiber, PMF- Polarization Maintaining Fiber, C- Connector, L- Lens, D- Detector.

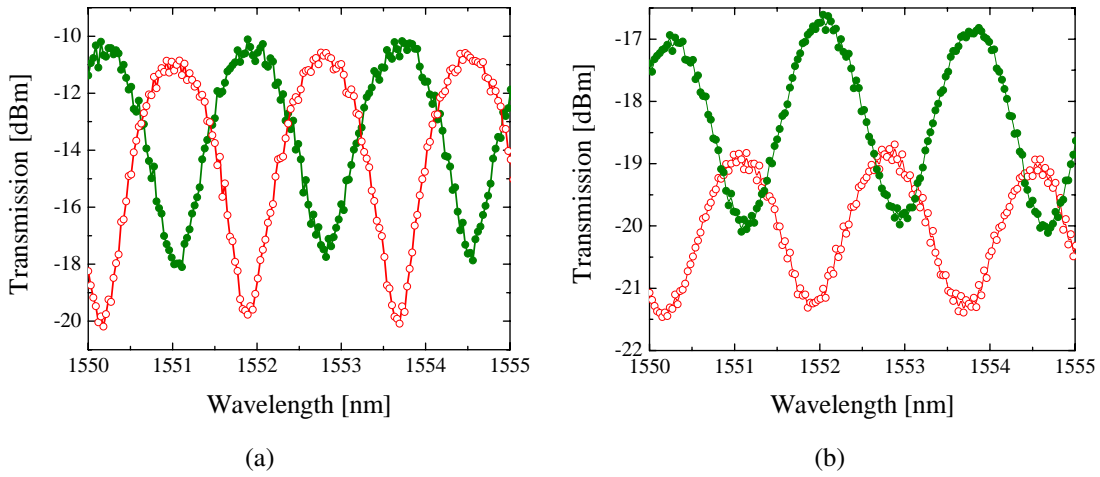


Figure 4.5: Wavelength dependent transmission characteristics of DWDM channel interleaver before and after pigtailling. (a) Response of interleaver in TE polarization before pigtailling, (b) Response of interleaver after pigtailling with SMF-28. Lines in red correspond to response at Port 3 (Bar) and, lines in green correspond to response at Port 4 (cross). The characteristics shown are recorded from interleaver in set S2 of GI12.

In order to ensure device operation in single polarization, another sample GI14 was pigtailed using PM fibers (type: PANDA). The Fig. 4.6(a) and Fig. 4.6(b) show wavelength dependent transmission characteristics ( $\lambda \sim 1550$  to  $1560$  nm, TM polarization) of interleaver before and after pigtailling with polarization maintaining fibers ( $\delta_{ex} > 20$  dB), respectively. These characteristics are recorded from device in set S3 of sample GI14. Here, the output polarization is ensured by putting an external polarizer at the output arm. Clearly, the improvement in inter-channel extinction with improvement in polarization extinction is evident. It is worth mentioning here that the results shown

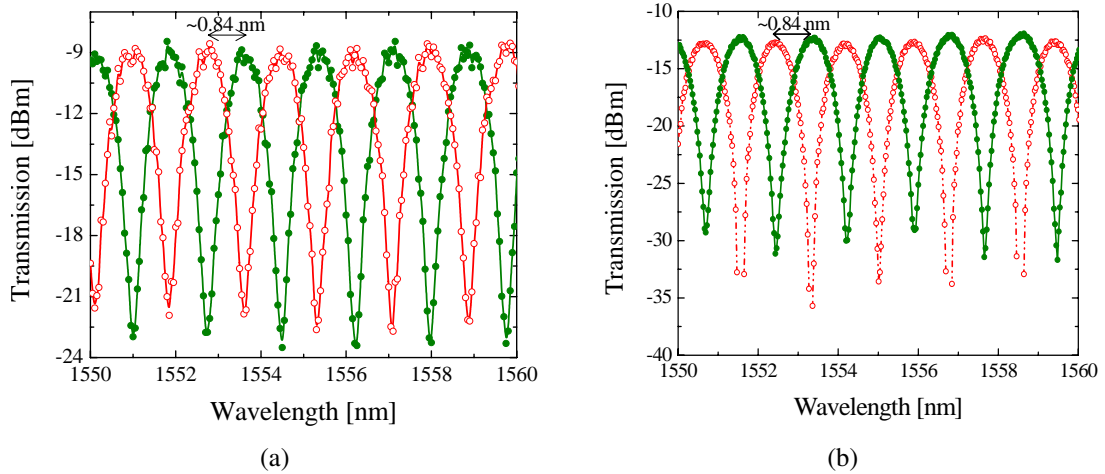
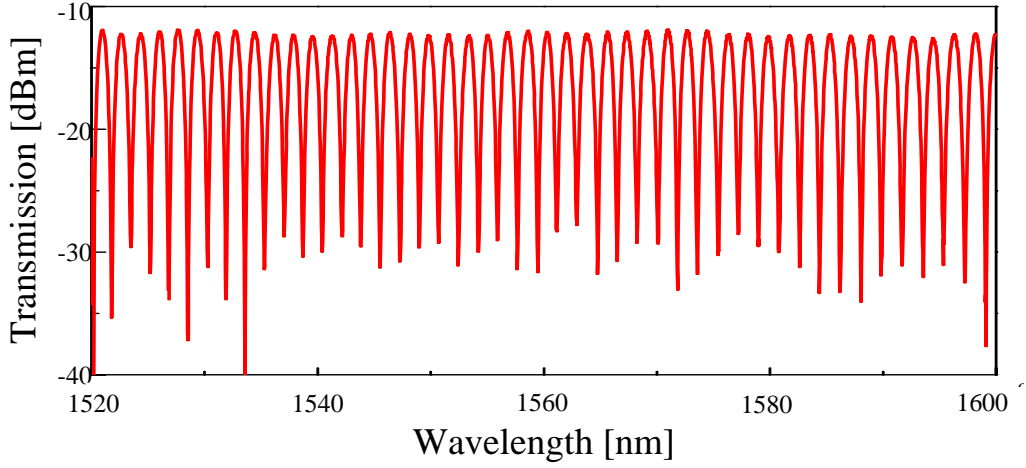
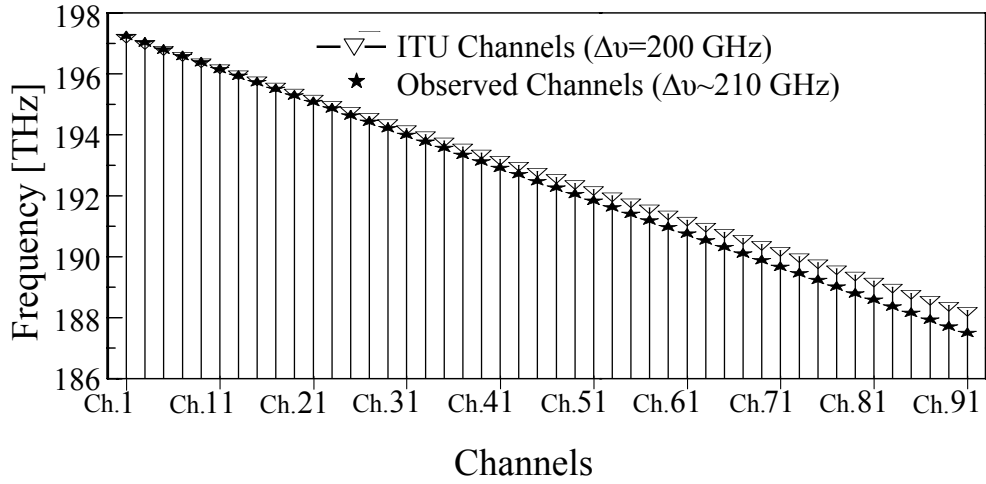


Figure 4.6: Wavelength dependent transmission characteristics of DWDM channel interleaver before and after pigtailling. (a) Response of interleaver before pigtailling and, (b) Response of interleaver after pigtailling with PM fibers (PANDA type). Lines in red correspond to response at Port 3 (Bar) and, lines in green correspond to response at Port 4 (cross). The characteristics shown here are recorded from interleaver in set S3 of GI14 for TM polarization.

in Fig. 4.5 and Fig. 4.6 are recorded from interleavers without integrated waveguide polarizers. Fig. 4.7(a) shows the wavelength dependent transmission characteristics ( $\lambda \sim 1520$  to  $1600$  nm) of PM fiber pigtailed SOI interleaver chip at Port 3 across most of the C+L band [81]. A comparison of deviation in channel spacings across the band of operation is also shown in Fig. 4.7. As already explained earlier in Section 3.3, the inter-channel spacing of  $210$  GHz ( $\Delta\lambda \sim 1.68$  nm) instead of expected  $200$  GHz ( $\Delta\lambda \sim 1.6$  nm) is due to CAD design error. A uniform interchannel extinction of  $> 18$  dB across the entire optical C+L band is recorded with a channel spacing of  $\sim 1.7$  nm. The packaged devices showed an insertion loss of  $\sim 19$  dB. As a comparison, the commercially available silica based channel interleavers show an overall insertion loss of  $\sim 2$  dB at channel pass-bands. This relatively high insertion loss in our case can be further reduced by improved end-face preparation, suitable anti-reflection coatings and appropriate index matching epoxy while fiber pigtailling. Moreover, the on-chip losses are directly or indirectly related to the waveguide sidewall roughness and can be reduced by use of ICP-RIE technique during waveguide fabrication. The Table 4.1 presents a comparison of measured data before and after characterization of interleaver pigtailed with PM fiber.



(a)



(b)

Figure 4.7: (a) Measured characteristics of packaged interleaver over the entire optical C+L band at Port 3 (Bar Port). (b) Position of experimentally measured resonance peaks with respect to the 100 GHz ITU channel standard. Results correspond to sample GI14.

Table 4.1: Characteristics of prototype DWDM channel interleaver. The results shown are measured for interleaver in set 3 of GI14 operating in TM polarization.

	<b>Before Packaging</b>	<b>After Packaging</b>
Dimensions	30 mm × 1.5 mm	100 mm × 20 mm
Input Polarization Extinction	~ 15 dB	>20 dB
Channel Spacing	0.84 nm	0.84 nm
Inter-channel Extinction	~ 12 dB	~ 18 dB
Channel Bandwidth	~ 40 GHz	~ 40 GHz
Insertion Loss	~ 11 dB	~ 19 dB



### 4.3 Conclusions

The polarization sensitive interleaver samples were pigtailed with commercially available PM fibers. The interleaved channels were  $\sim 210$  GHz apart and the response was uniform over the entire optical C+L band. This variation is due to the design error in  $\Delta L$  ( $\sim 0.1\%$ ) because of the angular rounding introduced by the mask designing CAD tool. The packaged prototype of DWDM channel interleaver showed  $\sim 19$  dB insertion loss and an inter-channel extinction of  $\sim 18$  dB. These losses can be further improved by better end-facet preparation, suitable anti-reflection coatings and appropriate index matching epoxy while fiber pigtailling.

# CHAPTER 5

## Conclusions

### 5.1 Summary

Channel interleavers with various waveguide cross-section namely, PhWW, PhWRW, RCRW and LCRW have been theoretically studied. Subsequently, a dispersion-free channel interleaver based on LCRW structures had been proposed. Various design parameters for single-mode straight waveguides, bend waveguides and, directional couplers have been optimized for low-loss and dispersion-free operation of an LCRW based interleaver. Afterwards, a dispersion-free integrated optical DWDM channel interleaver based on large cross-section SOI rib waveguides has been successfully demonstrated. An interchannel extinction of  $> 13$  dB has been obtained over the entire optical C+L band with channel spacing of  $\sim 210$  GHz in of the output each ports of interleaver. The reference directional couplers showed wavelength independent  $\sim 3$ -dB power splitting. Reference straight waveguides showed a waveguide loss of 0.8 dB/cm and 1 dB/cm for TM and TE polarizations, respectively. The 3-cm-long interleaver showed an overall on-chip insertion loss of  $\sim 11$  dB at the channel resonance peak. This includes, waveguide loss ( $\sim 1$  dB), bend-induced losses ( $\sim 1.5$  dB/bend) and insertion loss of each directional couplers ( $\sim 1$  dB). The fabricated interleavers were found to be slightly polarization sensitive due to the asymmetric cross-sectional geometry of large cross-section rib waveguides. As a result, the resonance peaks in transmission characteristics of interleaver when operated for two different polarization (TE and TM) were found to be shifted ( $\delta\lambda = \lambda_r^{TE} - \lambda_r^{TM} \sim 0.25$  pm). Thus, it is necessary to ensure optimum polarization extinction during device performance to achieve significant inter-channel extinction. Moreover, it has also been found that there is significant amount of polarization cross-talk in LCRW based bend waveguides that can degrade the device performance. Hence, TE-pass metal-clad waveguide polarizers were investigated using various metals like Al, Au and Cr. A polarization extinction of  $> 15$  dB (Cladding

metal: Al, thickness:  $\sim 1$  nm, length:  $\sim 1$  mm) was achieved during device performance. However, it was found that integration of waveguide polarizers increases the overall insertion loss by  $\sim 2$  dB.

Some of the interleavers have been fiber-pigtailed using polarization maintaining (PANDA) fibers. The fiber pigtailed and packaged prototype devices showed an inter-channel extinction of  $> 15$  dB at either of the ports with an insertion loss of  $\sim 19$  dB at channel resonance peaks. The relatively high insertion loss can be reduced by better surface smoothness on side walls of the rib through ICP RIE technique as compared to conventional RIE, use of anti-reflection coating at the device end-facets and better quality of index matching epoxy for fiber pigtailed.

## 5.2 Outlook

Interleavers are an important component for increasing the transmission capacity of an optical link. In order to have a higher channel modulation, it is necessary that the interleavers provide a flat-band response around the channel resonance peaks. This can be achieved by integrating a ring structure at one of the arm of an interleaver. Recently, such an interleaver based on PhW waveguides, with flat-top pass band response has been demonstrated by integrating a ring-resonator at one of the arms of MZI [28]. The ring-resonator is matched at the channel resonance peak (see Fig. 5.1). However, the

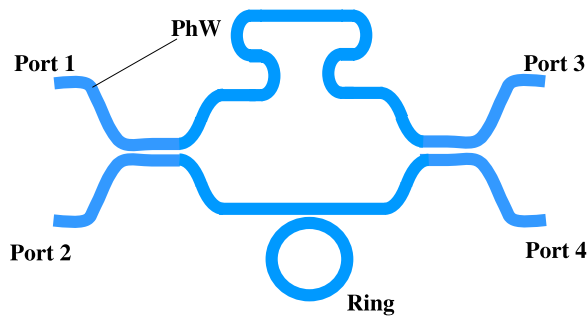


Figure 5.1: Schematic of an interleaver with integrated ring resonator [28].

device response has been found to be non-uniform across the band of operation due to dispersive characteristics of PhW waveguides. Dispersion in these sub-micron dimension silicon waveguides is still a challenging issue and needs thorough investigation. As discussed earlier in Section 2.2, the dispersion in silicon waveguides is mainly due

to the waveguide geometry. Hence, sub-micron PhW waveguides with low/negative dispersion characteristics can be designed by optimizing the waveguide-design parameters. Such an approach of modifying the waveguide geometry to reduce the dispersion has already been thoroughly investigated for single-mode fibers [86, 87, 88].

Integrating a ring structure with an LCRW based interleaver to achieve flat-band response can significantly increase the device foot-print. Alternatively, such interleavers can be designed with RCRW-based asymmetric MZI. RCRW based devices can have improved polarization and interchannel extinctions and relatively smaller foot-prints due to tighter confinement of the guided mode. Nevertheless, this can come at a cost of reduced operational band (see Fig. 2.16). Moreover, reconfigurable interleavers can be demonstrated by having an external heating element integrated with the package or an on-chip NiCr heater. Reconfigurability can also be achieved by integrated electro-optic element.

Integrated low cost ITU channel sources can be prepared using the interleavers with PhW waveguides. A typical block diagram of such a chip is shown in Fig. 5.2. Here,

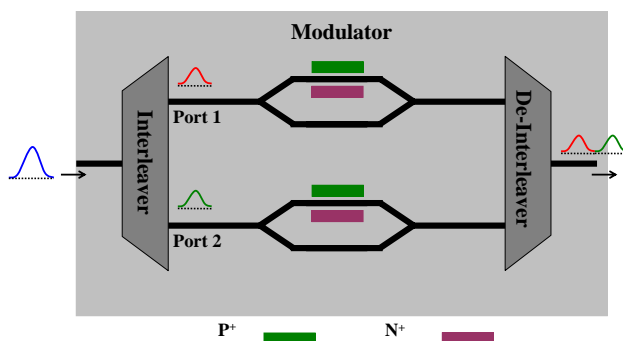


Figure 5.2: Proposed twin ITU channel source in SOI.

a low cost broad band laser source is used as an input to the interleaver on chip. An interleaver response can be electro-/thermo-optically tuned to match the ITU peaks. The two interleaved and consecutive ITU channels with designed channel spacing ( $\Delta\lambda = 0.8$  nm in this case) thus generated, can be taken into two separate output waveguides. The two separated DWDM channels can be modulated using an on-chip modulator and later fed to the inputs of a de-interleaver. The output of de-interleaver will be a DWDM signal carrying the modulated channels to be transmitted over the optical link. The interleaver demonstrated as a part of this thesis work have been experimentally

investigated for their response to an input signal with line width  $\sim 1$  nm. The two interleaved channels are shown in Fig. 5.3(a) (also see Fig. 2.1 and Section 2.1). The high inter-channel cross-talk in the center reduces the channel modulation capacity. As a solution, a ring resonator can be fabricated at one of the input arms of an interleaver in order to reduce the cross-talk, and avoid signal degradation on de-interleaving. This has been shown schematically in Fig. 5.3 (b).

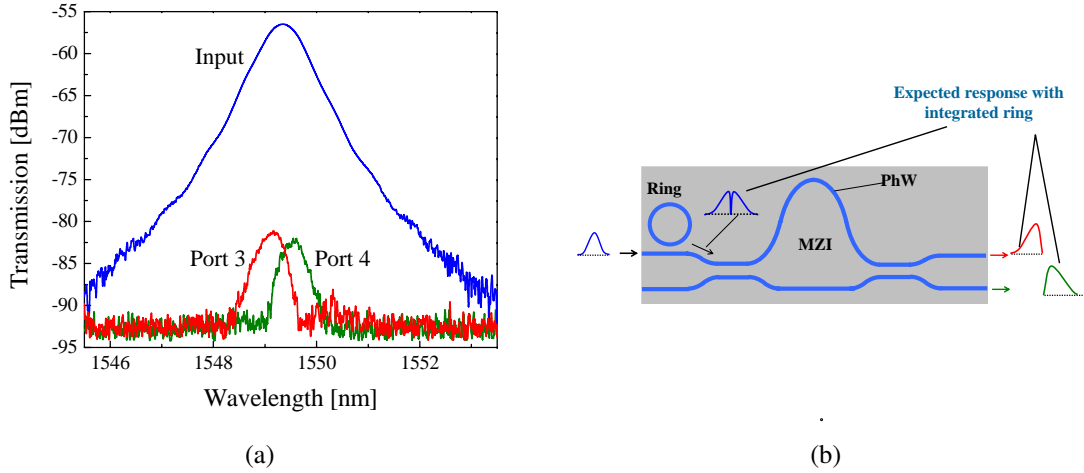


Figure 5.3: (a) Measured response of interleaver (S3-GI14) for broad band input source (line width  $\sim 1$  nm). Note the two distinct ITU peaks at the output ports. (b) Proposed design modification in interleaver to reduce the inter-channel cross-talk. Schematically shown is the distortion in the two peaks leading to low inter-channel cross talk.

The metal-clad waveguides can also be utilized to realize TM-pass polarizer. However, this requires deposition on metallic layer on the side walls of the rib. Though this is fabrication challenge, it can be achieved by depositing a thick layer of metal ( $\sim$  rib height) by electroplating followed by metal removal from top of the rib waveguide by photolithography and subsequent metal etching (see Fig. 5.4). This can also be achieved by  $n^{++}$ -type doping on the sides of rib close enough that the mode overlap tends to excite plasma oscillation and eventually leading to ohmic losses. Since the TE polarization having electric field component perpendicular to the doping regions can excite plasma oscillations, TM-pass polarizer can be realized.

Moreover, such metal-clad waveguides can also used to realize polarization beam splitters. Very recently, such surface plasmon excitation based polarization rotators and beam-splitters have been demonstrated [89, 90]. Such integrated beam splitters can

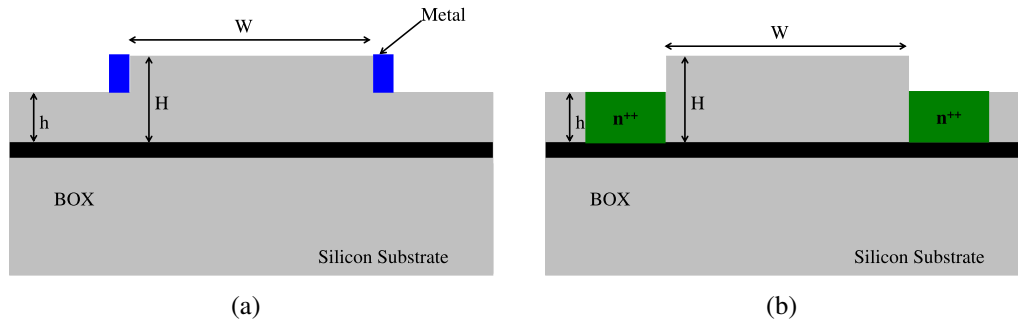


Figure 5.4: (a) Schematic of metal-clad waveguide for realizing TM-pass polarizer. (b) TM-pass polarizer using high doping on the sides of the rib.

also be used to remove signal with unwanted polarization and increase the polarization extinction. However, for realising such a devices it necessary to have metal-cladding of thickness less than the skin depth, in order to prevent ohmic losses of mode-energy coupled to plasma cloud of metal.

Metal-clad waveguides have also been widely studied for various applications on bio-sensing. The presence of bio-chemicals over the metal-cladding can vary the reflectivity of the light at the interface [91, 92]. The change in reflectivity and reflectance angle depends on the refractive index of the bio-chemical under test. These above proposed structures can also be realized with photonic wire waveguides utilizing high end fabrication techniques. This can help achieve smaller device footprints and better integratability. Finally, with the growing need for higher data rates, the future of data communication industry depends on integrated photonic devices and circuits which can offer higher reliability, better bandwidths and efficient reconfigurability for on-chip optical data processing, at miniaturized dimensions.



# APPENDIX A

## Appendix

### A.1 Asymmetric MZI Based Interleaver

#### Transfer Function of Asymmetric MZI

Considering Fig. 2.1, the electric field at different points in upper (lower) arm of interleaver are marked as  $E_{1i}$  ( $E_{1j}$ ). Consider  $M_{dc1}$ ,  $M_\phi$  and  $M_{dc2}$  are the transfer matrix of first directional coupler, the unbalanced arms and second directional coupler, respectively (see Fig. 2.1). Then the transfer matrix solution for the interleaver can be derived as below.

$$M_{dc1} = \begin{bmatrix} E_{12} \\ E_{22} \end{bmatrix} = \begin{bmatrix} \cos(\kappa_1 L_{c1}) & -j \sin(\kappa_1 L_{c1}) \\ j \sin(\kappa_1 L_{c1}) & \cos(\kappa_1 L_{c1}) \end{bmatrix} \cdot \begin{bmatrix} E_{11} \\ E_{21} \end{bmatrix} \quad (\text{A.1})$$

$$M_\phi = \begin{bmatrix} E_{13} \\ E_{23} \end{bmatrix} = e^{-j\beta L} \begin{bmatrix} \exp(-j\phi) & 0 \\ 0 & \exp(j\phi) \end{bmatrix} \cdot \begin{bmatrix} E_{12} \\ E_{22} \end{bmatrix} \quad (\text{A.2})$$

$$M_{dc2} = \begin{bmatrix} E_{14} \\ E_{24} \end{bmatrix} = \begin{bmatrix} \cos(\kappa_2 L_{c2}) & -j \sin(\kappa_2 L_{c2}) \\ j \sin(\kappa_2 L_{c2}) & \cos(\kappa_2 L_{c2}) \end{bmatrix} \cdot \begin{bmatrix} E_{13} \\ E_{23} \end{bmatrix} \quad (\text{A.3})$$

Let  $M$  be the transfer matrix of asymmetric MZI based interleaver then,  $M = M_{DC2} \cdot M_\phi \cdot M_{DC1}$ . Now, considering  $\hat{M} = M_\phi \cdot M_{DC1}$  then

$$\begin{bmatrix} E_{13} \\ E_{23} \end{bmatrix} = e^{-j\beta L} \begin{bmatrix} \exp(-j\phi) & 0 \\ 0 & \exp(j\phi) \end{bmatrix} \cdot \begin{bmatrix} \cos(\kappa_1 L_{c1}) & -j \sin(\kappa_1 L_{c1}) \\ j \sin(\kappa_1 L_{c1}) & \cos(\kappa_1 L_{c1}) \end{bmatrix} \cdot \begin{bmatrix} E_{11} \\ E_{21} \end{bmatrix} \quad (\text{A.4})$$

$$\hat{M} = e^{-j\beta L} \begin{bmatrix} \exp(-j\phi) & 0 \\ 0 & \exp(j\phi) \end{bmatrix} \cdot \begin{bmatrix} \cos(\kappa_1 L_{c1}) & -j \sin(\kappa_1 L_{c1}) \\ j \sin(\kappa_1 L_{c1}) & \cos(\kappa_1 L_{c1}) \end{bmatrix} \quad (\text{A.5})$$

$$\hat{M} = e^{-j\beta L} \begin{bmatrix} 2j \sin \phi & 2j \cos \phi \\ 2j \cos \phi & -2j \sin \phi \end{bmatrix} \quad (\text{A.6})$$

Assuming that the directional couplers has exact 3-dB power splitting, then  $\kappa_1 \cdot L_{c1} = \kappa_1 \cdot L_{c1} = \frac{\pi}{4}$ . Now, for  $M = M_{DC2} \cdot \hat{M}$  then

$$\hat{M} = e^{-j\beta L} \begin{bmatrix} 0.707 & -0.707j \\ 0.707j & 0.707 \end{bmatrix} \cdot \begin{bmatrix} 2j \sin \phi & 2j \cos \phi \\ 2j \cos \phi & -2j \sin \phi \end{bmatrix} \quad (\text{A.7})$$

$$E_{14} = \exp(-j\beta L)(E_{11} \cdot \sin \phi + E_{21} \cdot \cos \phi)j \quad (\text{A.8})$$

$$E_{24} = \exp(-j\beta L)(E_{11} \cdot \cos \phi + jE_{21} \cdot \sin \phi)j \quad (\text{A.9})$$

The power can then be given as,

$$P_{14} = (E_{11}^2 \cdot \sin^2 \phi) + E_{21} \cdot E_{11} \cdot \sin(2\phi) + (E_{21}^2 \cdot \cos^2 \phi) \quad (\text{A.10})$$

$$P_{14} = (E_{11}^2 \cdot \cos^2 \phi) + E_{21} \cdot E_{11} \cdot \sin(2\phi) + (E_{21}^2 \cdot \sin^2 \phi) \quad (\text{A.11})$$

Assuming there is no input at port 2, the equation of power distribution at output port 3 and port 4 can be written as:

$$P_{14} = (E_{11}^2 \cdot \sin^2 \phi) + E_{21} \cdot E_{11} \cdot \sin(2\phi) \quad (\text{A.12})$$



$$P_{14} = (E_{11}^2 \cdot \cos^2 \phi) + E_{21} \cdot E_{11} \cdot \sin(2\phi) \quad (\text{A.13})$$

## Interleaver Channel Spacing

The schematic of interleaver is shown in Fig. 2.1. Assume that the two consecutive WDM channels ( $\lambda_1$  and  $\lambda_2$ ) are given at its input. The effective refractive index of two channel wavelengths is  $n_1$  and  $n_2$ . The phase accumulated by channel  $\lambda_1$  while propagating in two arms can be given as below.

$$\lambda_1 \phi_1 = \frac{2\pi n_1 L_1}{\lambda_1} \quad (\text{A.14})$$

$$\lambda_1 \phi_2 = \frac{2\pi n_1 L_2}{\lambda_1} + \left(\frac{\pi}{2}\right)_{DC1} + \left(\frac{\pi}{2}\right)_{DC2} \quad (\text{A.15})$$

Similarly, for channel  $\lambda_2$

$$\lambda_2 \phi_1 = \frac{2\pi n_2 L_1}{\lambda_2} \quad (\text{A.16})$$

$$\lambda_2 \phi_2 = \frac{2\pi n_2 L_2}{\lambda_2} + \left(\frac{\pi}{2}\right)_{DC1} + \left(\frac{\pi}{2}\right)_{DC2} \quad (\text{A.17})$$

It is required that  $\lambda_1$  exists in Port 3 only and hence from A.14, A.15,

$$\lambda_1 \phi = \lambda_1 \phi_1 - \lambda_1 \phi_2 = 2l\pi \quad (\text{A.18})$$

$$\Rightarrow \frac{2\pi n_1 L_1}{\lambda_1} - \frac{2\pi n_1 L_2}{\lambda_1} + \pi = 2l\pi \quad (\text{A.19})$$

$$\Rightarrow \frac{2\pi n_1 \Delta L}{\lambda_1} + \pi = 2l\pi \quad (\text{A.20})$$

Similarly,

$$\lambda_2 \phi = \lambda_2 \phi_1 - \lambda_2 \phi_2 = (2m - 1)\pi \quad (\text{A.21})$$

$$\Rightarrow \frac{2\pi n_2 L_1}{\lambda_2} - \frac{2\pi n_2 L_2}{\lambda_2} + \pi = 2l\pi \quad (\text{A.22})$$

$$\Rightarrow \frac{2\pi n_2 \Delta L}{\lambda_2} + \pi = (2l - 1)\pi \quad (\text{A.23})$$

here,  $l$  and  $m$  are integers. If  $\lambda_1$  exists in only Port 3 and  $\lambda_2$  only in Port 4, then,

$$\lambda_1 \phi - \lambda_2 \phi = \pi \quad (\text{A.24})$$

$$\Rightarrow \frac{2\pi n_1 \Delta L}{\lambda_1} + \pi - \frac{2\pi n_2 \Delta L}{\lambda_2} + \pi = \pi \quad (\text{A.25})$$

$$\Rightarrow 2\pi \Delta L \left( \frac{n_2}{\lambda_2} - \frac{n_1}{\lambda_1} \right) = \pi \quad (\text{A.26})$$

$$\Rightarrow \Delta L = \frac{\lambda_1 \cdot \lambda_2}{2\Delta \lambda n_g} \quad (\text{A.27})$$

## A.2 Recipes for etching

Recipes used for etching of various materials during the fabrication process are mentioned below.

### Wet etching of Aluminium

#### Al Etchant Solution =

114.0 ml of Ortho-phosphoric Acid +

22.5 ml of Acetic Acid +  
4.5 ml of Nitric Acid +  
7.5 ml of DI Water

## **Wet etching of Chromium**

The Chromium etchant solution is prepared by mixing of two different solutions as mentioned below:

**Solution A** = 78 ml of DI Water + 22 gms of Ammonium Ceric Nitrate

**Solution B** = 92 ml of DI Water + 8 ml of Acetic Acid

**Cr Etchant Solution:** Solution A + Solution B

Note: DI water can be mixed appropriately with the final etchant solution to reduce its concentration.

## **Wet etching of Gold**

**Au Etchant Solution =**

4 gms Potassium Iodide +  
40 ml DI Water +  
1 gms Iodine

## **Dry etching of Silicon Dioxide**

The dry etching of residual SiO<sub>2</sub> on top of SOI wafer can also be done using conventional RIE technique. The growth of this SiO<sub>2</sub> mainly happens when wafer are exposed to ambience. Generally all the silicon etching steps are followed after silicon dioxide etching.

Recipe: Ar/CHF<sub>3</sub>:: 25/25 sccm

Chamber Pressure: 100 mTorr

RF Power: 200 W

## **Dry etching of Silicon**

The dry etching of Si has been done using conventional RIE technique.

Recipe: Ar/SF<sub>6</sub>:: 20/20 sccm

Chamber Pressure: 200 mTorr

RF Power: 150 W

## **PPR Ashing**

PPR ashing is often carried using conventional RIE technique. This is done to remove residual PPR on top of wafer, which could not be removed by acetone.

Recipe: O<sub>2</sub>:: 35 sccm

Chamber Pressure: 250 mTorr

RF Power: 150 W

## REFERENCES

- [1] R. Ramaswami and K. N. Sivarajan, *Optical Networks: A Practical Perspective*, 2nd ed. San Francisco, CA: Morgan Kaufmann, 2002.
- [2] C. A. Brackett, "Dense wavelength division multiplexing networks: principles and applications," *IEEE J. Sel. Areas in Commun.*, vol. 8, no. 6, pp. 948–964, Aug. 1990.
- [3] M. K. Smit, "Progress in AWG design and technology," in *IEEE LEOS WFOPC*, Jun. 2005.
- [4] M. Fischer, M. Reinhardt, and A. Forchel, "GaInAsN/GaAs laser diodes operating at 1.52  $\mu\text{m}$ ," *Electron. Lett.*, vol. 36, no. 14, pp. 1208–1209, Jul. 2000.
- [5] J. Swoger, C. Qiu, J. Simmons, D. Thompson, F. Shepherd, D. Beckett, and M. Cleroux, "Strained layer (1.5  $\mu\text{m}$ ) InP/InGaAsP lasing opto-electronic switch (LOES)," *IEEE Photon. Technol. Lett.*, vol. 6, no. 8, pp. 927–929, Aug. 1994.
- [6] K. J. Bachmann and J. L. Shay, "An InGaAs detector for the 1.0–1.7- $\mu\text{m}$  wavelength range," *App. Phy. Lett.*, vol. 32, no. 7, pp. 446–448, Apr. 1978.
- [7] V. N. Luk'yanov, A. T. Semenov, N. V. Shelkov, and S. D. Yakubovich, "Lasers with distributed feedback (review)," *Soviet J. Quantum Electron.*, vol. 5, no. 11, p. 1293, 1975.
- [8] A. Yariv and P. Yeh, *Photonics: Optical Electronics in Modern Communications (The Oxford Series in Electrical and Computer Engineering)*, 6th ed. Oxford University Press, USA, Jan. 2006.
- [9] Z. Alferov, "Double heterostructure lasers: Early days and future perspectives," *IEEE J. Sel. Topics Quantum Electron.*, vol. 6, no. 6, pp. 832–840, Nov.-Dec. 2000.
- [10] G. P. Agrawal, *Fiber-optic Communication Systems*, 3rd ed. John Wiley & Sons, 2002.
- [11] E. L. Wooten, K. M. Kissa, A. Yi-Yan, E. J. Murphy, D. A. Lafaw, P. F. Hallemeier, D. Maack, D. V. Attanasio, D. J. Fritz, G. J. McBrien, and D. E. Bossi, "A review of lithium niobate modulators for fiber-optic communications systems," *IEEE J. Sel. Topics Quantum Electron.*, vol. 6, no. 1, pp. 69–82, Jan.-Feb. 2000.
- [12] R. G. Walker, "High-speed III-V semiconductor intensity modulators," *IEEE J. Quantum Electron.*, vol. 27, no. 3, pp. 654–667, Aug. 1991.
- [13] K. Okamoto, *Fundamentals of optical waveguides*, 2nd ed. Elsevier, 2006.

- [14] S. Cao, J. Chen, J. N. Damask, C. R. Doerr, L. Guiziou, G. Harvey, Y. Hibino, H. Li, S. Suzuki, K. Y. Wu, and P. Xie, "Interleaver technology: Comparisons and applications requirements," *J. Lightw. Technol.*, vol. 22, no. 1, pp. 281–289, Jan. 2004.
- [15] D. wei Huang, T. hsuan Chiu, and Y. Lai, "Arrayed waveguide grating DWDM interleaver," in *OFC*, Mar. 2001.
- [16] C. H. Hsieh, R. Wang, Z. J. Wen, F. I. C.-W. L. Ian McMichael, Pochi Yeh, and I. Wood-Hi Cheng, Senior Member, "Flat-top interleavers using two Gires-Tournois etalons as phase-dispersive mirrors in a Michelson interferometer," *IEEE Photon. Technol. Lett.*, vol. 15, no. 2, pp. 242 – 244, Feb. 2003.
- [17] B. H. Verbeek, C. H. Henry, N. A. Olsson, K. J. Orlowsky, R. F. Kazarinov, and B. H. Johnson, "Integrated four-channel Mach-Zehnder multi/demultiplexer fabricated with phosphorous doped SiO<sub>2</sub> waveguides on Si," *J. Lightw. Technol.*, vol. 6, no. 6, pp. 1011 –1015, Jun. 1988.
- [18] Q. Wang, Y. Zhang, and Y. C. Soh, "All-fiber 3 × 3 interleaver design with flat-top passband," *IEEE Photon. Technol. Lett.*, vol. 16, no. 1, pp. 168 –170, Jan. 2004.
- [19] Q. J. Wang, Y. Zhang, and Y. C. Soh, "Efficient structure for optical interleavers using superimposed chirped fiber bragg gratings," *IEEE Photon. Technol. Lett.*, vol. 17, no. 2, pp. 387 –389, Feb. 2005.
- [20] K. Okamoto, K. Takiguchi, and Y. Ohmori, "16-channel optical add/drop multiplexer using silica-based arrayed-waveguide gratings," *Electron. Lett.*, vol. 31, no. 9, pp. 723 –724, Apr. 1995.
- [21] H. H. Yaffe, C. H. Henry, M. R. Serbin, and L. G. Cohen, "Resonant couplers acting as add-drop filters made with silica-on-silicon waveguide technology," *J. Lightw. Technol.*, vol. 12, no. 6, pp. 1010 –1014, Jun. 1994.
- [22] JDSU Communications Components, "Bandsplitters 200 GHz channel spacing," Sep. 2008. [Online]. Available: <http://www.jdsu.com/en-us/Optical-Communications/Products/a-z-product-%list/Pages/wdm-filter-200-ghz-bandsplitter.aspx>
- [23] H. Takahashi, Y. Ohmori, and M. Kawachi, "Design and fabrication of silica-based integrated-optic 1 × 128 power splitter," *Electron. Lett.*, vol. 27, no. 23, pp. 2131 –2133, Nov. 1991.
- [24] L. Pavesi, "Will silicon be the photonic material of the third millenium?" *J. Phy.: Con. Matt.*, vol. 15, p. R1169, Jun. 2003.
- [25] M. Haurylau, G. Chen, H. Chen, J. Zhang, N. A. Nelson, D. H. Albonesi, E. G. Friedman, and P. M. Fauchet, "On-chip optical interconnect roadmap: Challenges and critical directions," *IEEE J. of Quantum Electron.*, vol. 12, no. 6, pp. 1699 –1705, Nov.-Dec. 2006.
- [26] R. Soref, "The past, present, and future of silicon photonics," *IEEE J. Sel. Topics Quantum Electron.*, vol. 12, no. 6, pp. 1678 –1687, Nov.-Dec. 2006.

- [27] G. T. Reed, G. Mashanovich, F. Y. Gardes, and D. J. Thomson, "Silicon optical modulators," *Nature Photonics*, vol. 4, no. 8, pp. 518–526, 2010.
- [28] L.-W. Luo, S. Ibrahim, A. Nitkowski, Z. Ding, C. B. Poitras, S. J. B. Yoo, and M. Lipson, "High bandwidth on-chip silicon photonic interleaver," *Opt. Exp.*, vol. 18, no. 22, pp. 23 079–23 087, Oct. 2010.
- [29] B. Jalali and S. Fathpour, "Silicon photonics," *J. Lightw. Technol.*, vol. 24, no. 12, pp. 4600–4615, Dec. 2006.
- [30] O. Boyraz and B. Jalali, "Demonstration of a silicon Raman laser," *Opt. Exp.*, vol. 12, no. 21, pp. 5269–5273, Oct. 2004.
- [31] H. Rong, R. Jones, A. Liu, O. Cohen, D. Hak, A. Fang, R. Nicolaescu, and M. Paniccia, "An all silicon Raman laser," *Nature*, vol. 433, 2005.
- [32] A. Fang, E. Lively, Y. Kuo, D. Liang, and J. Bowers, "Distributed feedback silicon evanescent laser," in *OFC*, Feb. 2008.
- [33] J. Bowers, A. W. Fang, H. Park, R. Jones, M. J. Paniccia, and O. Cohen, "Hybrid silicon evanescent laser in a silicon-on-insulator waveguide," in *OFC*, Mar. 2007.
- [34] B. R. Koch, A. W. Fang, O. Cohen, and J. E. Bowers, "Mode-locked silicon evanescent lasers," *Opt. Exp.*, vol. 15, no. 18, pp. 11 225–11 233, Aug. 2007.
- [35] Y. Kuo, H. Park, A. W. Fang, J. E. Bowers, R. Jones, M. Paniccia, and O. Cohen, "High speed data amplification using hybrid silicon evanescent amplifier," in *OSA CLEO*, May 2007.
- [36] L. Agazzi, J. D. B. Bradley, M. Dijkstra, F. Ay, G. Roelkens, R. Baets, K. Wörhoff, and M. Pollnau, "Monolithic integration of erbium-doped amplifiers with silicon-on-insulator waveguides," *Opt. Exp.*, vol. 18, no. 26, pp. 27 703–27 711, Dec. 2010.
- [37] L. Colace, G. Masini, and G. Assanto, "Ge-on-Si approaches to the detection of near-infrared light," *IEEE J. Quantum Electron.*, vol. 35, no. 12, pp. 1843–1852, Dec. 1999.
- [38] O. Dosunmu, M. K. Emsley, D. D. Cannon, B. Ghyselen, L. C. Kimerling, and M. S. Unlu, "Germanium on double-SOI photodetectors for 1550 nm operation," in *IEEE LEOS*, Oct. 2003.
- [39] S. J. Koester, C. L. Schow, L. Schares, G. Dehlinger, J. D. Schaub, F. E. Doany, and R. A. John, "Ge-on-SOI-detector/Si-CMOS-amplifier receivers for high-performance optical-communication applications," *J. Lightw. Technol.*, vol. 25, no. 1, pp. 46–57, Jan. 2007.
- [40] H. Park, A. W. Fang, R. Jones, O. Cohen, O. Raday, M. N. Sysak, M. J. Paniccia, and J. E. Bowers, "A hybrid silicon evanescent photodetector," in *IEEE DRC*, Oct. 2007.

- [41] A. W. Fang, R. Jones, H. Park, O. Cohen, O. Raday, M. J. Paniccia, and J. E. Bowers, "Integrated AlGaInAs-silicon evanescent race track laser and photodetector," *Opt. Exp.*, vol. 15, no. 5, pp. 2315–2322, Mar. 2007.
- [42] G. T. Reed and A. P. Knights, *Silicon Photonics-An Introduction*. Wiley, 2004.
- [43] D. Marris-Morini, G. Rasigade, L. Vivien, E. Cassan, S. Laval, P. Rivallin, P. Lyan, and J. M. Fedeli, "Recent progress in fast silicon modulators," in *IEEE GFP*, Sep. 2008.
- [44] A. Liu, R. Jones, L. Liao, D. Samara-Rubio, D. Rubin, O. Cohen, R. Nicolaescu, and M. Paniccia, "A high-speed silicon optical modulator based on a metal–oxide–semiconductor capacitor," *Nature*, vol. 427, no. 6975, pp. 615–618, Feb. 2004.
- [45] Intel Labs, "The 50G silicon photonics link," Intel, Tech. Rep., 2010.
- [46] Q. Xu, S. Manipatruni, B. Schmidt, J. Shakya, and M. Lipson, "12.5 Gbit/s carrier-injection-based silicon micro-ring silicon modulators," *Opt. Exp.*, vol. 15, no. 2, pp. 430–436, Jan. 2007.
- [47] W. Jiang, L. Gu, X. Chen, and R. T. Chen, "Photonic crystal waveguide modulators for silicon photonics: Device physics and some recent progress," *Solid-State Electronics*, vol. 51, no. 10, pp. 1278–1286, Sep. 2007.
- [48] M. Uenuma, Y. Ikoma, Y. Kato, and T. Motooka, "Design and fabrication of temperature-independent arrayed-waveguide grating demultiplexers on SOI substrates," in *IEEE SOI*, Oct. 2005.
- [49] A. Alduino, L. Liao, R. Jones, M. Morse, B. Kim, W. Lo, J. Basak, B. Koch, H. Liu, H. Rong *et al.*, "Demonstration of a high speed 4-channel integrated silicon photonics WDM link with hybrid silicon lasers," in *OSA IPR*, Jul. 2010.
- [50] F. Xia, M. O'Boyle, L. Sekaric, and Y. A. Vlasov, "Compact wavelength multiplexers/demultiplexers using photonic wires on silicon-on-insulator (SOI) substrate," in *IEEE IPRM*, Jun. 2006.
- [51] J. Minowa and Y. Fujii, "Dielectric multilayer thin-film filters for wdm transmission systems," *J. Lightw. Technol.*, vol. 1, no. 1, pp. 116 – 121, Mar. 1983.
- [52] A. M. Prabhu, A. Tsay, Z. Han, and V. Van, "Ultracompact SOI microring add-drop filter with wide bandwidth and wide FSR," *IEEE Photon. Technol. Lett.*, vol. 21, no. 10, pp. 651–653, May 2009.
- [53] Z. Wu, S. Honda, J. Matsui, K. Utaka, T. Edura, M. Tokuda, K. Tsutsui, and Y. Wada, "Tunable monolithic DWDM band-selection interleaver filter switch on silicon-on-insulator substrate," *J. Lightw. Technol.*, vol. 26, no. 19, pp. 3363 – 3368, Oct. 2008.
- [54] Z. Wang, S.-J. Chang, C.-Y. Ni, and Y. J. Chen, "A high-performance ultracompact optical interleaver based on double-ring assisted mach-zehnder interferometer," *IEEE Photon. Technol. Lett.*, vol. 19, no. 14, pp. 1072 –1074, July 2007.



- [55] T. Aalto, K. Solehmainen, M. Harjanne, M. Kapulainen, and P. Heimala, "Low-loss converters between optical silicon waveguides of different sizes and types," *IEEE Photon. Technol. Lett.*, vol. 18, no. 5, pp. 709–711, Mar. 2006.
- [56] R. Holly, K. Hingerl, R. Merz, and P. Hudek, "Fabrication of silicon 3D taper structures for optical fibre to chip interface," *Microelectron. Eng.*, vol. 84, no. 5-8, pp. 1248–1251, Feb. 2007.
- [57] L. Vivien, S. Laval, B. Dumont, S. Lardenois, A. Koster, and E. Cassan, "Polarization-independent single-mode rib waveguides on silicon-on-insulator for telecommunication wavelengths," *Opt. Commun.*, vol. 210, no. 1-2, pp. 43 – 49, Sep. 2002.
- [58] R. K. Navalakhe, N. DasGupta, and B. K. Das, "Fabrication and characterization of straight and compact s-bend optical waveguides on a silicon-on-insulator platform," *Appl. Opt.*, vol. 48, no. 31, pp. G125–G130, Nov. 2009.
- [59] R. K. Navalakhe, "Design, fabrication and characterization of straight and bend optical waveguides on silicon-on-insulator," Master's thesis, Dept. Electrical Engineering, IIT Madras, Jul. 2009.
- [60] J. P. George, N. Dasgupta, and B. K. Das, "Compact integrated optical directional coupler with large cross section silicon waveguides," *Proc. SPIE 7719*, vol. 77191X, 2010.
- [61] J. P. George, "Design, fabrication and characterization of integrated optical directional coupler on silicon-on-insulator," Master's thesis, Dept. Electrical Engineering, IIT Madras, Sep. 2010.
- [62] K. Jinguji, "Synthesis of coherent two-port optical delay-line circuit with ring waveguides," *J. Lightw. Technol.*, vol. 14, no. 8, pp. 1882–1898, Aug. 1996.
- [63] H. Yamada, T. Chu, S. Ishida, and Y. Arakawa, "Si photonic wire waveguide devices," *IEEE J. Sel. Topics Quantum Electron.*, vol. 12, no. 6, pp. 1371 –1379, Nov.-Dec. 2006.
- [64] R. A. Soref, J. Schmidtchen, and K. Petermann, "Large single-mode rib waveguides in GeSi-Si and Si-on-SiO<sub>2</sub>," *IEEE J. Quantum Electron.*, vol. 27, no. 8, pp. 1971 –1974, Aug. 1991.
- [65] Y. Quan, P. Han, Q. Ran, F. Zeng, L. Gao, and C. Zhao, "A photonic wire-based directional coupler based on soi," *Opt. Commun.*, vol. 281, no. 11, pp. 3105–3110, Jun. 2008.
- [66] S. T. Lim, C. E. Png, E. A. Ong, and Y. L. Ang, "Single mode, polarization-independent submicron silicon waveguides based on geometrical adjustments," *Opt. Exp.*, vol. 15, no. 18, pp. 11 061–11 072, Sep. 2007.
- [67] K. Yamada, T. Tsuchizawa, T. Watanabe, H. Fukuda, H. Shinojima, and S. Itabashi, "Applications of low-loss silicon photonic wire waveguides with carrier injection structures," in *IEEE GFP*, Sep. 2007.

- [68] H. Rong, R. Jones, A. Liu, O. Cohen, D. Hak, A. Fang, R. Nicolaescu, and M. Paniccia, "An all silicon Raman laser," *Nature*, vol. 433, pp. 293–294, Jan. 2005.
- [69] M. Bass, C. DeCusatis, G. Li, V. N. Mahajan, J. Enoch, and E. V. Stryland, *Handbook of Optics: Optical Properties of Materials, Non-linear Optics, Quantum Optics*, 1st ed. McGraw-Hill, 2009.
- [70] W. W. Lui, T. Hirono, K. Yokoyama, and W. P. Huang, "Polarization rotation in semiconductor bending waveguides: A coupled-mode theory formulation," *J. Lightw. Technol.*, vol. 16, no. 5, p. 929, May 1998.
- [71] T. Baba, "Si photonic wire waveguides," *Proc. SPIE 5515*, pp. 150 – 157, 2004.
- [72] K. Rollke and W. Sohler, "Metal-clad waveguide as cutoff polarizer for integrated optics," *IEEE J. Quantum Electron.*, vol. 13, no. 4, pp. 141 – 145, Apr. 1977.
- [73] L. L. Buhl, "Optical losses in metal/SiO<sub>2</sub>-clad Ti:LiNbO<sub>3</sub> waveguides," *Electron. Lett.*, vol. 19, no. 17, pp. 659 –660, Aug. 1983.
- [74] J. R. Feth and C. L. Chang, "Metal-clad fiber-optic cutoff polarizer," *Opt. Lett.*, vol. 11, no. 6, pp. 386–388, Jun 1986.
- [75] S. A. Maier, *Plasmonics: Fundamentals and Applications*, 1st ed. Springer, Berlin, May 2007.
- [76] H. Nishihara, M. Haruna, and T. Suhara, *Optical Integrated Circuits*. McGraw-Hill, 1985.
- [77] RSoft Design Group, "Rsoft material library," 2008.
- [78] A. Yariv and P. Yeh, *Optical Networks: A Practical Perspective*, 6th ed. Photonics: Optical Electronics in Modern Communication, 2002.
- [79] H. Janseny, H. Gardeniers, M. d. Boer, M. Elwenspoek, and J. Fluitman, "A survey on the reactive ion etching of silicon in microtechnology," *J. Micromech. Microeng.*, vol. 6, pp. 14 –28, 1996.
- [80] R. Regener and W. Sohler, "Loss in low-finesse Ti:LiNbO<sub>3</sub> optical waveguide resonators," *App. Phy. B: Lasers and Optics*, vol. 36, no. 3, pp. 143–147, 1985.
- [81] G. R. Bhatt, R. Sharma, U. Karthik, and B. K. Das, "Dispersion-free SOI interleaver for DWDM applications," *J. Lightw. Technol.*, vol. 30, no. 1, pp. 140–147, Jan. 2012.
- [82] G. R. Bhatt and B. K. Das, "Demonstration of ITU channel interleaver in SOI with large cross section single mode waveguides," *Proc. SPIE*, vol. 8069, p. 806904, Apr. 2011.
- [83] G. R. Bhatt and B. K. Das, "Improvement of polarization extinction in silicon waveguide devices," *Opt. Commun.*, vol. 285, no. 8, pp. 2067–2070, Apr. 2012.
- [84] M. Krause, H. Renner, and E. Brinkmeyer, "Polarization-dependent curvature loss in silicon rib waveguides," *IEEE J. Sel. Topics Quantum Electron.*, vol. 12, no. 6, pp. 1359–1362, Nov.-Dec. 2006.

- [85] C. Van Dam, L. H. Spiekman, F. Van Ham, F. H. Groen, J. Van Der Tol, I. Moerman, W. W. Pascher, M. Hamacher, H. Heidrich, C. M. Weinert, and M. K. Smit, “Novel compact polarization converters based on ultra short bends,” *IEEE Photon. Technol. Lett.*, vol. 8, no. 10, pp. 1346–1348, Oct. 1996.
- [86] L. N. Binh, T. L. Huynh, K. Y. Chin, and D. Sharma, “Design of dispersion flattened and compensating fibers for dispersion-managed optical communications systems,” *Int. J. Wireless and Opt. Comm.*, vol. 1, pp. 1–21, Jun. 2004.
- [87] M. A. Saifi, S. J. Jang, L. G. Cohen, and J. Stone, “Triangular-profile single-mode fiber,” *Opt. Lett.*, vol. 7, no. 1, pp. 43–45, Jan. 1982.
- [88] Y. W. Li, C. D. Hussey, and T. A. Birks, “Triple-clad single-mode fibers for dispersion shifting,” *J. Lightw. Technol.*, vol. 11, no. 11, pp. 1812–1819, Nov. 1993.
- [89] J. Zhang, S. Zhu, H. Zhang, S. Chen, G. Lo, and D. L. Kwong, “An ultra-compact polarization rotator based on surface plasmon polariton effect,” in *OFC*, Mar. 2011.
- [90] T. Yamazaki, J. Yamauchi, and H. Nakano, “A branch-type TE/TM wave splitter using a light-guiding metal line,” *J. Lightw. Technol.*, vol. 25, no. 3, pp. 922–928, Mar. 2007.
- [91] B. Liedberg, C. Nylander, and I. Lunström, “Surface plasmon resonance for gas detection and biosensing,” *Sensors and Actuators*, vol. 4, pp. 299–304, Jan. 1983.
- [92] M. Zourob, S. Mohr, B. J. Treves Brown, P. R. Fielden, M. B. McDonnell, and N. J. Goddard, “An integrated metal clad leaky waveguide sensor for detection of bacteria,” *Anal. Chem.*, vol. 77, no. 1, pp. 232–242, Dec. 2005.

## LIST OF PAPERS BASED ON THESIS

### Journals

1. Dispersion free SOI interleaver for DWDM applications  
**G.R. Bhatt**, R. Sharma, U. Karthik, and B.K. Das,  
*J. Lightw. Technol.*, vol. 30, no. 1, pp. 140-147, Jan. 2012.
2. Improvement of polarization extinction in silicon waveguide devices  
**G.R. Bhatt**, and B.K. Das,  
*Opt. Commun.*, vol. 285, no. 8, pp. 2067-2070, Apr. 2012.

### Conferences

1. *Silicon Photonics in SOI platform: Problems with waveguide dispersion and birefringence effects.*  
B.K. Das, Sujith C., **G.R. Bhatt**, U. Karthik and R. Sharma,  
*Frontiers in Optics and Photonics*, New Delhi, India, Dec. 3-5 (2011).
2. *Demonstration of ITU channel interleaver in SOI with large cross section single-mode waveguides.*  
**G.R. Bhatt**, and B.K. Das,  
*SPIE Microtechnologies*, Prague, Czech Republic, Apr. 18-20 (2011).
3. *Attenuation of TM-polarized light in metal coated SOI rib waveguides due to plasmonic absorption.*  
**G.R. Bhatt**, P.V. Vivek, and B.K. Das,  
*Photonics*, Guwahati, India, Dec. 12-15 (2010).

## **GENERAL TEST COMMITTEE**

- CHAIR PERSON** : **Prof. E. Bhattacharya**  
The Head,  
Dept. of Elec. Engg.
- GUIDE** : **Dr. B.K. Das**  
Dept. of Elec. Engg.
- GTC MEMBERS** : **Prof. N. DasGupta**  
Dept. of Elec. Engg.
- Prof. N.J. Vasa**  
Dept. of Engg. Design

## **CURRICULUM VITAE**

**NAME** : Gaurang R. Bhatt

**DATE OF BIRTH** : 16<sup>th</sup> Sept. 1986

**EDUCATIONAL QUALIFICATIONS** :

**Master of Science (by Research), 2009-2012**

Silicon Photonics

Dept. of Electrical Engineering, IIT-Madras

Chennai 600036, Tamil Nadu, India

**Bachelor of Engineering, 2004-2008**

Electronics

Birla Vishwakarma Mahavidyalaya, S.P. University

Vallabh-Vidyanagar 388120, Gujarat, India